

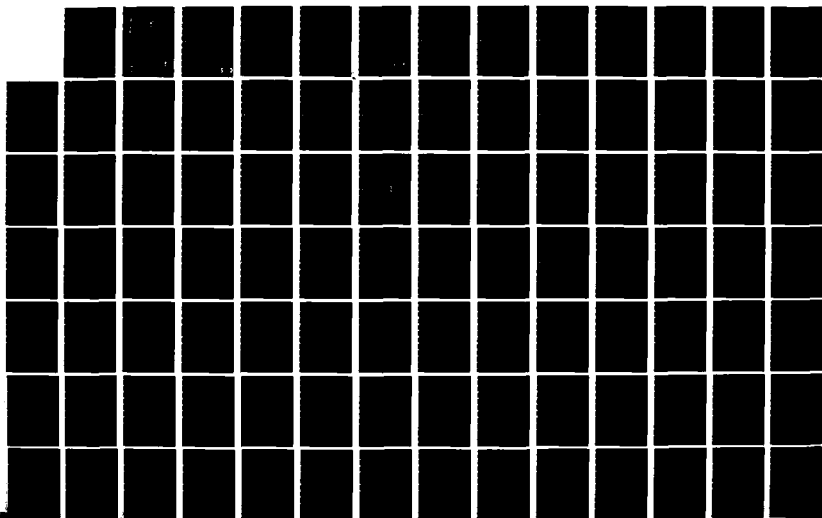
AD-A135 867

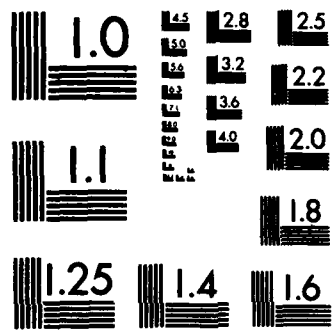
THE HIGH TEMPERATURE VISCOPLASTIC FATIGUE BEHAVIOR OF  
IN-100 USING THE BO. (U) AIR FORCE INST OF TECH  
WRIGHT-PATTERSON AFB OH SCHOOL OF ENGI.. R E WILSON  
SEP 83 AFIT/GAE/AA/835-6 F/G 11/6

1/2

UNCLASSIFIED

NL

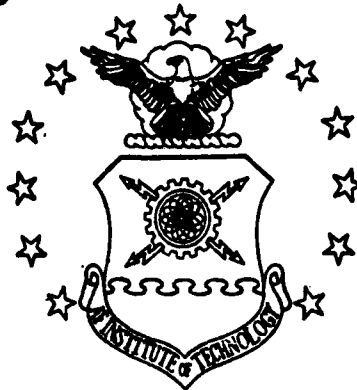




MICROCOPY RESOLUTION TEST CHART  
NATIONAL BUREAU OF STANDARDS-1963-A

AD-A135867

# AIR FORCE INSTITUTE OF TECHNOLOGY



AIR UNIVERSITY  
UNITED STATES AIR FORCE

THE HIGH TEMPERATURE VISCOPLASTIC FATIG  
BEHAVIOR OF IN-100 USING THE BODNER-  
PARTOM FLOW LAW  
THESIS

AFIT/GAE/AA/83S-6 Roy E. Wilson  
1LT USAF

DTIC FILE COPY

## SCHOOL OF ENGINEERING

DTIC  
ELECTE  
DEC 15 1983

WRIGHT-PATTERSON AIR FORCE BASE, OHIO

*[Handwritten signature]* B

**DISTRIBUTION STATEMENT A**  
Approved for public release  
Distribution Unlimited

83 12 13 245

AFIT/GAE/AA/83S-6

THE HIGH TEMPERATURE VISCOPLASTIC FATIGUE  
BEHAVIOR OF IN-100 USING THE BODNER-  
PARTOM FLOW LAW  
THESIS

AFIT/GAE/AA/83S-6

Roy E. Wilson  
1LT USAF

Approved for public release; distribution unlimited.

DTIC  
ELECTE  
DEC 15 1983  
S D  
B

THE HIGH TEMPERATURE VISCOPLASTIC FATIGUE  
BEHAVIOR OF IN-100 USING THE BODNER-PARTOM  
FLOW LAW

THESIS

Presented to the Faculty of the School of Engineering  
of the Air Force Institute of Technology  
Air University  
In Partial Fulfillment of the  
Requirements for the Degree of  
Master of Science

by

Roy E. Wilson

1Lt USAF

Graduate Aerospace Engineering

September 1983

Approved for public release; distribution unlimited.

Contents

	Page
Acknowledgements. . . . .	iii
List of Symbols . . . . .	iv
List of Figures . . . . .	vi
List of Tables. . . . .	xi
Abstract. . . . .	xii
I. Introduction . . . . .	1
Approach. . . . .	2
II. Viscoplasticity Theory . . . . .	4
Bodner-Partom Constitutive Model . . . . .	7
III. Method of Analysis . . . . .	12
The Computer Program. . . . .	12
Finite Element Modeling . . . . .	14
Verification of Computer Program. . . . .	21
IV. Results and Discussion . . . . .	24
Positive R-Ratio Compact Tension Specimen . . . . .	24
Negative R-Ratio Uniaxial Results . . . . .	41
Negative R-Ratio Compact Tension Specimen . . . . .	65
V. Conclusions. . . . .	86
Bibliography. . . . .	88
Appendix A: Computer Program Modifications . . . . .	90
Vita. . . . .	97

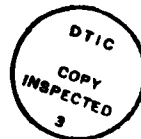
Acknowledgements

Many sincere thanks go to Dr. A. N. Palazotto for his guidance and patience during this research project. His outstanding educational abilities and comprehensive technical knowledge were what allowed completion of this course of study in the allotted time. My gratitude goes to Dr. T. Nicholas of the AFWAL Materials Laboratory for sponsoring this research. Thanks also go to Major James E. Keck of the ASD Propulsion Systems Program Office and to Capt Michael H. Bohun of the AFWAL Materials Laboratory for their aid.

I would like to especially thank my wife, Shelley, and my three wonderful children, Sarah, Robert, and Daniel. My wife provided immeasurable support and encouragement during my long hours of research.

Roy E. Wilson

Accession For	
NTIS GRA&I	<input checked="" type="checkbox"/>
DTIC TAB	<input type="checkbox"/>
Unannounced Justification	<input type="checkbox"/>
By _____	
Distribution/	
Availability Codes	
Dist	Avail and/or Special
A-1	



## List of Symbols

$(\dot{\phantom{a}})$	Time rate of change ( )
a	Crack length in compact tension specimen
C	Compliance
B	Compact tension specimen depth
$D_2^P$	Second invariant of plastic strain rate
$D_0$	Bodner material constant
E	Elastic modulus
G	Shear modulus
H, $\lambda$	Proportionality constants
i, j	Indices
$J_2, J_3$	Second and third invariant of deviatoric stress tensor
$K_I$	Stress intensity factor
k	Hardening parameter
m	Bodner material constant
n	Bodner material constant
p	Applied load
r	Bodner material constant
R	Load ratio Min Load/Max Load
$S_{ij}$	Deviatoric stress
$U_d$	Distortion strain energy

List of Symbols (Cont'd)

$W_p$	Plastic strain energy density
$Z$	Bodner model internal state variable
$Z_0, Z_1, Z_2$	Bodner material constant
$\epsilon$	Total uniaxial strain
$\epsilon_{ij}^e$	Components of total strain
$\epsilon_{ij}$	Elastic components of total strain
$\epsilon_{ij}^p$	Plastic components of total strain
$\sigma$	Uniaxial stress
$\sigma_{ij}$	Components of stress
$\sigma_{ys}$	Uniaxial material yield stress
$\dot{z}_{rec}$	Rate of work hardening recovery
Hz	Frequency of cycles per second

List of Figures

Figure		Page
3.1	Typical Load Cycles. . . . .	13
3.2	Uniaxial Finite Element Models . . . . .	17
3.3	Compact Tension Specimen Geometry. . . . .	18
3.4	2-Dimensional Finite Element Model . . . . .	19
3.5	Uniform Mesh Ahead of Crack Tip. . . . .	20
3.6	2-Dimensional Loads Cases. . . . .	23
4.1	Plastic Zones After 2.5 Cycles Mesh2A Compared to Mesh382 . . . . .	26
4.2	Y Stress vs Distance Ahead of Crack Tip Mesh2A Compared to Mesh382 . . . . .	27
4.3	Crack Mouth Displacement vs Percent Load Mesh2A Compared to Mesh382 . . . . .	28
4.4	Total Strain After Each Cycle 2.5 Hz $K_1=35\text{KSI } \sqrt{\text{in}}$ R=0.1 . . . . .	33
4.5	Projected Number of Cycles Required for Stabilization. . . . .	34
4.6	Y Displacement vs Distance Behind Crack Tip 2.5 Hz $K_1=35\text{KSI } \sqrt{\text{in}}$ R=0.1 . . . . .	35
4.7	Crack Mouth Displacement vs Percent Load 2.5 Hz $K_1=35\text{KSI } \sqrt{\text{in}}$ R=0.1 . . . . .	36
4.8	Effective Stress vs Total Strain at Crack Tip 2.5 Hz $K_1=35\text{KSI } \sqrt{\text{in}}$ R=0.1 . . . . .	37
4.9	Z Hardness vs Distance Ahead of Crack Tip 2.5 Hz $K_1=35\text{KSI } \sqrt{\text{in}}$ R=0.1 . . . . .	38

List of Figures (Cont'd)

Figure		Page
4.10	Y Stress vs Distance Ahead of Crack Tip 2.5 Hz $K_1=35\text{KSI } \sqrt{\text{in}}$ $R=0.1$ . . . . .	39
4.11	Y Strain vs Distance Ahead of Crack Tip 2.5 Hz $K_1=35\text{KSI } \sqrt{\text{in}}$ $R=0.1$ . . . . .	40
4.12	Uniaxial Stress-Strain Curve 2.5 Hz 130KSI Max Stress $R=-1.0$ . . . . .	45
4.13	Uniaxial Stress-Strain Curve 2.5 Hz 150KSI Max Stress $R=-1.0$ . . . . .	46
4.14	Uniaxial Stress-Strain Curve 2.5 Hz 165KSI Max Stress $R=-1.0$ . . . . .	47
4.15	Uniaxial Stress-Strain Curve 2.5 Hz 180KSI Max Stress $R=-1.0$ . . . . .	48
4.16	Uniaxial Stress-Strain Curve 2.5 Hz 200KSI Max Stress $R=-1.0$ . . . . .	49
4.17	Uniaxial Stress-Strain Curve 2.5 Hz 220KSI Max Stress $R=-1.0$ . . . . .	50
4.18	Uniaxial Stress-Strain Curve .167 Hz 130KSI Max Stress $R=-1.0$ . . . . .	51
4.19	Uniaxial Stress-Strain Curve .167 Hz 150KSI Max Stress $R=-1.0$ . . . . .	52
4.20	Uniaxial Stress-Strain Curve .167 Hz 165KSI Max Stress $R=-1.0$ . . . . .	53
4.21	Uniaxial Stress-Strain Curve .167 Hz 180KSI Max Stress $R=-1.0$ . . . . .	54

List of Figures (Cont'd)

Figure		Page
4.22	Uniaxial Stress-Strain Curve .167 Hz 200KSI Max Stress R=-1.0 . . . . .	55
4.23	Uniaxial Stress-Strain Curve .167 Hz 220KSI Max Stress R=-1.0 . . . . .	56
4.24	Uniaxial Stress-Strain Curve .03 Hz 130KSI Max Stress R=-1.0 . . . . .	57
4.25	Uniaxial Stress-Strain Curve .03 Hz 150KSI Max Stress R=-1.0 . . . . .	58
4.26	Uniaxial Stress-Strain Curve .03 Hz 165KSI Max Stress R=-1.0 . . . . .	59
4.27	Uniaxial Stress-Strain Curve .03 Hz 180KSI Max Stress R=-1.0 . . . . .	60
4.28	Uniaxial Stress-Strain Curve .03 Hz 200KSI Max Stress R=-1.0 . . . . .	61
4.29	Uniaxial Stress-Strain Curve .03 Hz 220KSI Max Stress R=-1.0 . . . . .	62
4.30	Uniaxial Stress-Strain Curve 10-Elements .167 Hz 200KSI Max Stress R=-1.0 . . . . .	63
4.31	Uniaxial Stress-Strain Curve .02 Tolerance .167 Hz 200KSI Max Stress R=-1.0 . . . . .	64
4.32	Z Hardness vs Time 2.5 Hz . . . . .	66
4.33	Z Hardness vs Time .167 Hz . . . . .	67
4.34	Z Hardness vs Time .03 Hz . . . . .	68
4.35	Y Displacement vs Distance Behind Crack Tip 2.5 Hz $K_1=35\text{KSI } \sqrt{\text{in}}$ R=-1.0 . . . . .	72

List of Figures (Cont'd)

Figure		Page
4.36	Y Displacement vs Distance Behind Crack Tip 2.5 Hz $K_1=45\text{KSI } \sqrt{\text{in}}$ $R=-1.0$ . . . . .	73
4.37	Y Stress vs Distance Ahead of Crack Tip 2.5 Hz $K_1=35\text{KSI } \sqrt{\text{in}}$ $R=-1.0$ at Full Tensile Load. . . . .	74
4.38	Y Stress vs Distance Ahead of Crack Tip 2.5 Hz $K_1=45\text{KSI } \sqrt{\text{in}}$ $R=-1.0$ at Full Tensile Load. . . . .	
4.39	Y Stress vs Distance Ahead of Crack Tip 2.5 Hz $K_1=35\text{KSI } \sqrt{\text{in}}$ $R=-1.0$ at Full Compres- sive Load . . . . .	76
4.40	Y Stress vs Distance Ahead of Crack Tip 2.5 Hz $K_1=45\text{KSI } \sqrt{\text{in}}$ $R=-1.0$ at Full Compres- sive Load . . . . .	77
4.41	Y Strain vs Distance Ahead of Crack Tip 2.5 Hz $K_1=35\text{KSI } \sqrt{\text{in}}$ $R=-1.0$ at Full Tensile Load. . . . .	78
4.42	Y Strain vs Distance Ahead of Crack Tip 2.5 Hz $K_1=45\text{KSI } \sqrt{\text{in}}$ $R=-1.0$ at Full Tensile Load. . . . .	79
4.43	Y Strain vs Distance Ahead of Crack Tip 2.5 Hz $K_1=35\text{KSI } \sqrt{\text{in}}$ $R=-1.0$ at Full Compres- sive Load . . . . .	80

List of Figures (Cont'd)

Figure	Page
4.44	
Y Strain vs Distance Ahead of Crack Tip	
2.5 Hz $K_1=45\text{KSI } \sqrt{\text{in}}$ $R=-1.0$ at Full Compressive Load. . . . .	81
4.45	
Plastic Zone After 2.25 Cycles	
2.5 Hz $K_1=45\text{KSI } \sqrt{\text{in}}$ $R=-1.0$ at Full Tensile Load . . . . .	82
4.46	
Plastic Zone After 2.25 Cycles	
2.5 Hz $K_1=45\text{KSI } \sqrt{\text{in}}$ $R=-1.0$ at Full Tensile Load . . . . .	83
4.47	
Plastic Zone After 2.75 Cycles	
2.5 Hz $K_1=35\text{KSI } \sqrt{\text{in}}$ $R=-1.0$ at Full Compressive Load. . . . .	84
4.48	
Plastic Zone After 2.75 Cycles	
2.5 Hz $K_1=45\text{KSI } \sqrt{\text{in}}$ $R=-1.0$ at Full Compressive Load. . . . .	85

List of Tables

Table		Page
2.1	Bodner Coefficients for IN-100 at 1350 F . .	11
3.1	Uniaxial Test Loads and Frequencies . . . .	15
3.2	Compact Tension Specimen Loads and Steess Intensity Factors . . . . .	21
4.1	Total Strain Values After Each Load Cycle. .	30

## Abstract

→ Few studies have been made on the stress/strain field or plastic zone size ahead of a crack tip in a high temperature environment under varying load frequencies and stress levels. Fewer studies have incorporated compressive loads or analyzed the effect of a negative R-ratio on the fatigue characteristics of the superalloy IN-100.

This study involves extending existing analysis of the stress field and plastic zone ahead of a crack tip in a compact tension specimen, through a larger number of load cycles and examining the nearly unexplored area of compressive loading of a crack in a superalloy. A USAF Materials Laboratory finite element computer program named VISCO was used for this study. The Bodner-Partom viscoplastic constitutive equations for describing the material behavior were utilized. Load spectra included various frequencies with R-ratios of 0.1 and -1.0 (zero mean load). ←

## I Introduction

Current emphasis in the United States Air Force on Product Assurance and equipment reliability coupled with the ever present need for cost savings has created the problem of maximizing the life cycle of airframe and engine components without jeopardizing mission safety. There are numerous standards governing the design, construction, and maintenance of airframe and engine components. These standards include requirements for periodic inspections to detect flaws.

In contrast to the normal requirements are some low cycle fatigue-limited jet engine parts which may be retired from service when no flaws have yet been found in them. Jet engine turbine disks are removed from service at a time when statistically 1 in 1000 would be expected to have initiated a crack of some finite length (0.03 in). Eighty percent of the disks have at least 10 useful lifetimes remaining, though no attempt is made to utilize the statistically "failed" disks [1].

From a mission safety standpoint, this retirement approach has been very successful. This approach is also very costly. It has been estimated that replacement costs for low cycle fatigue-limited jet engine components are in the vicinity of \$100,000,000 for the 1980-1985 time period [2]. A significant reduction of this cost could be realized if a procedure was developed to utilize a disk after it has statistically "failed."

The life cycle of a turbine disk is a complex one consisting of frequent load cycle variations with ambient temperatures of up to 1350 F. The elevated temperatures introduce time dependent creep phenomena which interact with the varied load spectra to produce complex material behavior. If the material behavior could be determined for the typical life cycle then accurate remaining life predictions could be made for components with subcritical flaws. Only those components with a quantifiable critical flaw size would therefore need to be retired [3].

#### Approach

This study attempts to quantify the material behavior under cyclic loading of IN-100, a superplastically forged nickel-based superalloy used in turbine disks for the F-100 jet engine. VISCO, a computer program developed by Hinnerichs [4] was used for this analysis. VISCO is a finite element program which uses constant strain triangular elements and has the capability to run with non-static loads.

The Bodner-Partom flow law subroutine in VISCO was used to model the plastic flow during the load cycling. The Bodner material parameters for IN-100 at 1350 F were experimentally determined by Stouffer [5]. The Bodner-Partom viscoplastic flow law has the capability to predict the behavior produced by cyclic effects, time dependent creep, strain hardening, and plastic deformation. This flow law is integrated through time by an Euler extrapolation scheme and incorporated into

the finite element program by utilizing the residual force technique [4].

A compact tension specimen was modeled differently than that used in previous work [12], to allow a larger number of load cycles to be examined. Load was input as a sawtoothed stress-time pattern of constant maximum and minimum stress. Load ratios of 0.1 and -1.0 were examined. During each time step the stress, strain, plastic work and the Z hardness material parameter were calculated for each element in the model.

The load ratio, herein referred to as R-ratio, is defined as the ratio of the applied minimum load to maximum load.

## II Viscoplasticity Theory

Viscoplasticity is a combination of two strain groups, time dependent nonrecoverable strain and plasticity. Time dependent strains accumulate at a finite rate and are therefore time dependent. Plastic strains are permanent and develop instantly since they are independent of time. The combined strain effect of time dependent strain and plasticity is measurable, irreversible and can be utilized in a unified plastic strain rate model. All materials exhibit some plastic behavior, even when the applied loads produce stress below the yield stress. Most plastic deformation below the yield stress is small and is therefore usually neglected [6].

Separating the total strain into elastic (reversible) and plastic (nonreversible) components yield:

$$\epsilon_{ij} = \epsilon_{ij}^e + \epsilon_{ij}^p \quad (2.1)$$

By taking the time derivative of equation (2.1), an expression for the total strain rate is obtained,

$$\dot{\epsilon}_{ij} = \dot{\epsilon}_{ij}^e + \dot{\epsilon}_{ij}^p \quad (2.2)$$

where  $\dot{\epsilon}_{ij}$  is the total strain rate,  $\dot{\epsilon}_{ij}^e$  is the elastic strain rate and  $\dot{\epsilon}_{ij}^p$  is the viscoplastic strain rate. The elastic strain rate  $\dot{\epsilon}_{ij}^e$  is related to the stress rate by the time derivative of Hooke's law. The viscoplastic strain rate  $\dot{\epsilon}_{ij}^p$ ,

assuming incompressibility and isotropy, is taken to follow the Prandtl-Reuss flow law of classical plasticity

$$\dot{\epsilon}_{ij}^p = \lambda S_{ij} \quad (2.3)$$

where  $S_{ij}$  are the components of the deviatoric stress tensor and  $\lambda$  is a scalar that reflects the viscosity of the material. In a classical theory, plastic deformation begins at yield and depends on a yield criterion. It can be shown that, at yield, the Prandtl-Reuss relations imply the Von Mises yield criterion [7]. The Von Mises yield criterion is used primarily for metals behavior and is based on the distortion strain energy theory. Yielding begins when the distortion strain energy equals the distortion strain energy required to produce yielding in a simple uniaxial stress test.

The distortion strain energy can be written as

$$U_d = \int_V S_{ij} d\epsilon'_{ij} dVol \quad (2.4)$$

where  $d\epsilon'_{ij}$  and  $S_{ij}$  are tensors related only to distortion, ( $S_{ij}$  is the deviatoric stress tensor).  $U_d$  can be written in terms of the second invariant of deviatoric stress,  $J_2$ , and the shear modulus  $G$  as

$$U_d = \frac{1}{2G} J_2 \quad (2.5)$$

where  $J_2$  in terms of the principal stresses is

$$J_2 = \frac{1}{6} \left[ (\sigma_1 - \sigma_2)^2 + (\sigma_2 - \sigma_3)^2 + (\sigma_1 - \sigma_3)^2 \right] \quad (2.6)$$

The distortion strain energy can now be written

$$U_d = \frac{1}{2} G \left[ (\sigma_1 - \sigma_2)^2 + (\sigma_2 - \sigma_3)^2 + (\sigma_1 - \sigma_3)^2 \right] \quad (2.7)$$

Since yielding is related to the strain energy in a uniaxial test,  $J_2$  and  $U_d$  can be reduced accordingly. For a uniaxial test

$$\sigma_1 = \sigma_{ys} \quad \sigma_2 = \sigma_3 = 0 \quad (2.8)$$

where  $\sigma_{ys}$  equals the stress at the start of yielding.  $J_2$  reduces to

$$J_2 = \frac{1}{3} \sigma_{ys}^2 \quad (2.9)$$

and the distortion strain energy becomes

$$U_d = \frac{1}{6} G \sigma_{ys}^2 \quad (2.10)$$

Equating the multiaxial distortion strain energy to that of the uniaxial case yields

$$J_2 = K \sigma_{ys}^2 \quad (2.11)$$

where  $k$  is a proportionality constant. Multiaxial plastic yielding is predicted to occur when  $J_2$  reaches the critical value at yield in a uniaxial stress test.

#### Bodner-Partom Constitutive Law

Bodner and Partom's constitutive law is based on the study of dislocation dynamics [8]. The constitutive equations are able to represent the principal features of cyclic loading behavior, including softening upon stress reversal, cyclic hardening or softening, cyclic saturation, cyclic relaxation, and cyclic creep. The formulation of the equations is arrived at by squaring the Prandtl-Reuss relation:

$$\dot{\epsilon}_{ij}^P = \lambda S_{ij} \quad (2.12)$$

resulting in

$$\frac{1}{2} \dot{\epsilon}_{ij}^P \dot{\epsilon}_{ij}^P = D_2^P = \frac{1}{2} \lambda^2 S_{ij} S_{ij} = \lambda^2 J_2 \quad (2.13)$$

where  $D_2^P$  is the second invariant of the plastic strain rate and  $J_2$  is the second invariant of the deviatoric stress. The plastic deformation rate has a functional relationship with the stress invariants, i.e.

$$D_2^P = D_2^P (J_2, Z_k, T) \quad (2.14)$$

Utilizing the above equations, the parameter  $\lambda$  can be found to be:

$$\lambda = \left[ D_2^P (J_2, Z_k, T) / J_2 \right]^{1/2} \quad (2.15)$$

Bodner and Partom further expressed  $D_2^P$  as:

$$D_2^P = D_0^2 \exp \left[ -\frac{(Z^2)^n}{3J_2} \frac{n+1}{n} \right] \quad (2.16)$$

This expression is based on extensive experimental data and has been modified to fit results found by several researchers.  $D_0$  is the limiting value of the plastic strain rate in shear. The parameter  $n$  controls strain rate sensitivity.  $Z$  is the measure of material hardening, and is a function of plastic work.

Analysis of the variables in the equation for the second invariant of the plastic strain rate show that  $D_0$  is an arbitrarily chosen value. For all materials, it is generally chosen as  $D_0 = 10^4 \text{ sec}^{-1}$ , unless very high rates of straining are present. The values of  $n$  chosen affect the inelastic level of the stress-strain curves. The parameter  $n$  influences the slope of the stress-strain rate curve and is therefore a measure of strain rate sensitivity [9].

Bodner's elastic-viscoplastic theory is based on an internal material state variable  $Z$ . Bodner's  $Z$  hardness parameter is a basic material property and is deformation

history dependent. The following relationship was introduced for the  $Z$  parameter:

$$Z = Z(\bar{W}_p) = Z_1 - (Z_1 - Z_0) \exp[-m\bar{W}_p] \quad (2.17)$$

The variables of interest in the above relationship include  $\bar{W}_p, Z_1, Z_0$ , and  $m$ .  $\bar{W}_p$  is the relative amount of plastic work done from some initial state and is mathematically defined at low temperatures to be:

$$\bar{W}_p = \int s_{ij} \epsilon_{ij}^p dt \quad (2.18)$$

$Z_1$  is the maximum value of hardness,  $Z_0$  is the value of  $Z$  where  $\bar{W}_p = 0$  (i.e. the initial state point), and  $m$  is a material constant, hardening rate exponent [10].

The analysis for this study is performed on a material under high temperature conditions. It is therefore necessary to include the thermal recovery of hardening due to high temperature. The plastic work oriented term,  $\bar{W}_p$  is redefined as follows:

$$\bar{W}_p = \int s_{ij} \epsilon_{ij}^p dt + \int \frac{\dot{z}_{rec} dt}{m(Z_1 - Z)} \quad (2.19)$$

where  $\dot{z}_{rec} = -A \left( \frac{Z - Z_2}{Z_1} \right)^r Z_1$  (2.20)

$Z_2$  is the stable, (i.e., non-work hardened) value of  $Z$  at a given temperature.  $A$  and  $r$  are material constants picked to match creep test data. The thermal recovery term ( $\dot{Z}_{rec}$ ) of Eq 2.20 makes a negative contribution to  $\bar{W}_p$  due to the negative sign on  $A$ , since  $Z$  is always greater than or equal to  $Z_2$ .

The Bodner constants for IN-100 at 1350 F are given in Table 2.1.

TABLE 2.1  
BODNER COEFFICIENTS FOR IN-100 AT 1350°F

Material Parameter	Description	Value
E	Elastic modulus	26.3x10 <sup>2</sup> KSI (18.133x10 <sup>4</sup> MPa)
n	Strain rate exponent	0.7
D <sub>0</sub>	Limiting value of strain rate	10 <sup>4</sup> sec
Z <sub>0</sub>	Limiting value of hardness	915.0 KSI (6304 MPa)
Z <sub>1</sub>	Maximum value of hardness	1015.0 KSI (6993 MPa)
Z <sub>2</sub>	Minimum value of hardness	600.0 KSI (4134 MPa)
m	Hardening rate exponent	2.57 KSI <sup>-1</sup> (.37273 MPa <sup>-1</sup> )
A	Hardening recovery coefficient	1.9x10 <sup>-3</sup> sec <sup>-1</sup>
r	Hardening recovery exponent	2.56
(1 KBAR = 100 MPa = 14.504 KSI)		

### III Methods of Analysis

#### The Computer Program

A two dimensional plane strain finite element program named VISCO was used throughout this study. VISCO accounts for both nonlinear viscoplastic material behavior and changing boundary conditions due to crack closure. The accuracy of the program has been verified by Smail [11] and Keck [12].

The Bodner-Partom viscoplastic constitutive equations in VISCO are solved using the Gauss-Seidel iterative equation solver with overrelaxation, eliminating costly stiffness matrix factorization. Time integration of the Bodner equations is accomplished for each element using an Euler extrapolation scheme. A variable time step algorithm is included that maximizes the time step size during the analysis while maintaining good accuracy. During each time step, equilibrium tolerances are checked. If the tolerances are exceeded, the time step is reduced until equilibrium is obtained.

To completely understand the material behavior of IN-100, it is necessary to conduct analysis over a range of loads, frequencies and R-ratios. The data can then be applied to any life duty cycle specified. For instance, in a jet engine turbine disk, there can be frequent load cycles of varying frequencies and load levels. In any application, there is also the likelihood of components being subjected to compressive loading.

The most convenient load spectrum for engine and other applications is saw-toothed load-time pattern with constant

maximum and minimum stress amplitudes. R-ratios of 0.1 and -1.0 give a good representation of the stress levels which may be seen in the life cycle of a component. These load spectra are illustrated in Fig 3.1.

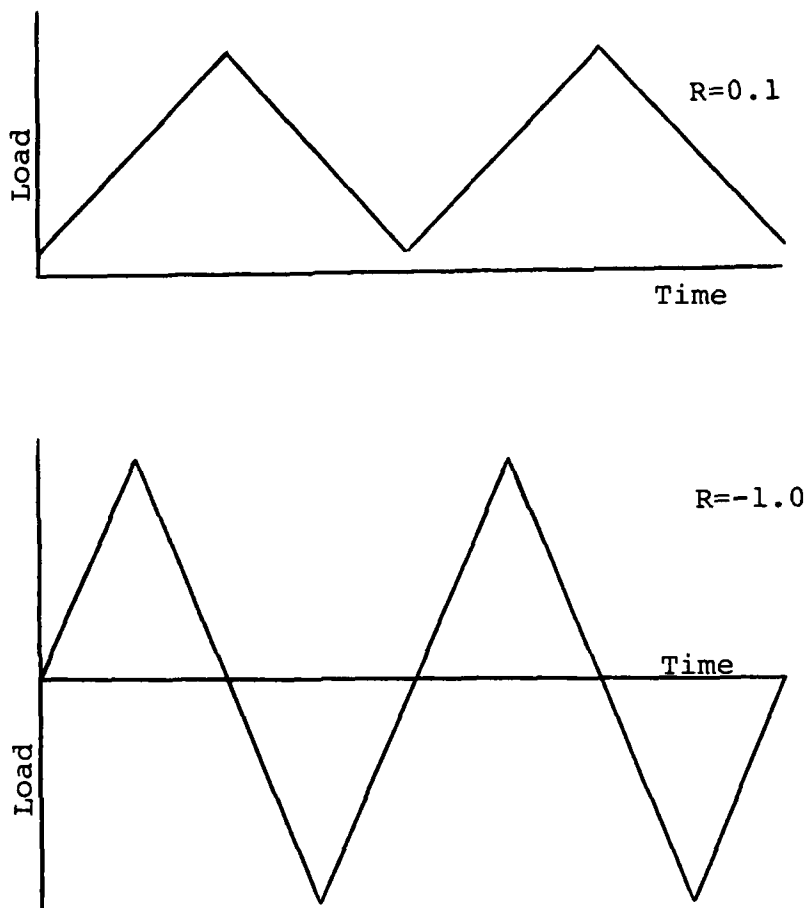


Fig 3.1 Typical Load Cycles

Frequencies for engine operation and turbine components generally range from .01 Hz to 5 Hz, which corresponds to experimental test data collected by Nicholas and Larsen [3].

VISCO's loading function was modified for the negative cycle response shown in the lower part of Fig 3.1 (see Appendix A). Using a linear load equation solver to model the load spectra shown in Fig 3.1, a percentage of total load was calculated at each time step. When the load percentage was less than zero, the load is applied to the lower edge of the hole for the compact tension specimen considered in the study. When the load percentage is positive, the load is applied to the top edge of the hole in the compact tension specimen (see Fig 3.4). Node displacement and element strain, stress and the Bodner Z-hardness were output at requested time intervals.

VISCO was also modified to accomplish crack closure and crack opening. The boundary condition on the nodes which lie along the crack edge when the node's displacement is positive is such that there is zero force on the node. When the node's displacement is calculated to be negative (indicating closure), the boundary condition changes to one of zero displacement, and the displacement of the node is reset to zero.

### Finite Element Modeling

Several finite element models were utilized throughout the course of this study. The first was the 2-element uniaxial model shown in the top of Fig 3.2. This model was used to validate the changes in VISCO and to provide uniaxial plane stress solutions for the frequencies and loads shown in Table 3.1. Variations in the computer program stress and strain

increment tolerances were tested with the 2-element model, and it was found that tighter tolerances than those used in the past [12], must be used to truly characterize the material behavior during negative load cycling.

TABLE 3.1

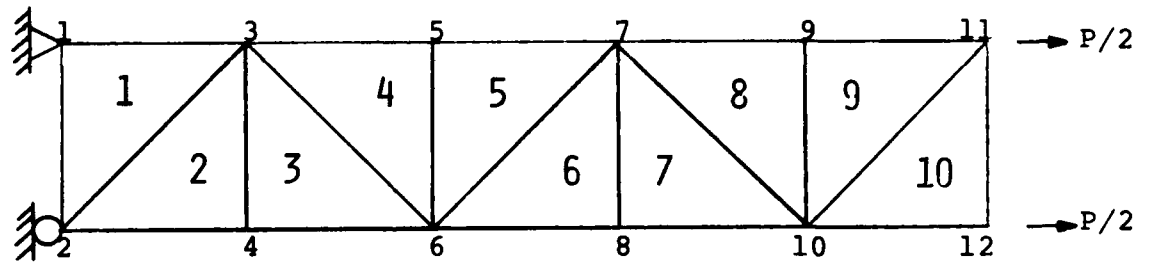
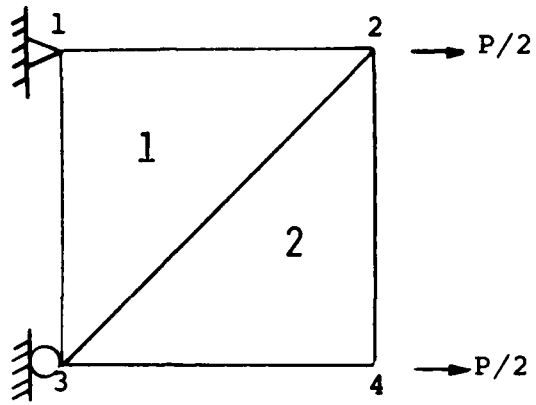
UNIAXIAL TEST LOADS AND FREQUENCIES

<u>Test Frequency (Hz)</u>	<u>Max Stresses (ksi)</u>
2.5	130, 150, 165, 180, 200, 220
0.167	"
0.03	"

The next model used was the 10-element uniaxial model shown in the lower half of Fig 3.2. This model was used to validate the accuracy of the 2-element model and was run at a frequency of 0.167 Hz and a maximum stress level of 200 ksi.

Two dimensional fatigue modeling was accomplished using a standard compact tension specimen geometry as shown in Fig 3.3. Due to symmetry, only half of the compact tension specimen was modeled using constant strain triangular elements. The finite element mesh shown in Fig's 3.4 and 3.5 was selected to model the top half of the compact tension specimen. This pattern allows for unlimited size reduction and insures that no two adjacent elements differ in size by more than a factor of 2. Except for elements near the loading pin holes, element aspect ratios varied from .5 to 1.0. Elements near the crack

tip have an area of  $4.8848 \times 10^{-6} \text{ in}^2$  ( $3.1494 \times 10^{-5} \text{ cm}^2$ ). Since crack growth was not specifically studied, the length of the crack was held at a constant .6630 in. The specimen thickness was established at a constant .2154 in. The loads and stress intensity factors are shown in Table 3.2.



Uniaxial Finite Element Models  
Figure 3.2

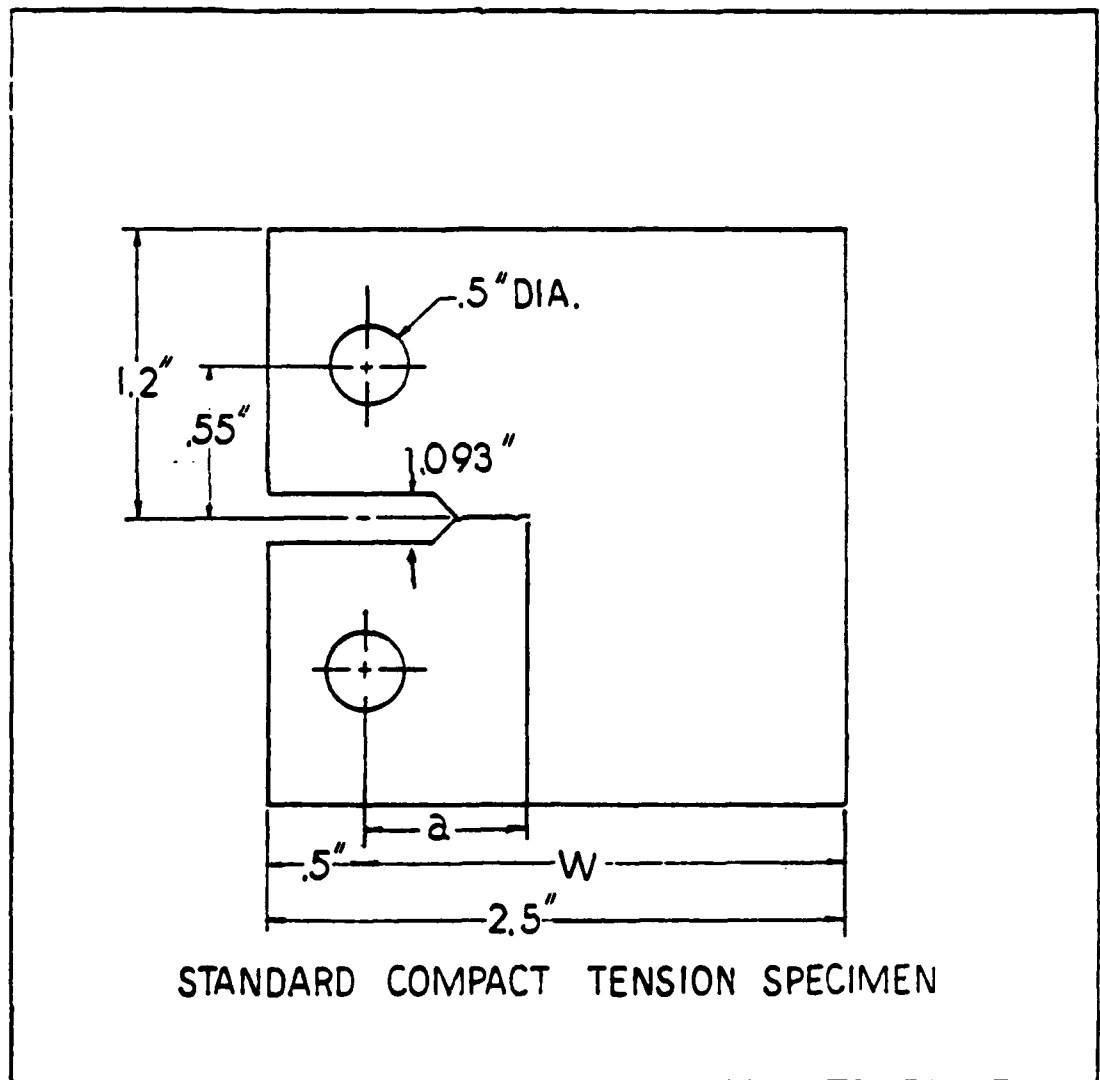


Fig 3.3 Compact Tension Specimen Geometry



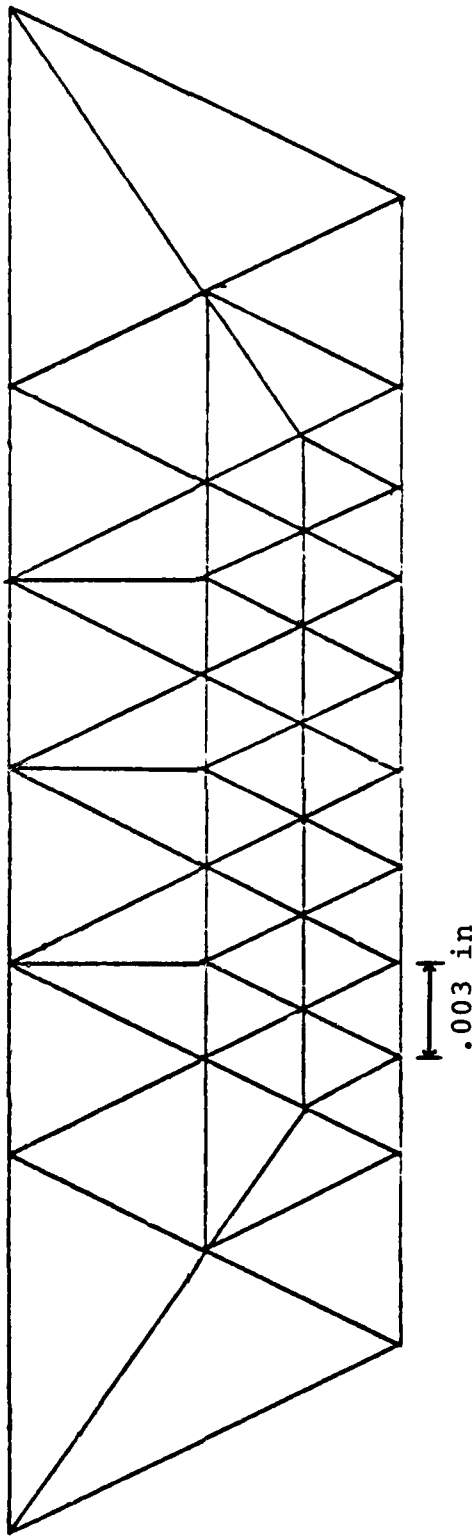


Fig. 3.5 Uniform Mesh Ahead of Crack Tip

TABLE 3.2

## COMPACT TENSION SPECIMEN LOADS AND STRESS INTENSITY FACTORS (K)

<u>K<sub>1</sub></u> (ksi in)	<u>Load</u> (lbs)	<u>R-Ratio</u>
35	1762	0.1
35	1762	-1.0
45	2265	-1.0

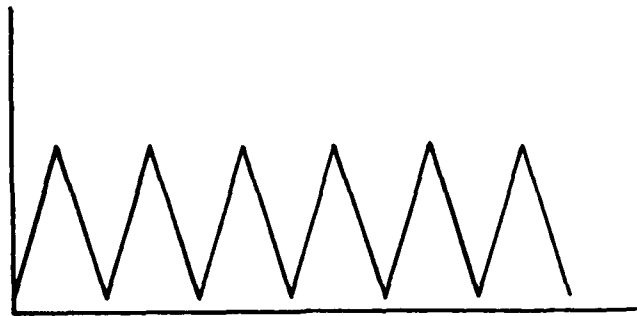
The compact tension loads are shown graphically in Fig 3.6.

Verification of Computer Program

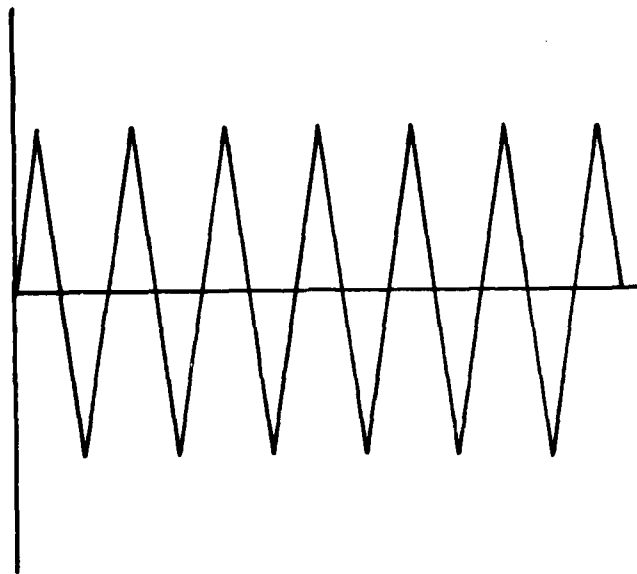
Validation of the negative cyclic subroutine and research into the non-linear response on IN-100 to fatigue loading was accomplished primarily with the 2-element uniaxial model. The crack closure algorithm was verified with a 2-dimensional mesh composed of 543 elements and 327 nodes. This mesh was used by Keck [12] in his research, which considered an R-ratio of 0.1 and is of known accuracy. Results from this mesh, which will be referred to as mesh2A, were used as a baseline in the effort to increase the number of load cycles permitted within specified computer central processor time.

Using mesh2A and given 2,000 seconds central processor time on the CDC 6600 computer, only 4 complete load cycles were possible. A new mesh was created which is composed of 382 elements and 235 nodes. This mesh is herein referred to as mesh382. Using mesh382 and given the same 2,000 seconds

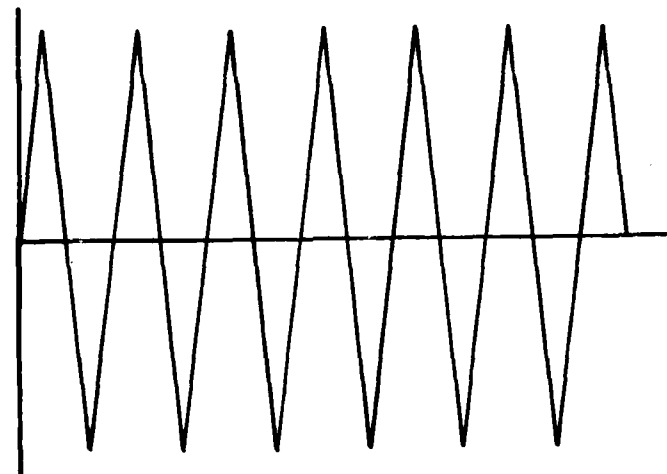
central processor time, 13.5 load cycles are possible. The differences between mesh2A and mesh382 are, the number of elements (543 vs 382), the number of nodes (327 vs 235), and the distance ahead of the crack tip where the element area increases (.078 in vs .048 in). Comparison of the results from mesh382 with the results from mesh2A show less than 3% error. This will be discussed in the results section of this study.



2.5 Hz  
R = 0.1  
k = 35 KSI  $\sqrt{IN}$



2.5 Hz  
R = -1.0  
k = 35 KSI  $\sqrt{IN}$



2.5 Hz  
R = -1.0  
k = 45 KSI  $\sqrt{IN}$

Fig 3.6 2-Dimensional Load Cases

#### IV Results and Discussion

Results and comparisons made in this chapter are divided into three major groups. The first section deals with extending existing compact tension analysis [12], which was performed with an R-ratio of 0.1, to a larger number of load cycles. The results were highly successful, with an increase of over three times the past number of load cycles now able to be analyzed. The second section is concerned with the uniaxial finite element specimen. Here is the first attempt to use VISCO for negative R-ratio load cycling. The program subroutines are verified for negative loads, and the accuracy of the solution is examined. The R-ratio used throughout this portion is -1.0 and various cyclic frequencies and load levels are examined. The final section deals with the application of reversed loading to the compact tension specimen. The R-ratio used in this section is -1.0, the load frequency is held constant at 2.5 Hz and two load levels are examined. The crack opening displacements and residual strain illustrations yield results of particular interest.

##### Positive R-ratio Compact Tension Specimen Tests

Results and illustrations in this section are derived from compact tension specimen load cycling at a frequency of 2.5 Hz, an R-ratio of 0.1, and a maximum stress intensity of  $K_I = 35 \text{ KSI } \sqrt{\text{in}}$ . The discussion is broken down into the following subsections:

- a) Comparison of results between Mesh2A and Mesh382
- b) The amount of plastic strain accumulated for each cycle
- c) Vertical (Y) displacement of the specimen behind the crack tip
- d) Cyclic stress strain behavior at the crack tip for 13 load cycles
- e) Profiles of Z hardness, Y stress and Y strain as a function of distance ahead of the crack tip for 13 load cycles

Validation of the accuracy of Mesh382 for modeling compact tension specimen behavior was accomplished by comparing results obtained with results given from Mesh2A, which is known to be accurate. Plastic zone sizes after 2.5 cycles are compared in Fig 4.1. The error between the areas of the two plastic zones is less than 2%, which is considered minor. The stress fields ahead of the crack tip for the two meshes after 2.5 cycles are compared in Fig 4.2. Again the differences in the results between Mesh382 and Mesh2A are insignificant. The third and final check on the accuracy of Mesh382 illustrated in this study, is a comparison of the specimen corner displacement through the second load cycle. From Fig 4.3, it is obvious that the displacement function for the corner of the compact tension specimen is the same regardless of which finite element mesh is used. For reasons of the above examples and other comparisons of strain, Z hardness and crack opening characteristics, it is evident that Mesh382 will accurately model the behavior of the compact tension specimen.

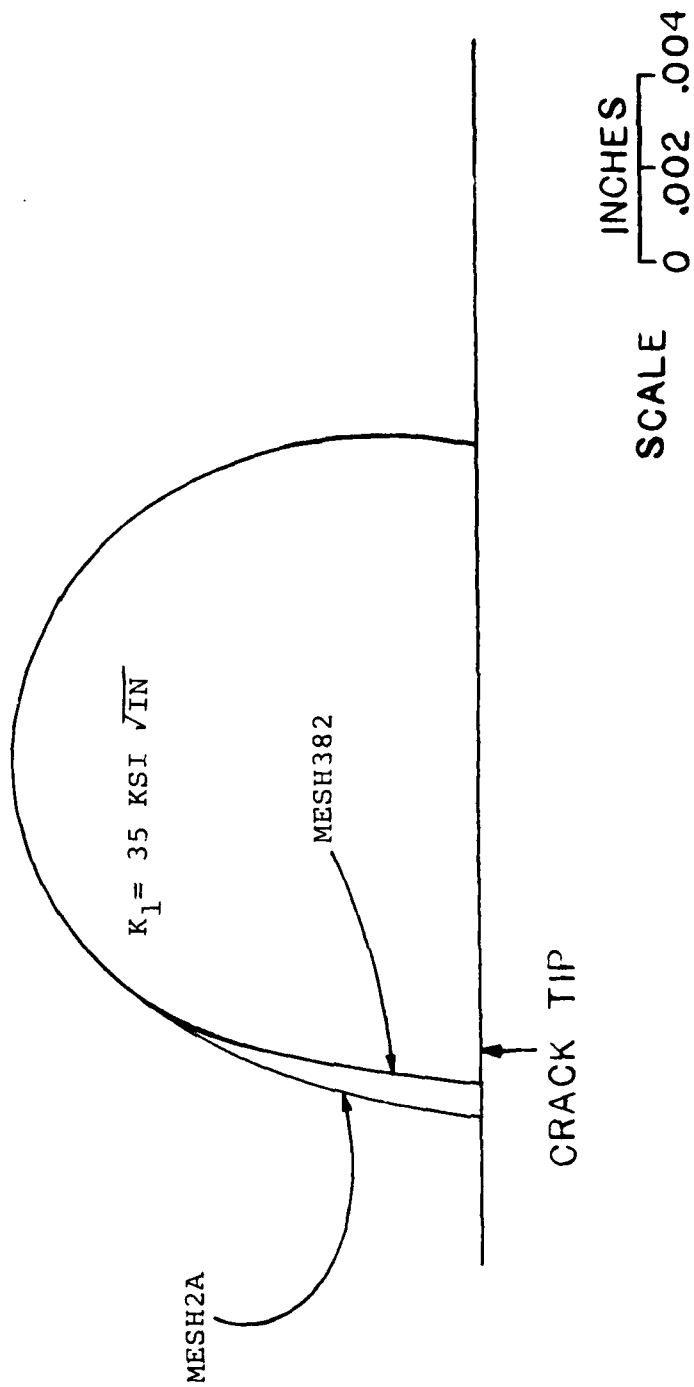


Fig 4.1 Plastic Zone After 2.5 Cycles

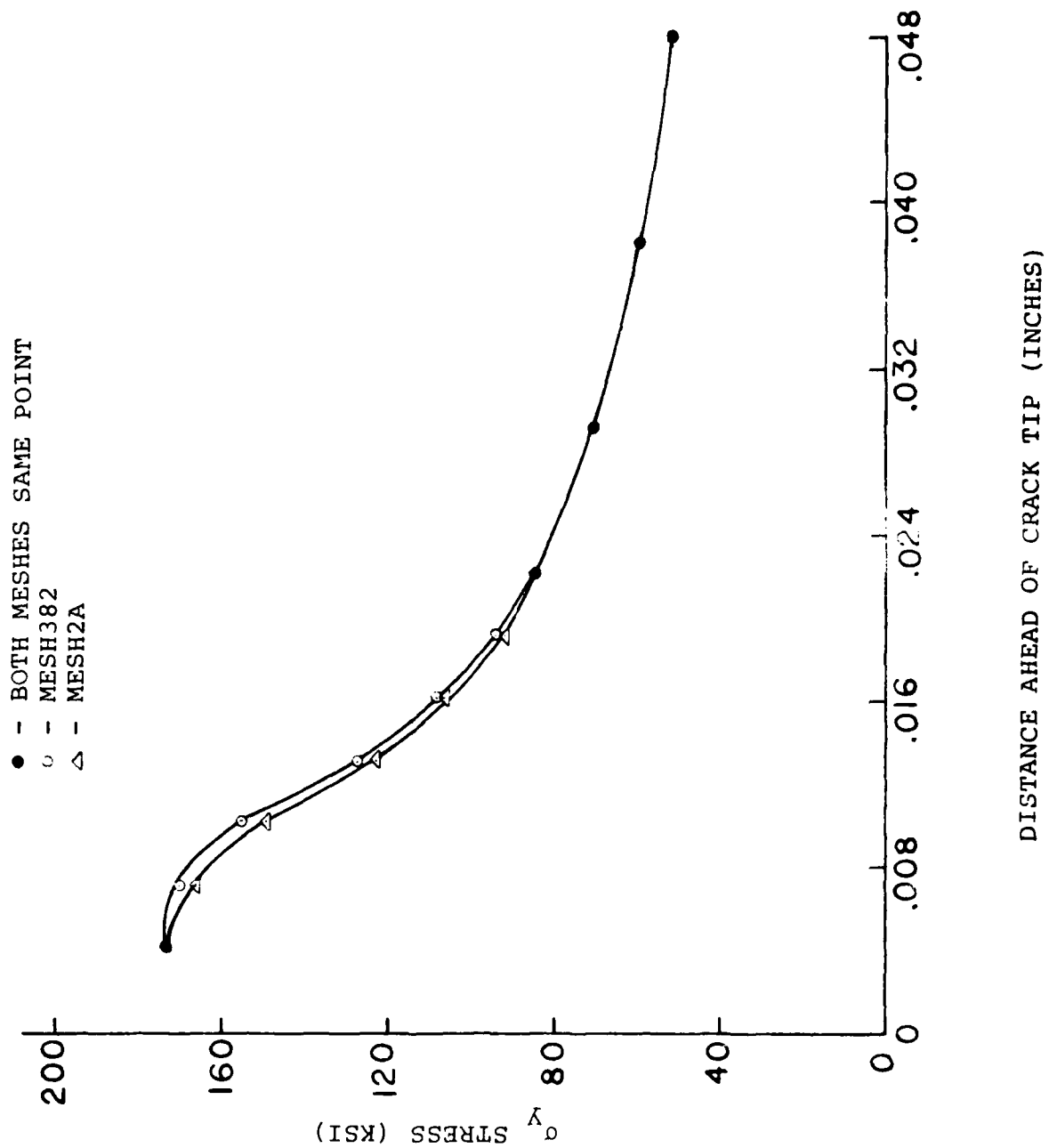


Figure 4.2 Stress Ahead of Crack Tip

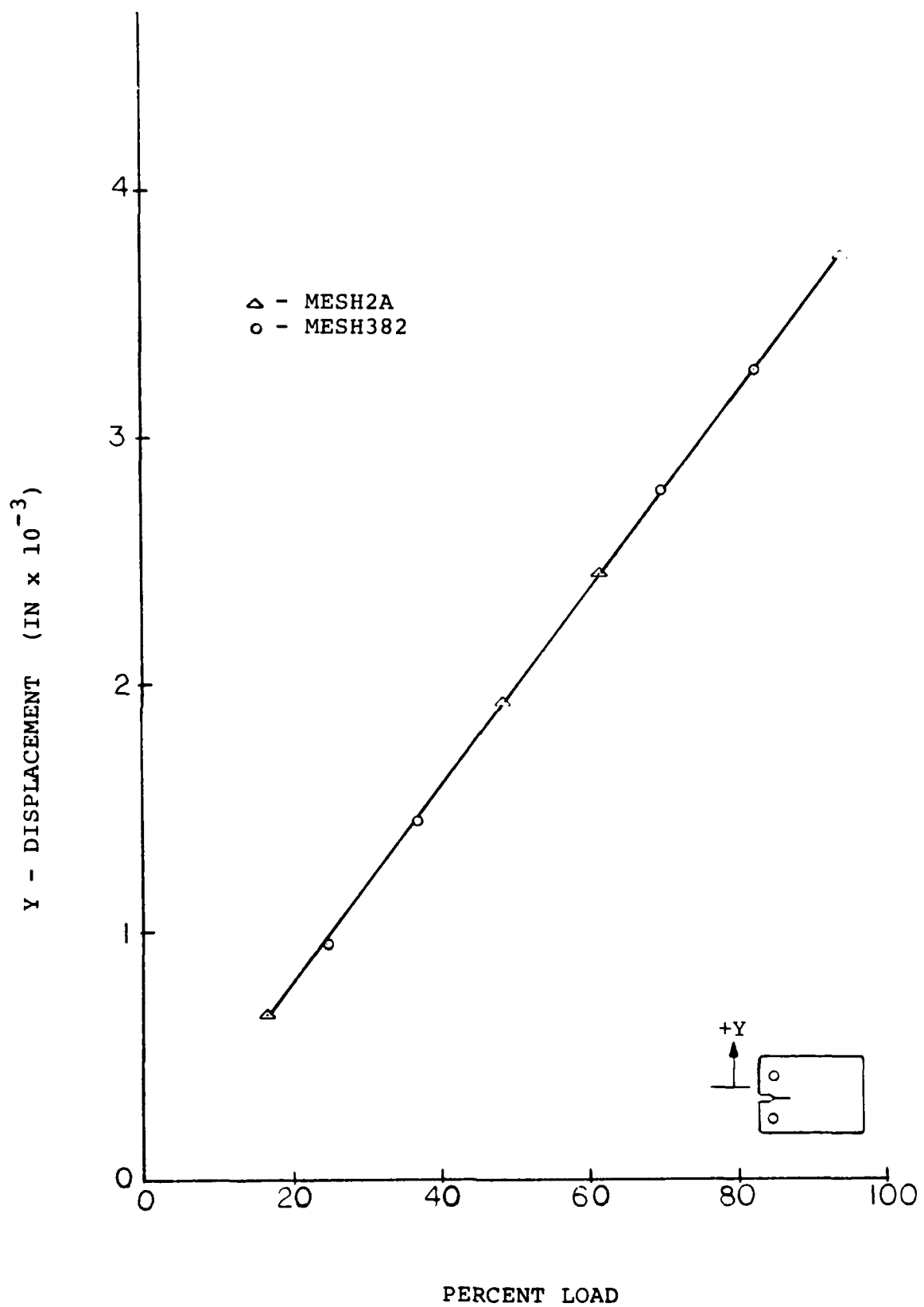


Figure 4.3 Displacement vs Load Percent During the Second Load Cycle

The benefit derived from using Mesh382 for modeling the compact tension specimen is enormous. Current research has been able to achieve only a moderate number of load cycles before computer operating time becomes prohibitive. For example, Mesh2A, which has 543 elements (327 nodes), allows somewhat less than four complete load cycles. With equal accuracy, Mesh382 is able to complete 13.5 cycles in the same amount of computer time.

The first area to be examined over the 13 load cycles, with a  $K_I$  value of 35 KSI  $\sqrt{\text{in}}$ , was the total strain over time ahead of the crack tip. Earlier work on a low number of load cycles indicated that a stable stress/strain condition exists at the crack tip after the first load cycle [12]. There appeared to be a constant accumulation of plastic strain at each cycle in the material ahead of the crack tip. This behavior has little physical appeal, because materials do not normally strain without bound under the conditions imposed by the compact tension specimen test. The evidence through 13 load cycles refutes the concept of a stable stress/strain condition ahead of the crack tip. The amount of plastic strain accumulating ahead of the crack tip is decreasing in an exponential fashion. This suggests that after an appropriate number of load cycles, the total strain will reach a stable state and no further plastic straining will occur. Table 4.1 illustrates the value of the total strain after each load cycle for the first element ahead of the crack tip along with the change in strain from the previous load cycle. This data is presented in Fig 4.4.

TABLE 4.1

## TOTAL STRAIN VALUES AFTER EACH LOAD CYCLE

<u>Cycle</u>	<u>Strain(in/inx10<sup>-3</sup>)</u>	<u>Strain Increase(in/inx10<sup>-3</sup>)</u>
0	0.0	0.0
1	14.03	14.03
2	15.25	1.22
3	16.07	.827
4	16.58	.51
5	17.0	.42
6	17.33	.33
7	17.60	.27
8	17.84	.24
9	18.09	.25
10	18.29	.20
11	18.49	.20
12	18.67	.18
13	18.81	.14

Extrapolation of the data in Fig 4.4 indicates that after approximately 23 load cycles, no more plastic straining will take place (see Fig 4.5). Data retrieved at this point could therefore be utilized to model material characteristics during fatigue tests of possibly several thousand cycles.

To check for crack closure, vertical (y) displacements behind the crack tip were monitored during the unload cycle for each of the 13 load cycles examined in this study. As shown in Fig 4.6, no negative displacements are observed,

indicating no crack closure. This is to be expected as the minimum load still applies a tension in the specimen near the crack tip due to the positive R-ratio of 0.1.

The displacement of the corner of the crack mouth for the first load cycle is shown in Fig 4.7. When this figure is superimposed over the crack mouth displacement for the second load cycle shown in Fig 4.3, it is found that the slopes of the curves are identical. Throughout the 13 load cycles examined in this study, there was no change in the plot of crack mouth displacement vs load. The results show that the compact tension specimen behaves elastically at points on the specimen boundary and does not see the localized inelastic behavior near the crack tip.

Fig 4.8 illustrates the stress/strain behavior for the first element ahead of the crack tip. Shown are the first four cycles, and then cycle numbers 8 and 13. A rapid increase in plastic deformation occurs during the first load cycle. Each successive cycle has less plastic deformation until, as shown earlier in Fig 4.5, the plastic strain per cycle goes to zero. After about 23 cycles then, linear elastic stress strain behavior is established. The constant amplitude of stresses each cycle suggests that the material ahead of the crack tip is essentially in a stress controlled boundary condition.

The behavior of the Bodner Z hardness material parameter is illustrated in Fig 4.9. The elements immediately ahead of the crack tip along the line of symmetry reach saturation value within the first load cycle. Elements which are farther

out than 2.4% of the crack length ahead of the crack tip see no change from the initial hardness value specified. The elements in between show a slight increase in their hardness value through approximately three load cycles where no more increase is indicated.

The stress and strain fields ahead of the crack tip are shown in Figs 4.10 and 4.11. The stress magnitude is relatively constant over all 13 load cycles, supporting the suggestion of stress controlled boundary condition. The strain field shows a slight increase over the 13 cycles with the majority occurring early in the load history. This is again showing the trend towards a stable strain-time history after approximately 23 load cycles.

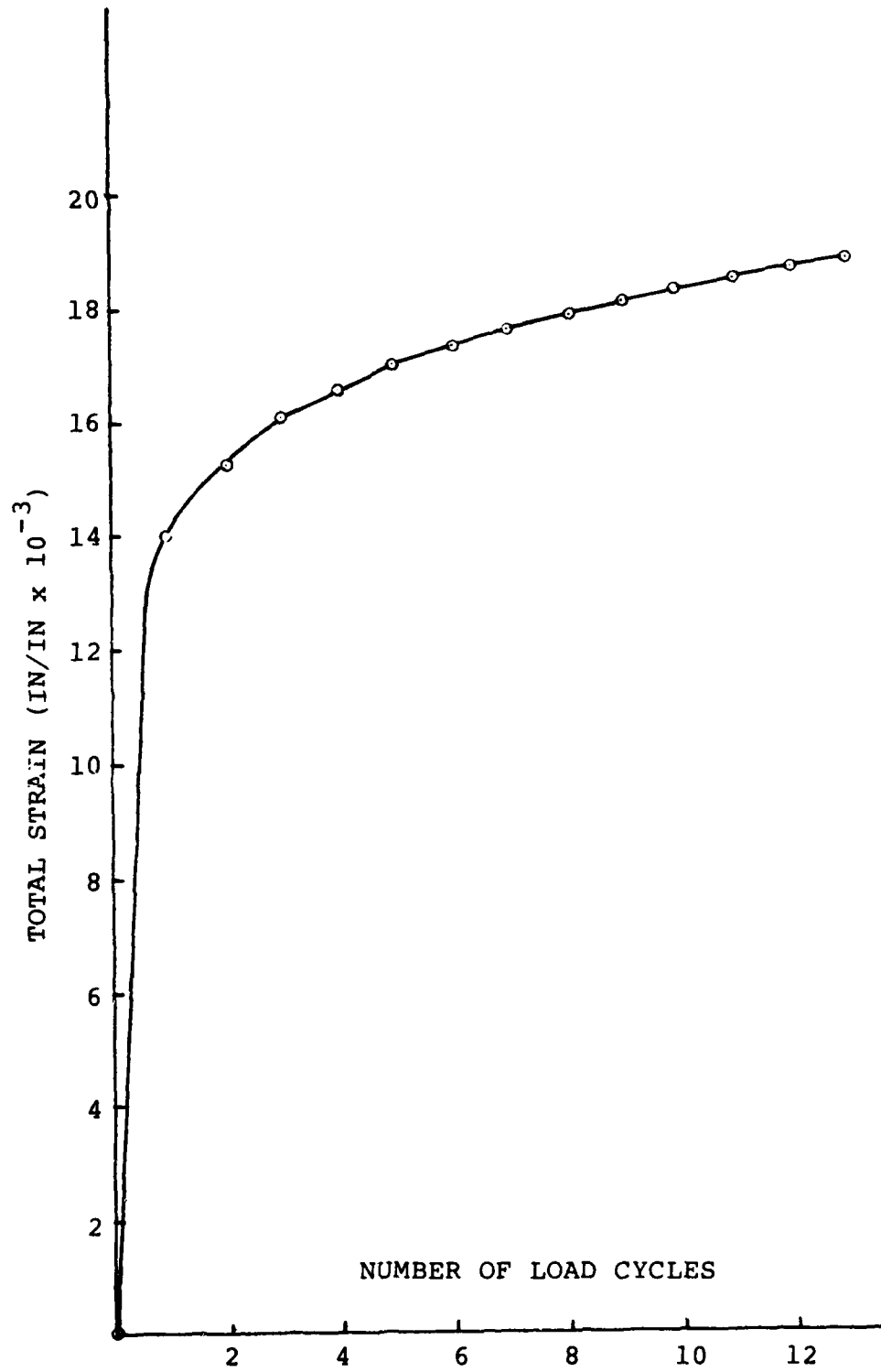


Fig 4.4 Total Strain After Each Cycle  
.002 in Ahead of the Crack Tip

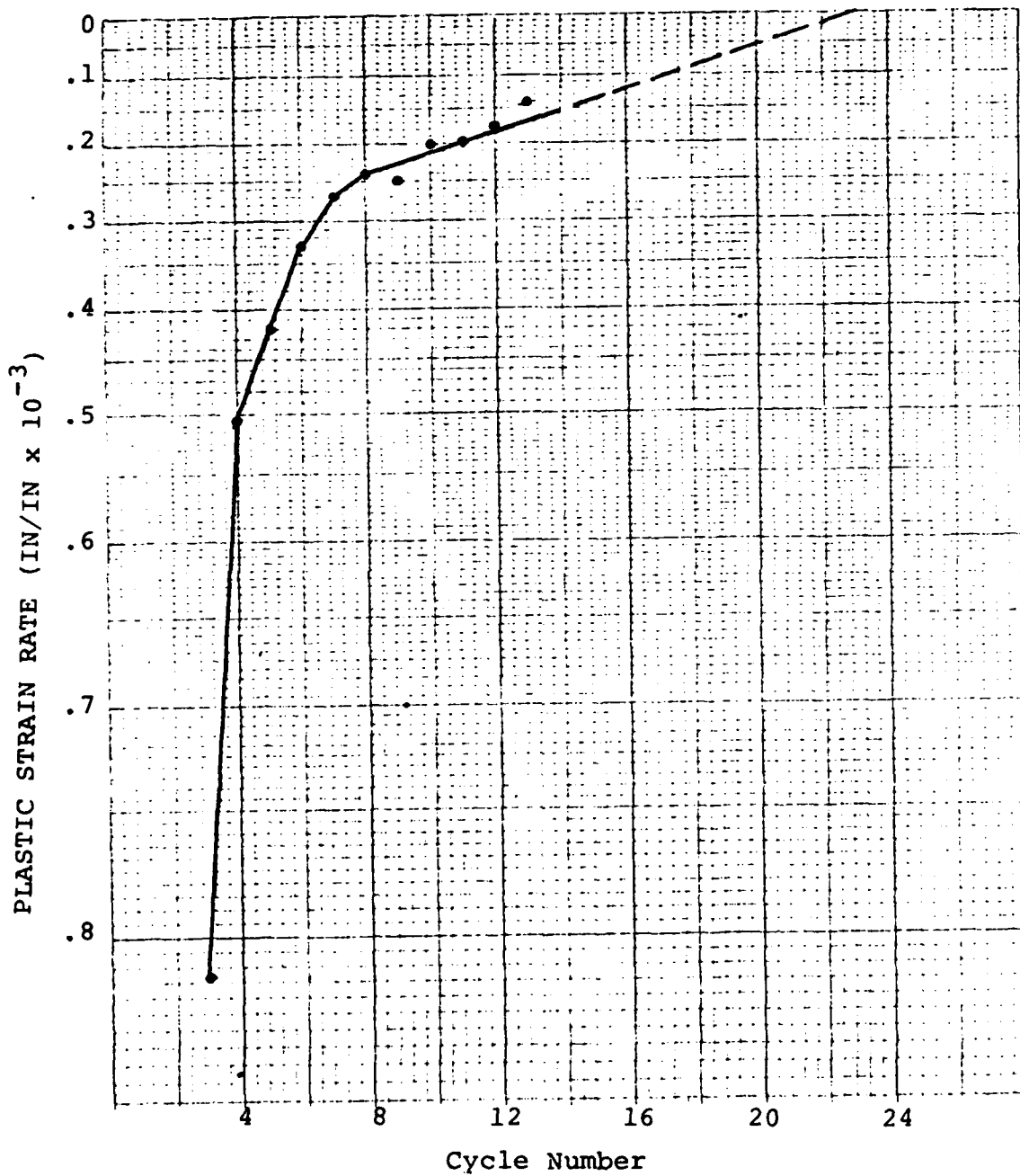


Fig 4.5 Projected Number of Cycles Required for Stabilization

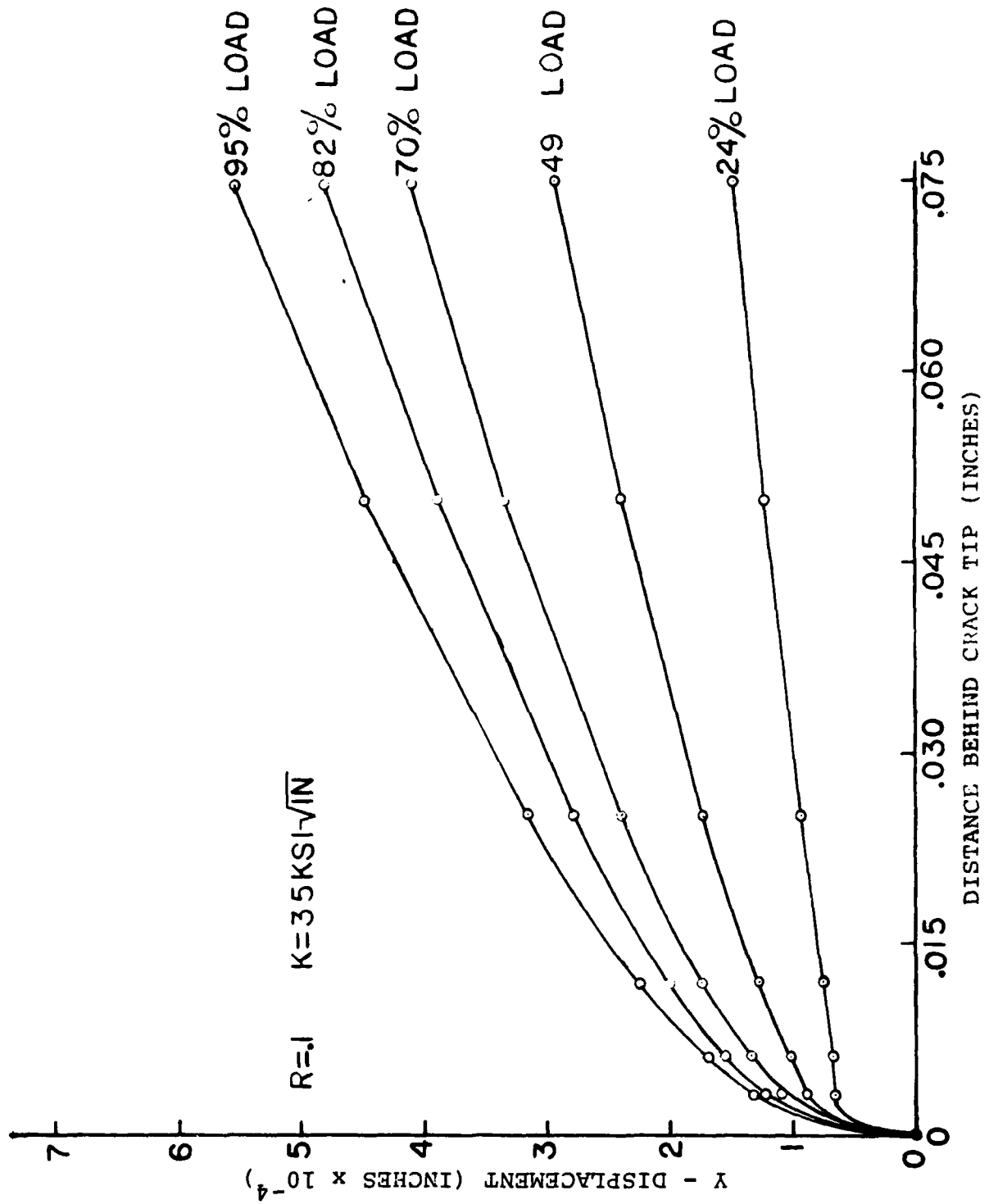


Fig 4.6 Y-Displacement vs Distance Behind Crack Tip

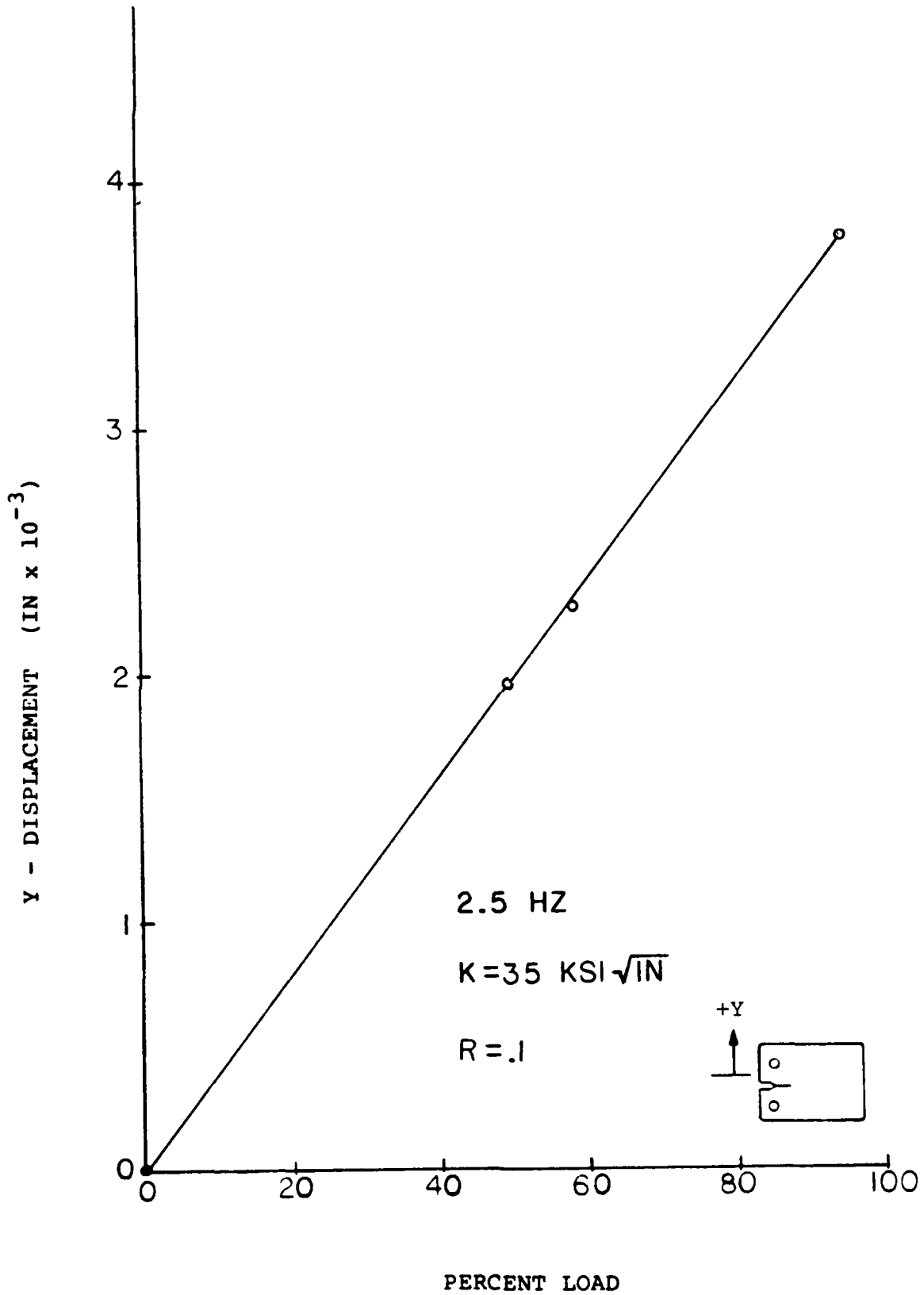


Fig 4.7 Y-Displacement vs Percent Load

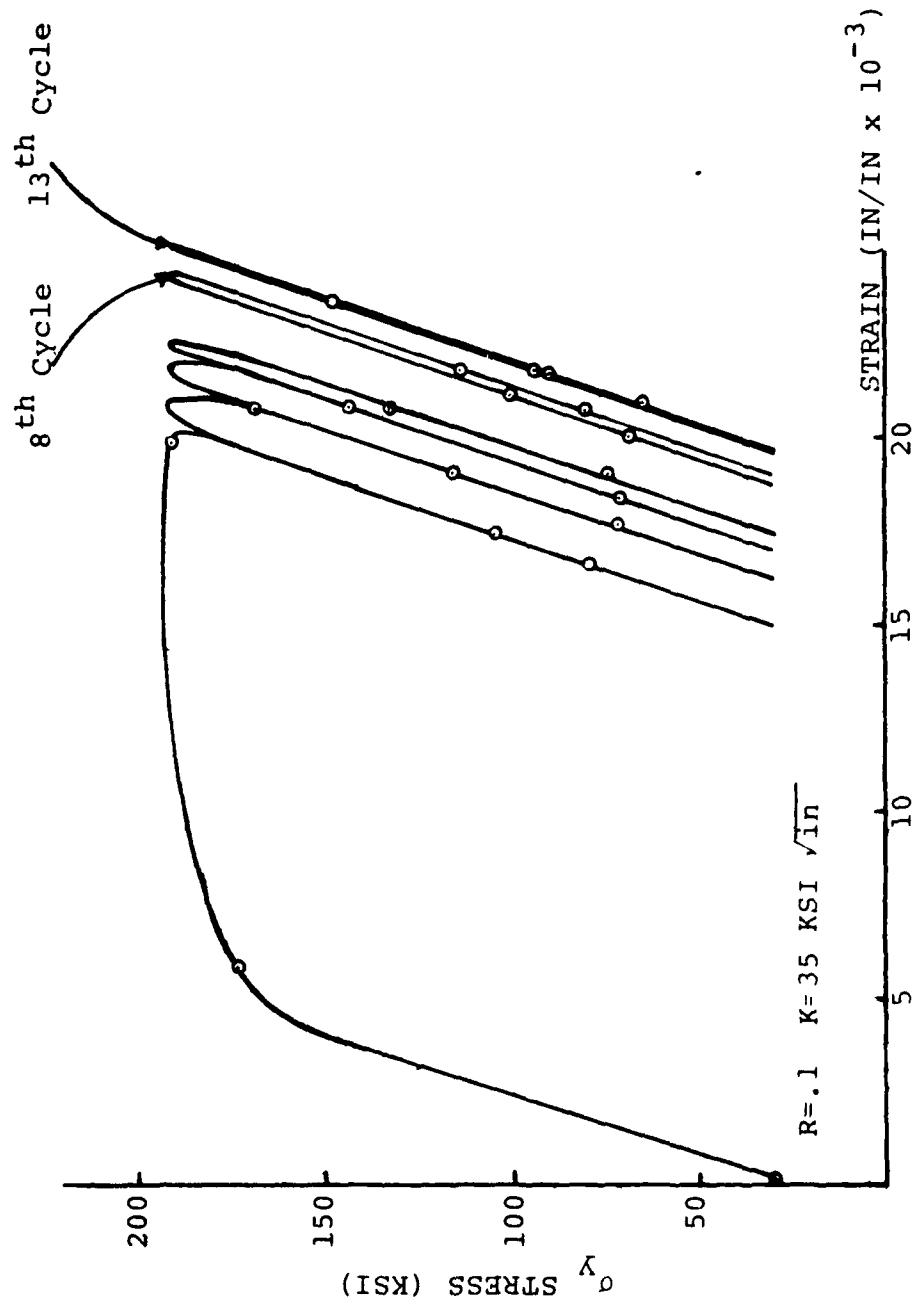


Fig 4.8 Compact Tension Specimen Stress/Strain Behavior

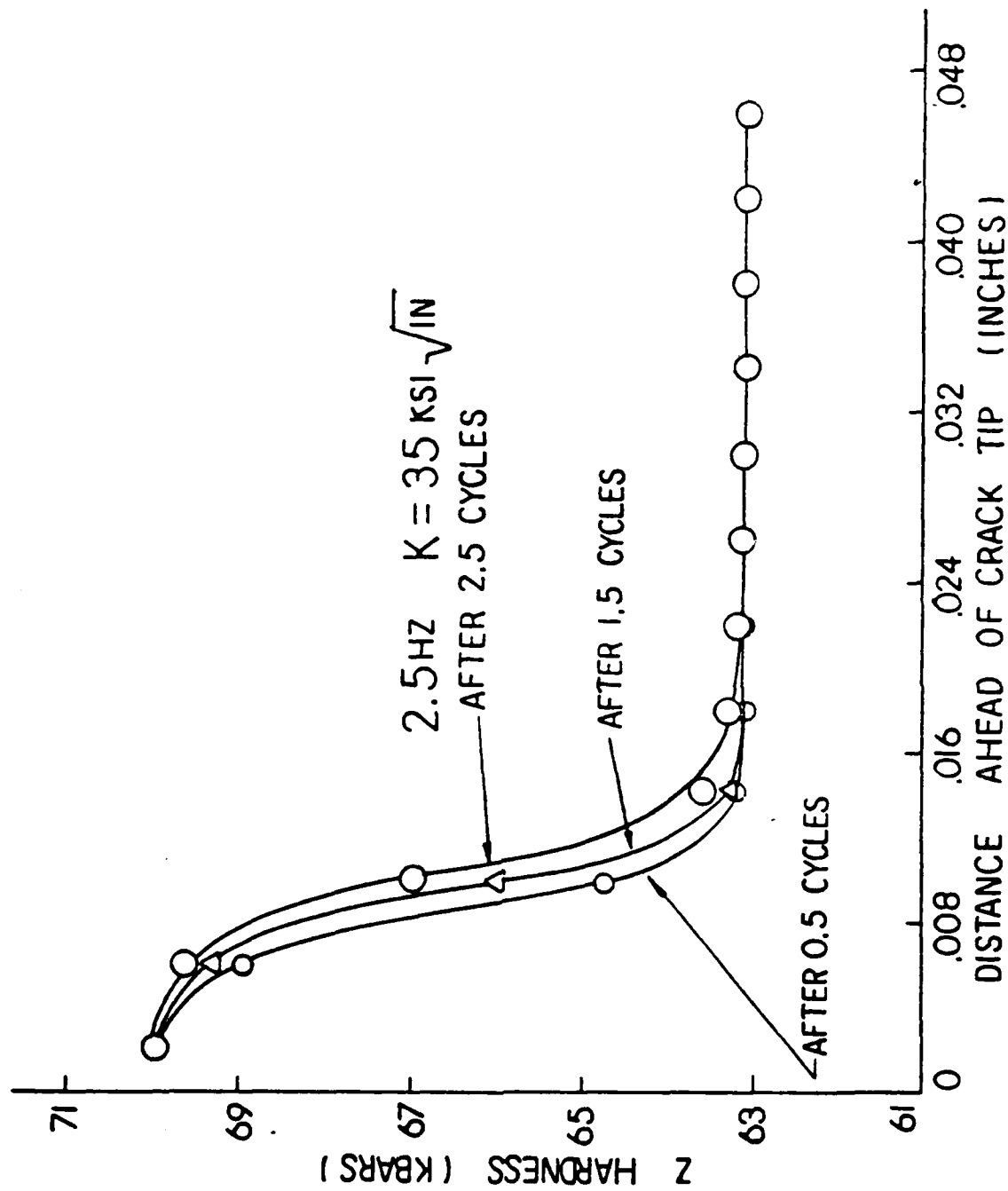


Fig 4.9 Z Hardness vs Distance Ahead of Crack Tip

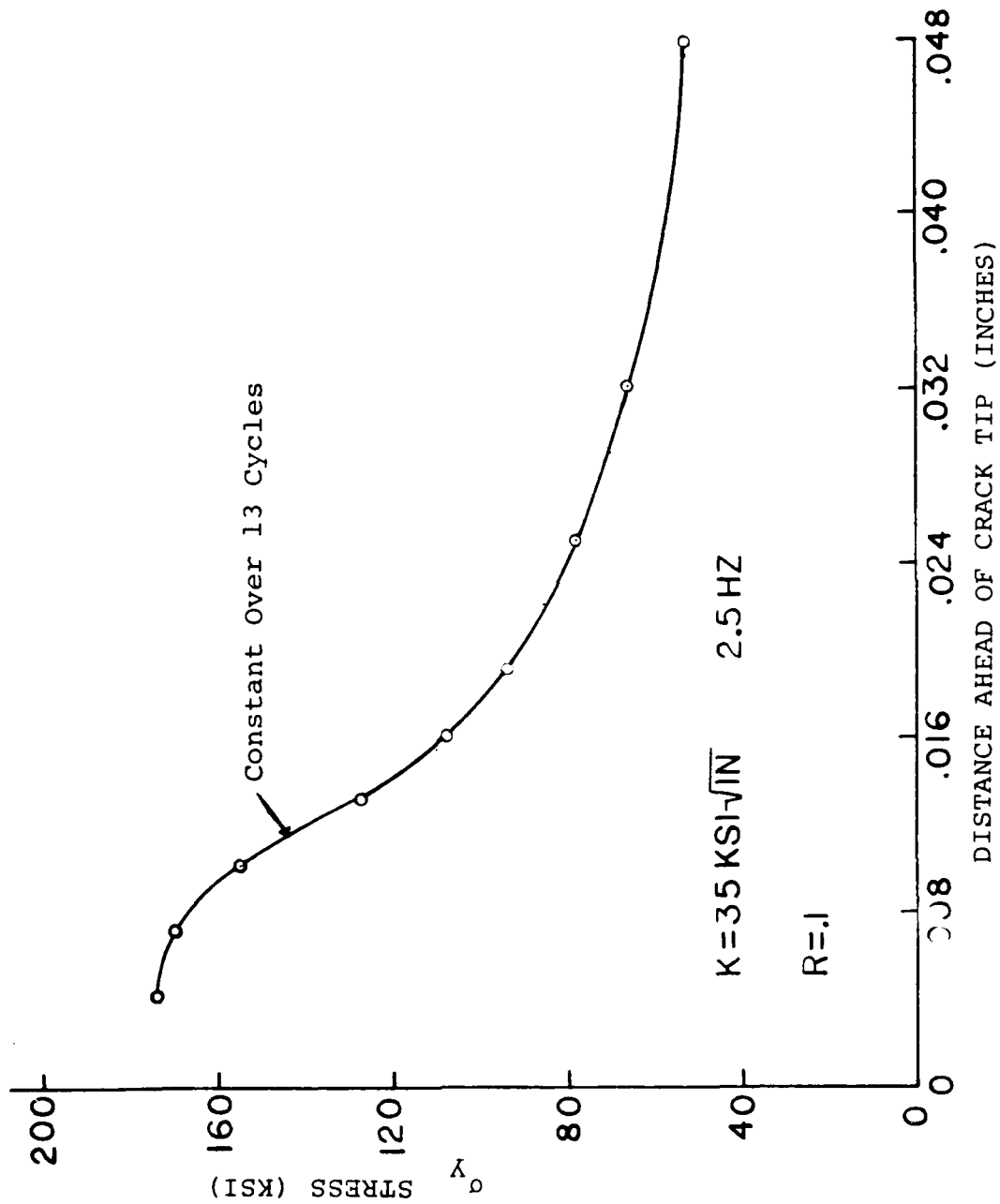


Fig 4.10 Y Stress vs Distance Ahead of Crack Tip

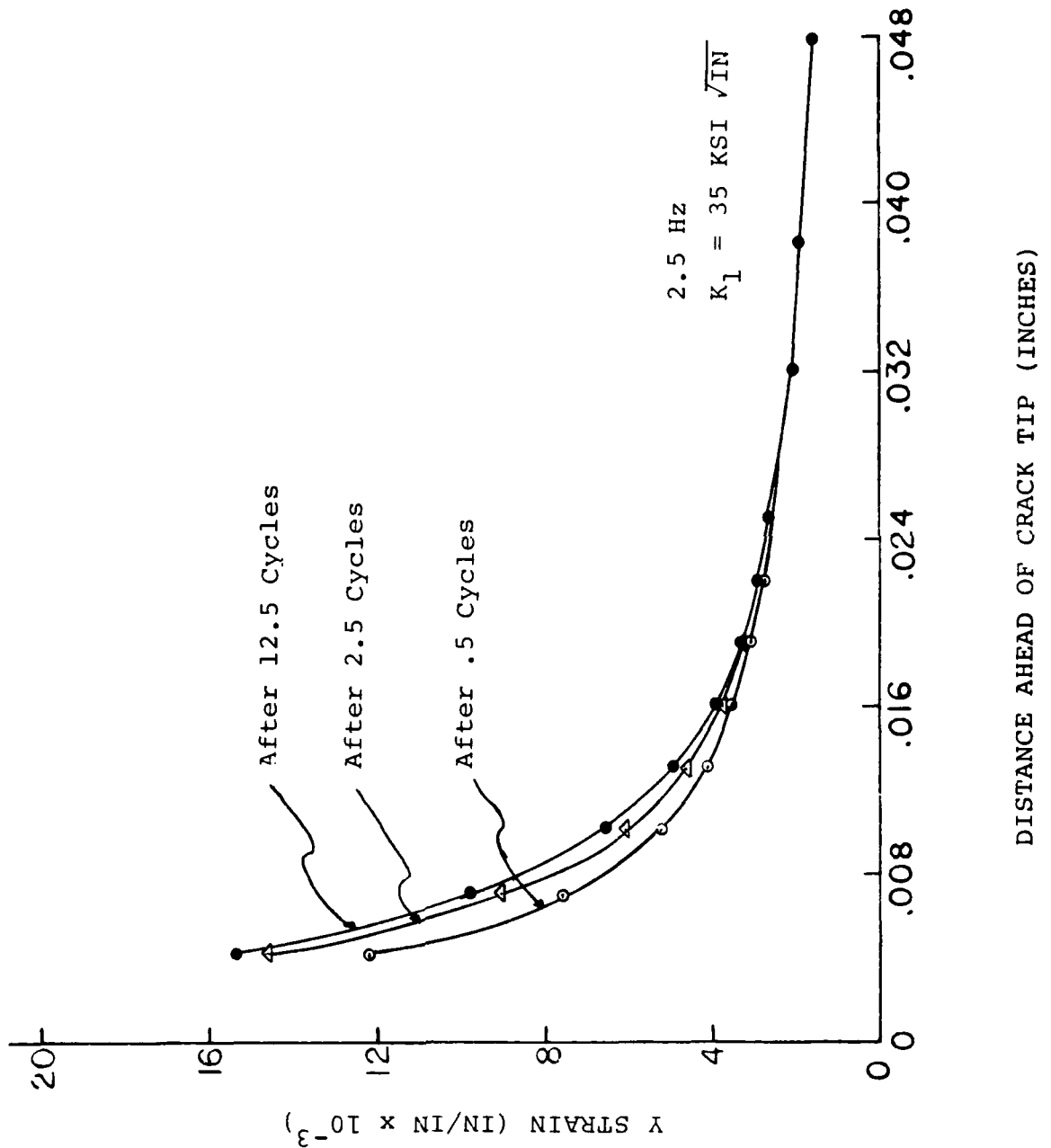


Fig 4.11 Y Strain vs Distance Ahead of Crack Tip

### Negative R-Ratio Uniaxial Results

Three major areas of concern were examined with the uniaxial models shown in Fig 3.2. First, the subroutines in VISCO for reversed loading had to be verified. Next, the behavior of IN-100 under reversed loads was examined. This data was extracted to provide a baseline for the behavior of the 2-dimensional compact tension specimen. Third, and last, was to examine the accuracy of VISCO for reversed loading.

An accurate stress/strain solution for the Bodner Viscoplastic equations with uniaxial loading under high stress levels is one in which the strain increases until the material fully strain hardens. After this point, the stress/strain loops for each cycle will overlay each other exactly [13,14]. The accuracy of VISCO is partially determined by the input parameters  $\sigma_{tol}$  and  $\epsilon_{tol}$  which are the stress and strain tolerances respectively. These values dictate the overall incremental iteration which is a function of the time step. In VISCO the time step  $dt$ , for time step  $i$  is

$$dt^i = \frac{dt^{i-1}}{P} \quad (4.1)$$

where  $P$  is the greater of  $P_\sigma$  and  $P_\epsilon$ .

$$P_\sigma = \frac{\sigma_e^i - \sigma_e^{i-1}}{\sigma_e^{i-1} \sigma_{tol}} \quad P_\epsilon = \frac{(d\epsilon_e^P)^i}{\epsilon_{total}^i \epsilon_{tol}} \quad (4.2)$$

If the time step is not set to the correct value, minor error will result and the stress/strain curves will not exactly overlay each other. The stress and strain tolerances, unless otherwise specified, were each set at 0.05.

At 2.5 Hz with stress levels at or below 150 KSI (see Figs 4.12, 4.13) the uniaxial model behaved elastically. A steady state stress/strain solution is realized immediately. When the stress is evaluated to 165 KSI (see Fig 4.14), some small amount of plasticity is evident, but a stable stress/strain solution is present immediately. Fig 4.15 illustrates the larger plastic strain present in the first load cycle for a stress level of 180 KSI. The material hardens so that after the first cycle, a stable solution is seen where the stress/strain loops directly overlay each other. Some variability in the solution is evident for stresses of 200 and 220 KSI (see Figs 4.16, 4.17). This is due to the slight variations in the time step algorithm discussed in equations 4.1 and 4.2. Neglecting the slight variations, a stable stress/strain solution is present after the first load cycle.

At .167 Hz, the only perfectly elastic stress/strain behavior is at 130 KSI (see Fig 4.18). When the stress level is raised to 150 KSI, a stable solution is reached after the first load cycle, as illustrated in Fig 4.19. Raising the stress level to 165 or 180 KSI introduces some minor variability in the solution as shown in Figs 4.20 and 4.21. It is evident that the material should see a steady stress/strain solution after the first cycle. Again the largest plastic

deformation occurs during the first load cycle. At stress levels of 200 and 220 KSI a large amount of plasticity, and consequently a relatively larger amount of error is seen in the solution (see Figs 4.22 and 4.23). According to the Bodner Viscoplastic equations, the stress/strain loops should overlay one another. The characteristics of the largest amount of plasticity occurring during the first cycle is evident even in these two figures.

At 0.03 Hz, stable elastic-plastic behavior was given for stress levels up to and including 165 KSI (see Figs 4.24-4.26). Little variation in the solution is noted after the first cycle. Input stresses of 180 and 200 KSI, however, produced a non-stable solution. Figs 4.27 and 4.28 show the same type of increasing strain present in Figs 4.22 and 4.23. Again, this variation is due to the time step algorithm and indirectly due to the input stress and strain tolerances. If the yield stress of IN-100 at 1350 F is set at 130 KSI, which is where the stress/strain curve becomes non-linear, then a load of 220 KSI is significantly higher than that value, and if applied for more than a small amount of time, should lead to excessive strain rates. This is indeed the case as shown in Fig 4.29. Convergence to a solution was not possible with this load input, so the stress/strain behavior for the first portion of the cycle is shown. At this point, the time step became smaller than the minimum value allowed by the CDC 6600 computer and no further computation was possible.

Two alternatives were examined to attempt to eliminate the variability in the solution present at higher stress levels and lower frequencies. First the 10-element model of Fig 3.2 was created to eliminate any errors from pin and roller connections present in the 2-element model, which are not realistic for uniaxial specimen. The stress and strains of elements five and six were averaged and then plotted over four load cycles in Fig 4.30. The input stress and frequency were identical to that of Fig 4.22. The tightening of the stress/strain loops towards the point where they would begin to overlay each other indicates that the 10-element model is a step towards a more accurate solution. The other alternative was to decrease the stress and strain error tolerances. The results when the tolerances were decreased from 0.05 to 0.02 are shown in Fig 4.31. Here a significant move towards the stress/strain loops directly overlaying each other is evident. Since the most accurate uniaxial results were obtained with the 2.5 Hz input frequency, the negative cycling of the 2-dimensional compact tension specimen was accomplished at 2.5 Hz.

The Bodner  $Z$  hardness parameter is illustrated in Figs 4.32-4.34. The value of  $Z$  is dependent on stress level, frequency and time. In Fig 4.32, which shows the  $Z$  hardness values for 2.5 Hz, the 220 KSI stress level saturates within the first load cycle while the 130 KSI stress level remains at the input value. Similar results are seen in Fig 4.33 for a frequency of .167 Hz. For 0.03 Hz, shown in Fig 4.34, the value of  $Z$  reaches its maximum within the first load cycle

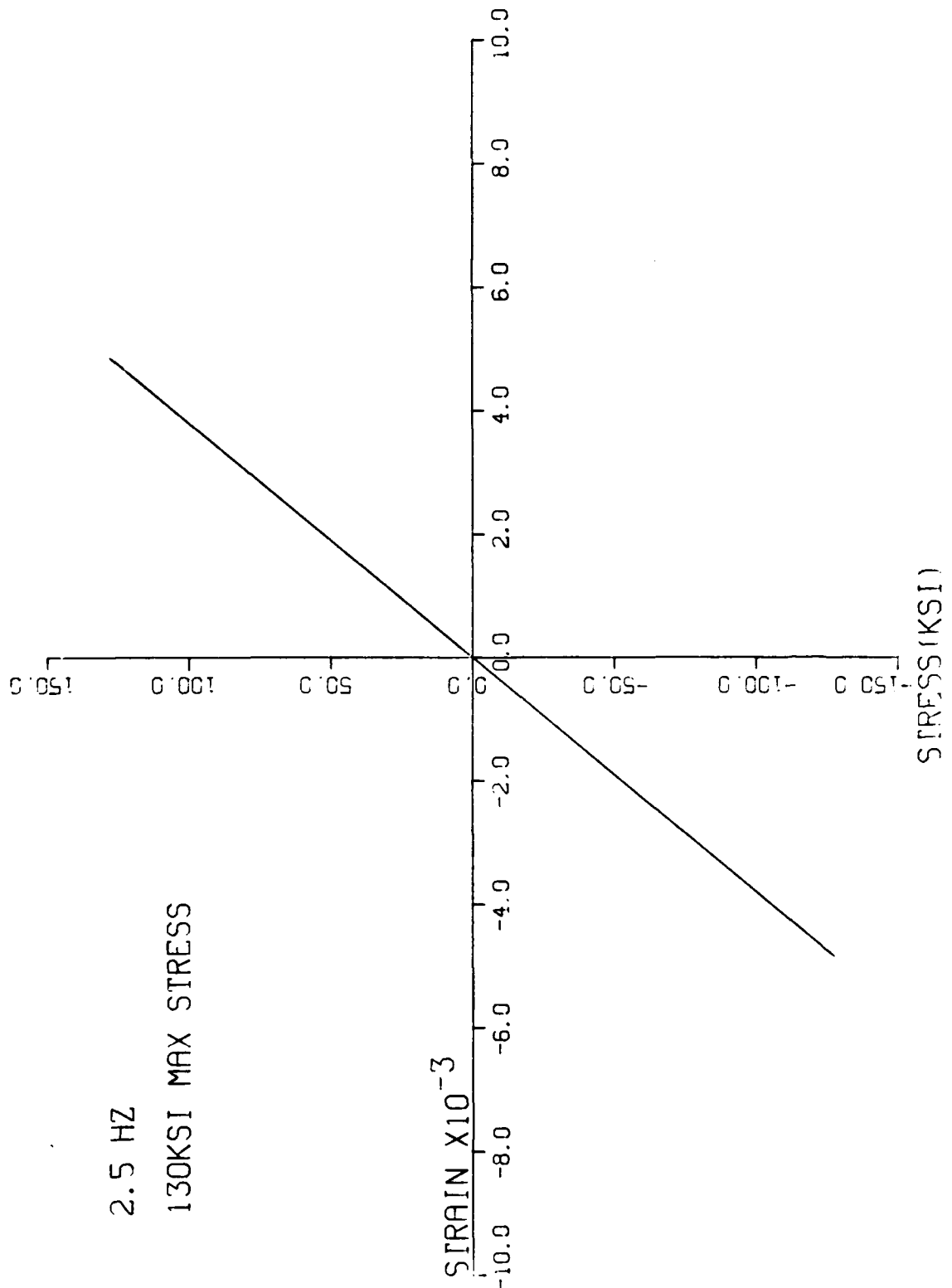


Fig 4.12 Stress/Strain Behavior Over Five Cycles

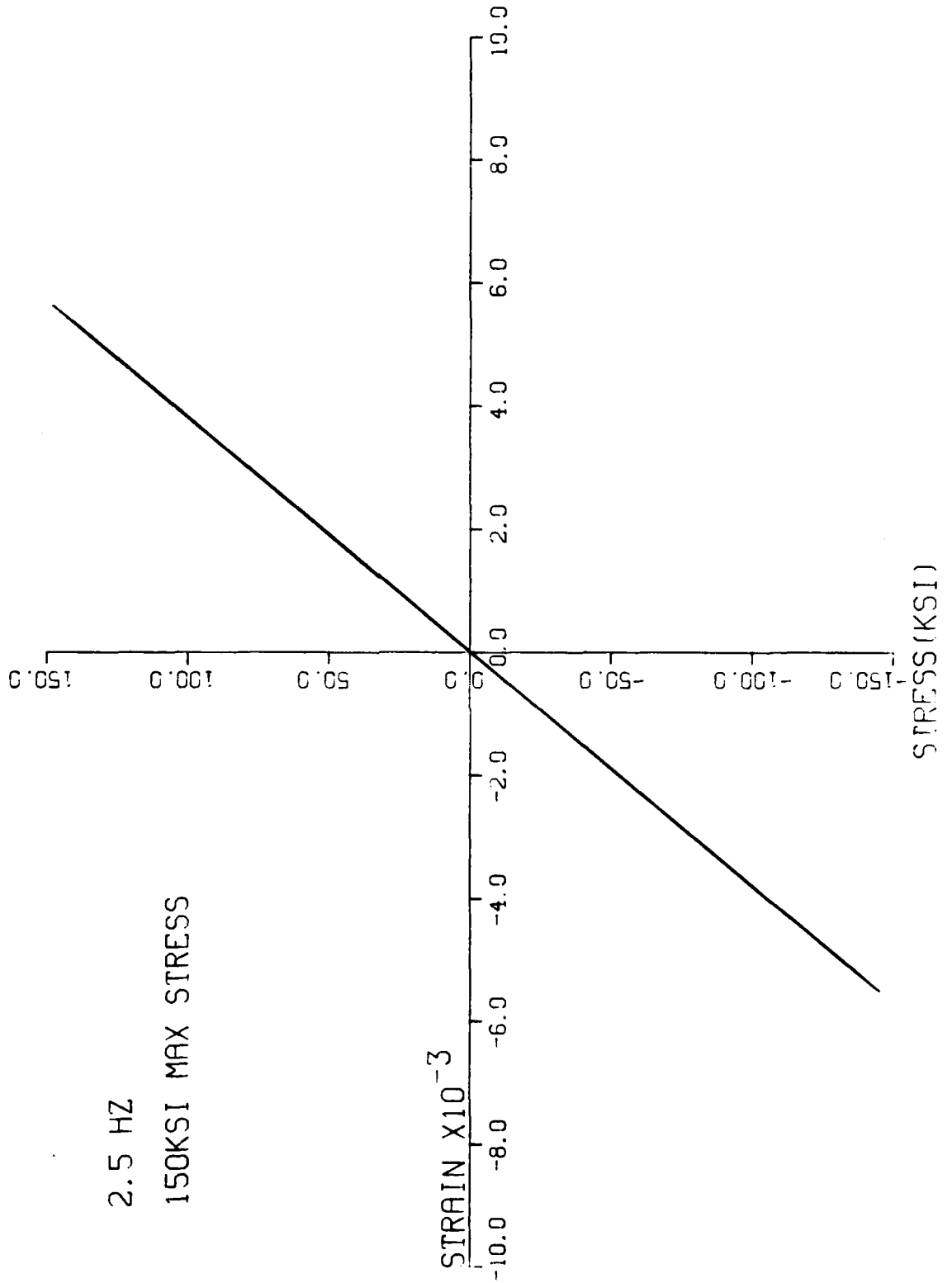


Fig 4.13 Stress/Strain Behavior Over Five Cycles

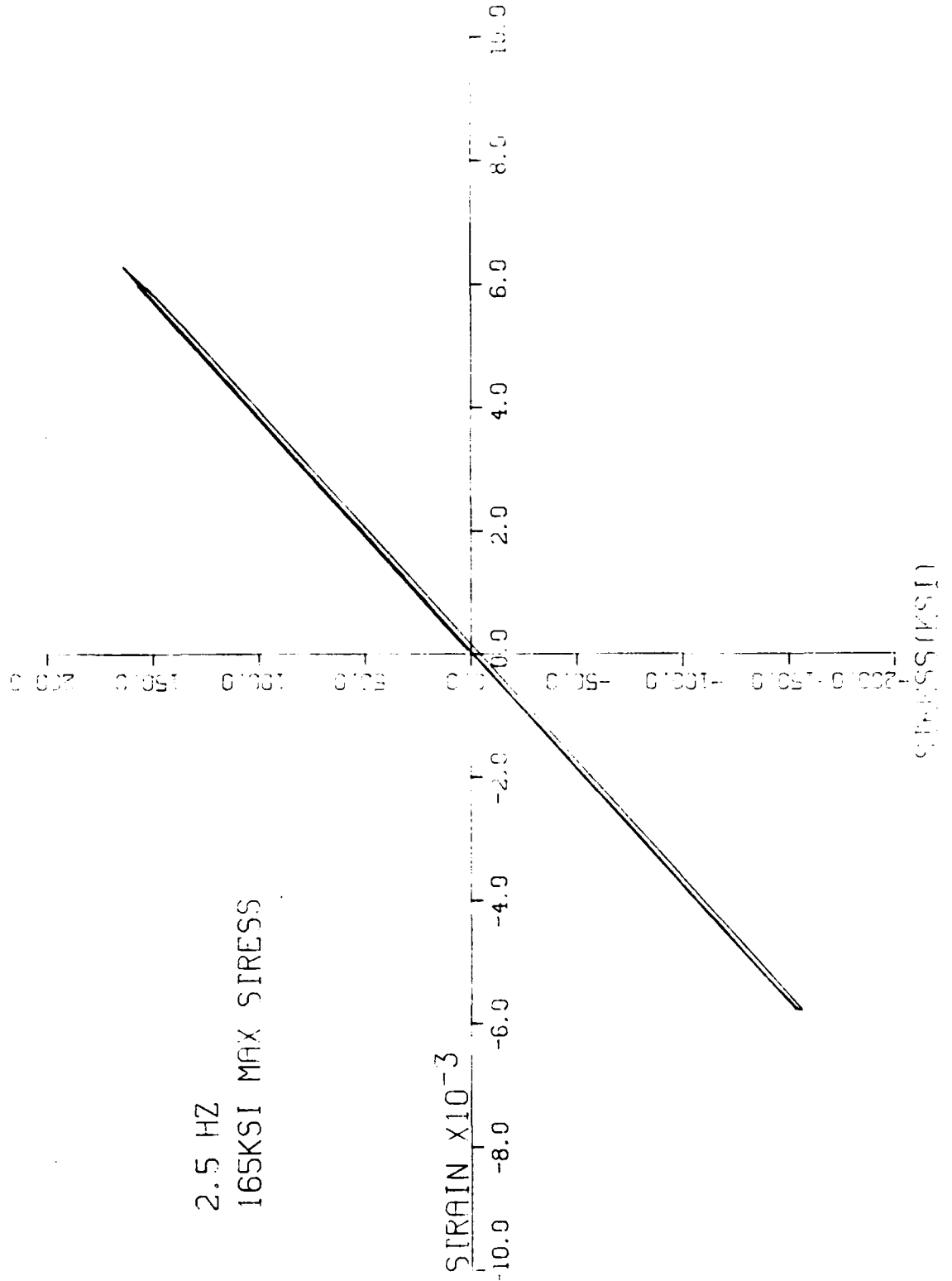


Fig 4.14 Stress/Strain Behavior Over Five Cycles

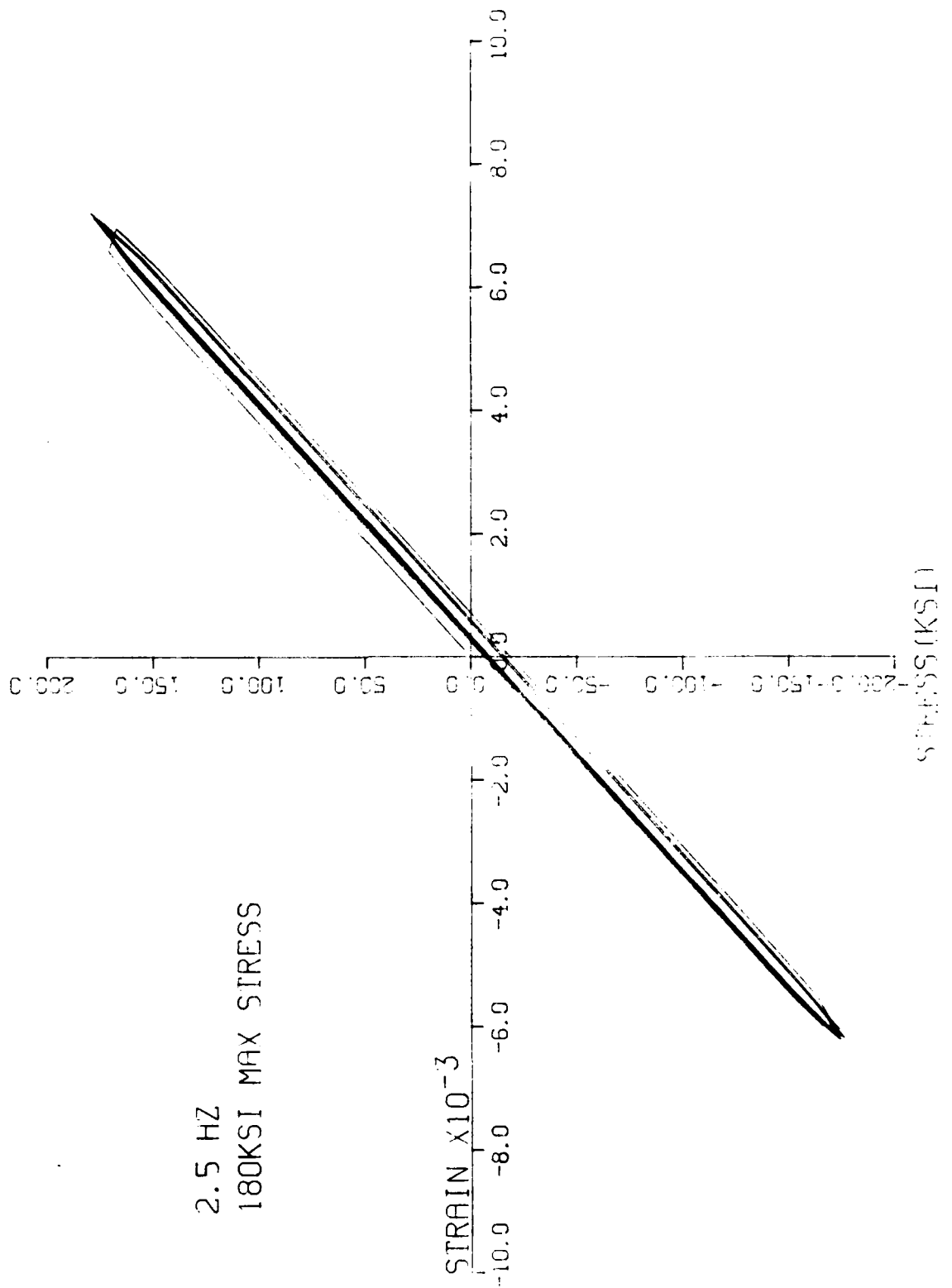


Fig 4.15 Stress/Strain Behavior Over Five Cycles

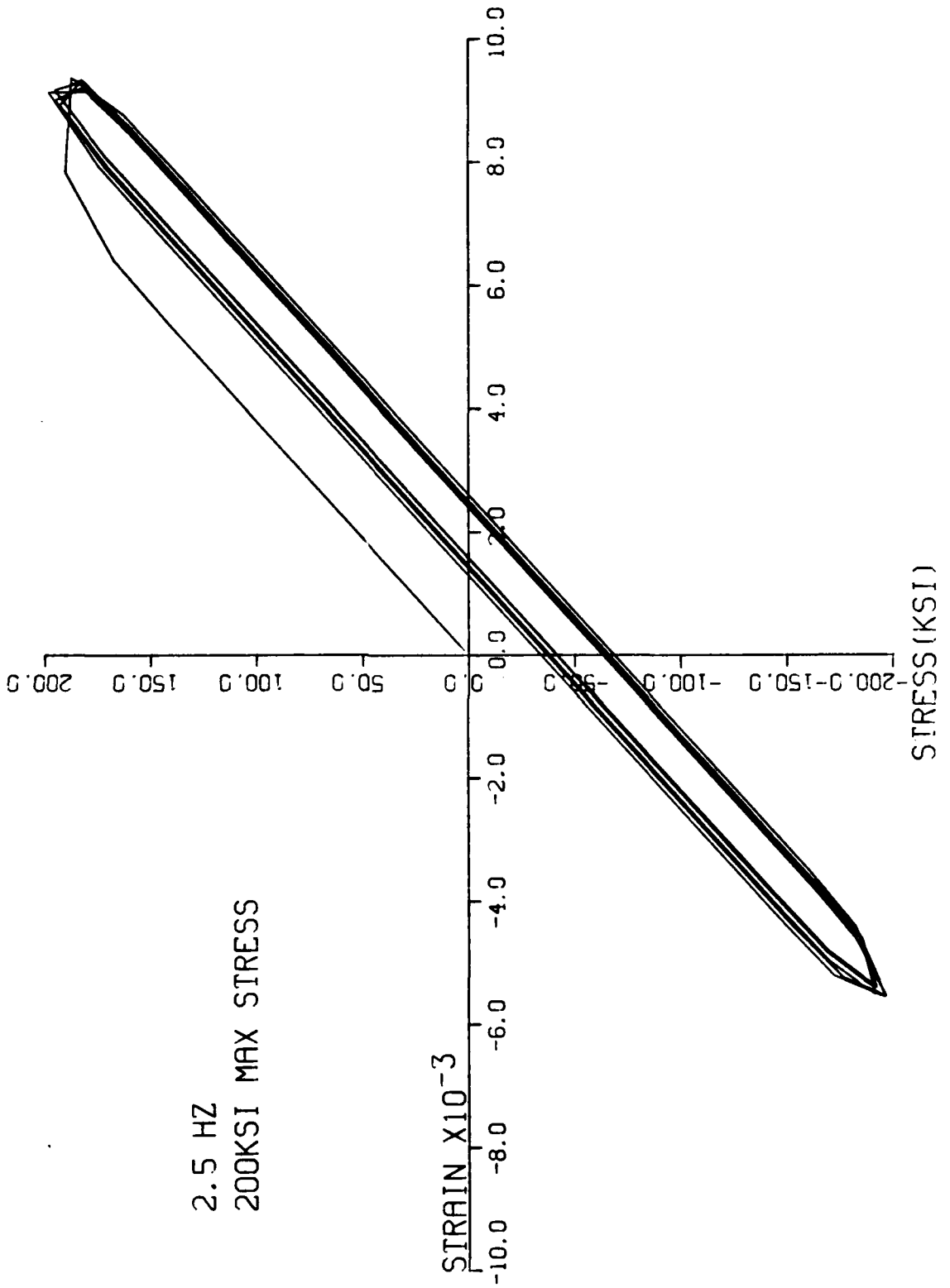


Fig 4.16 Stress/Strain Behavior Over Five Cycles

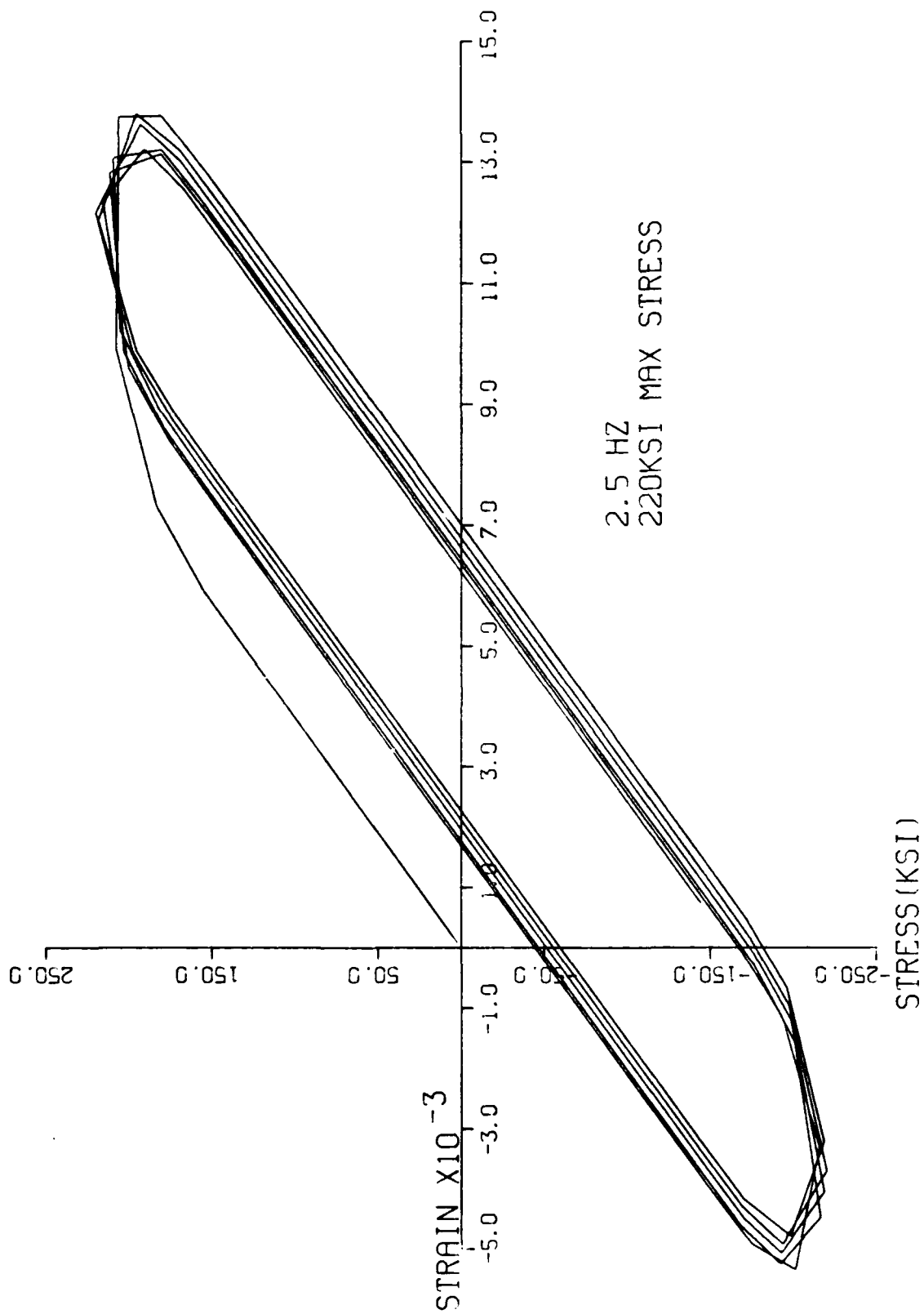


Fig 4.17 Stress/Strain Behavior Over Five Cycles

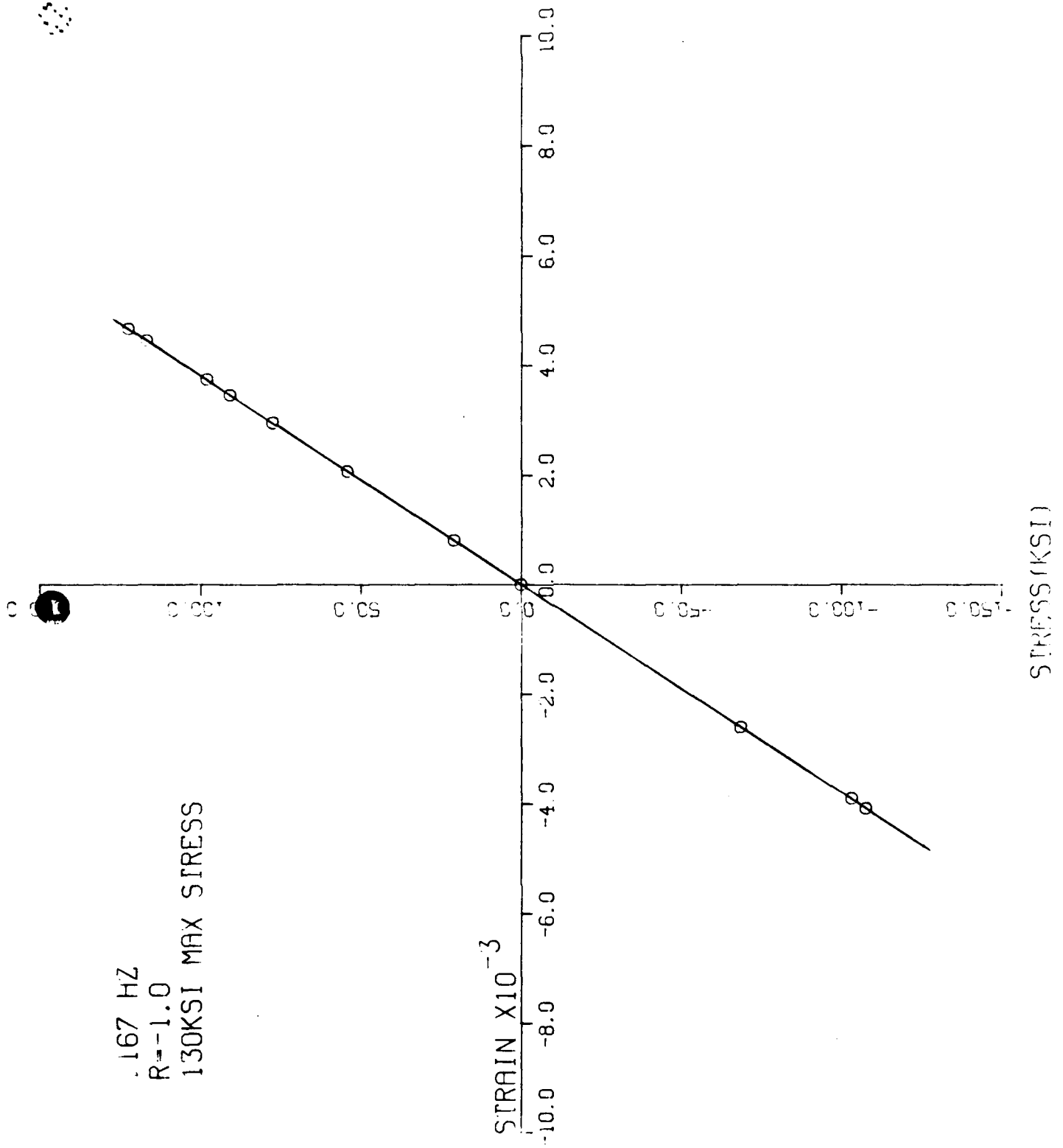


Fig 4.18 Stress/Strain Behavior Over Five Cycles

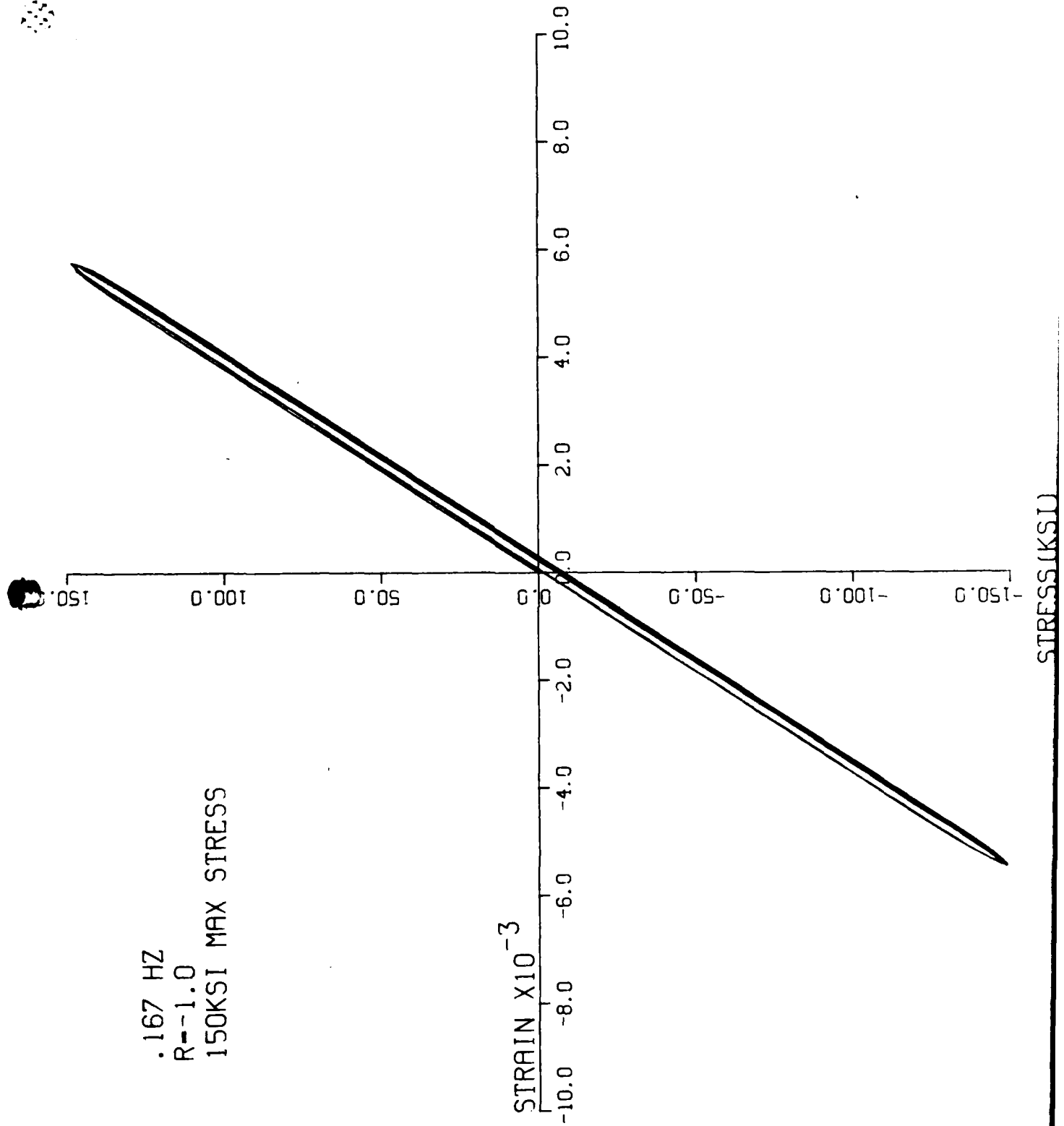


Fig 4.19 Stress/Strain Behavior Over Five Cycles

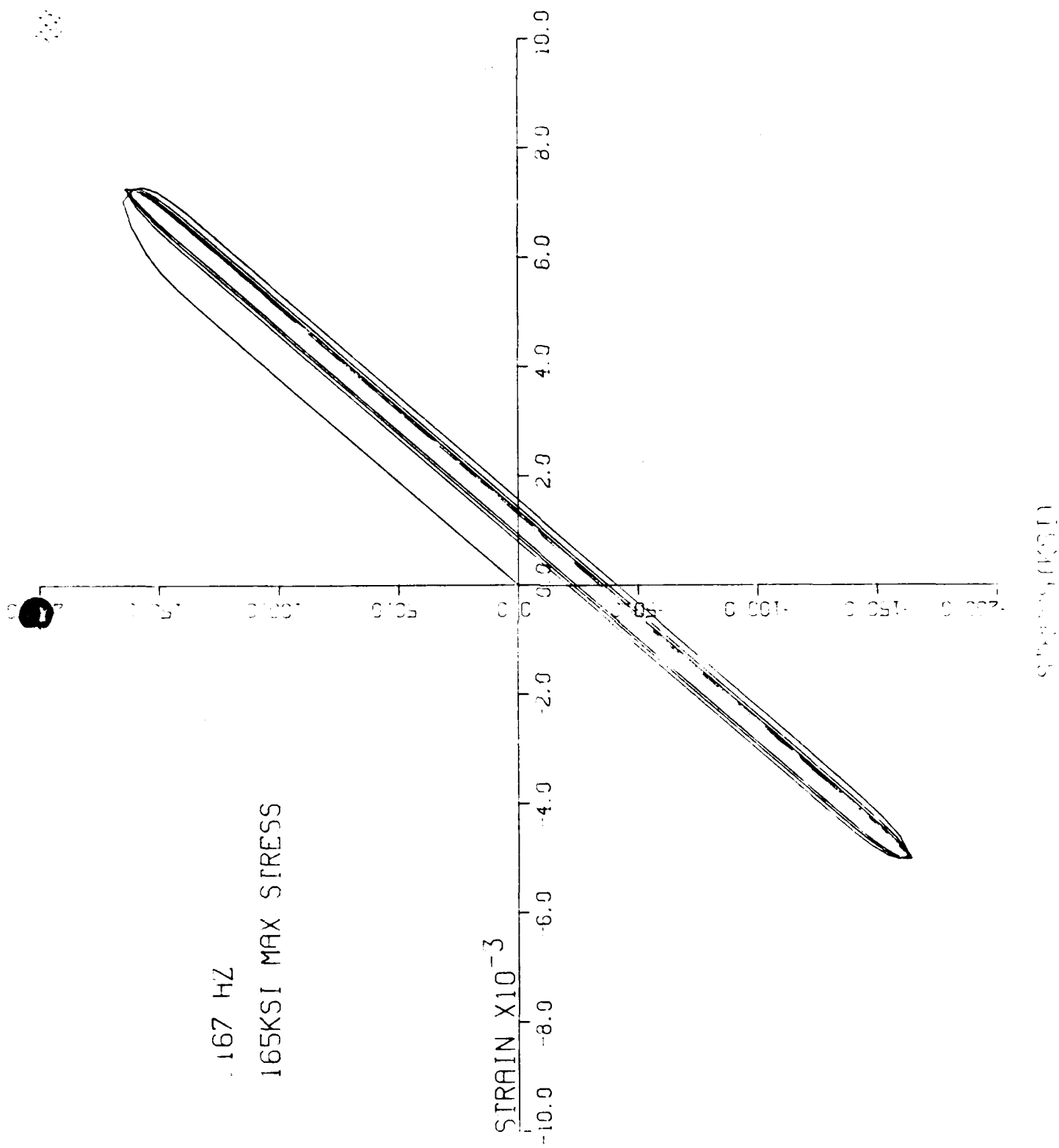


Fig 4.20 Stress/Strain Behavior Over Five Cycles

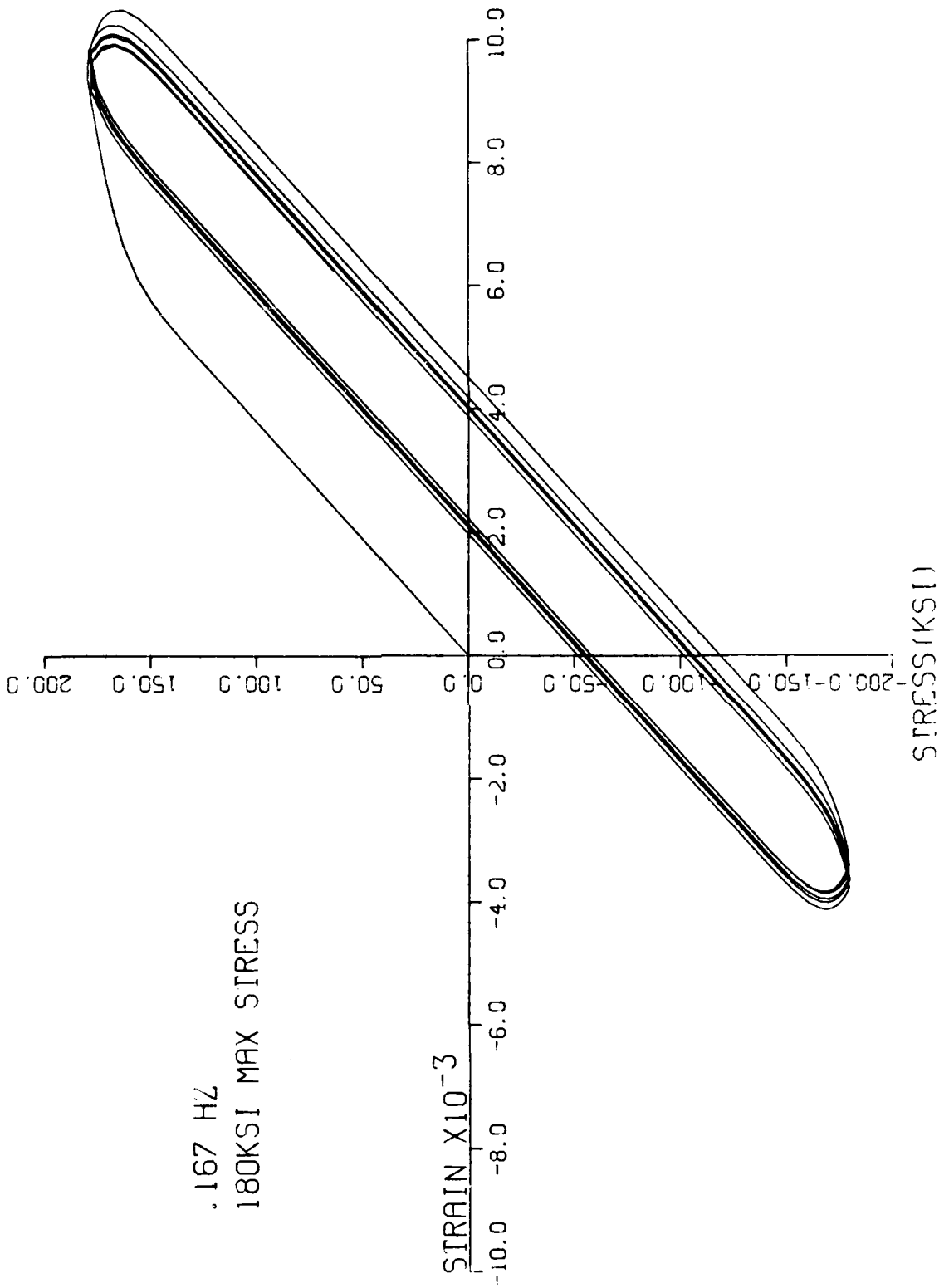


Fig 4.21 Stress/Strain Behavior Over Five Cycles

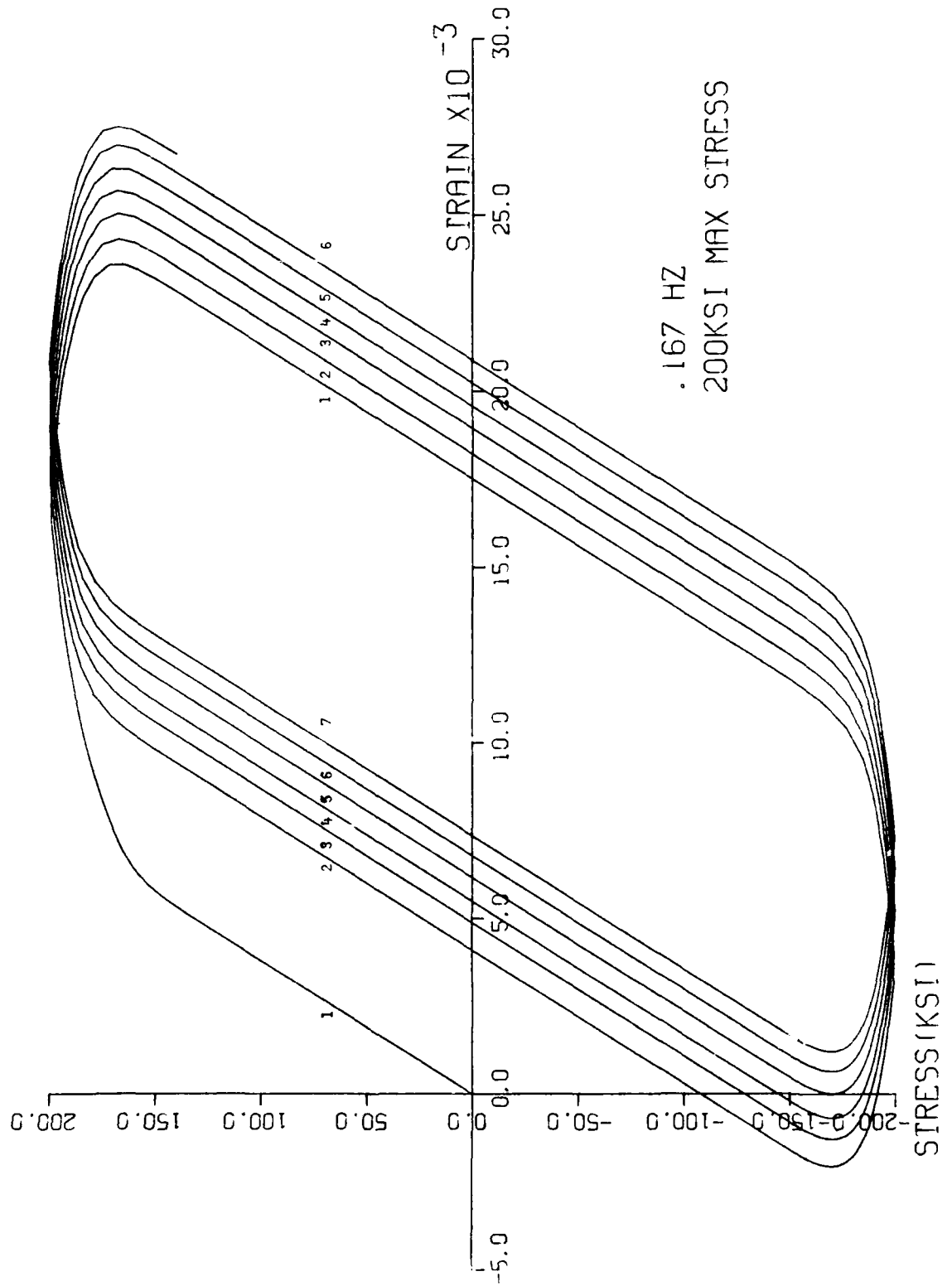


Fig 4.22 Stress/Strain Behavior Over Six Cycles

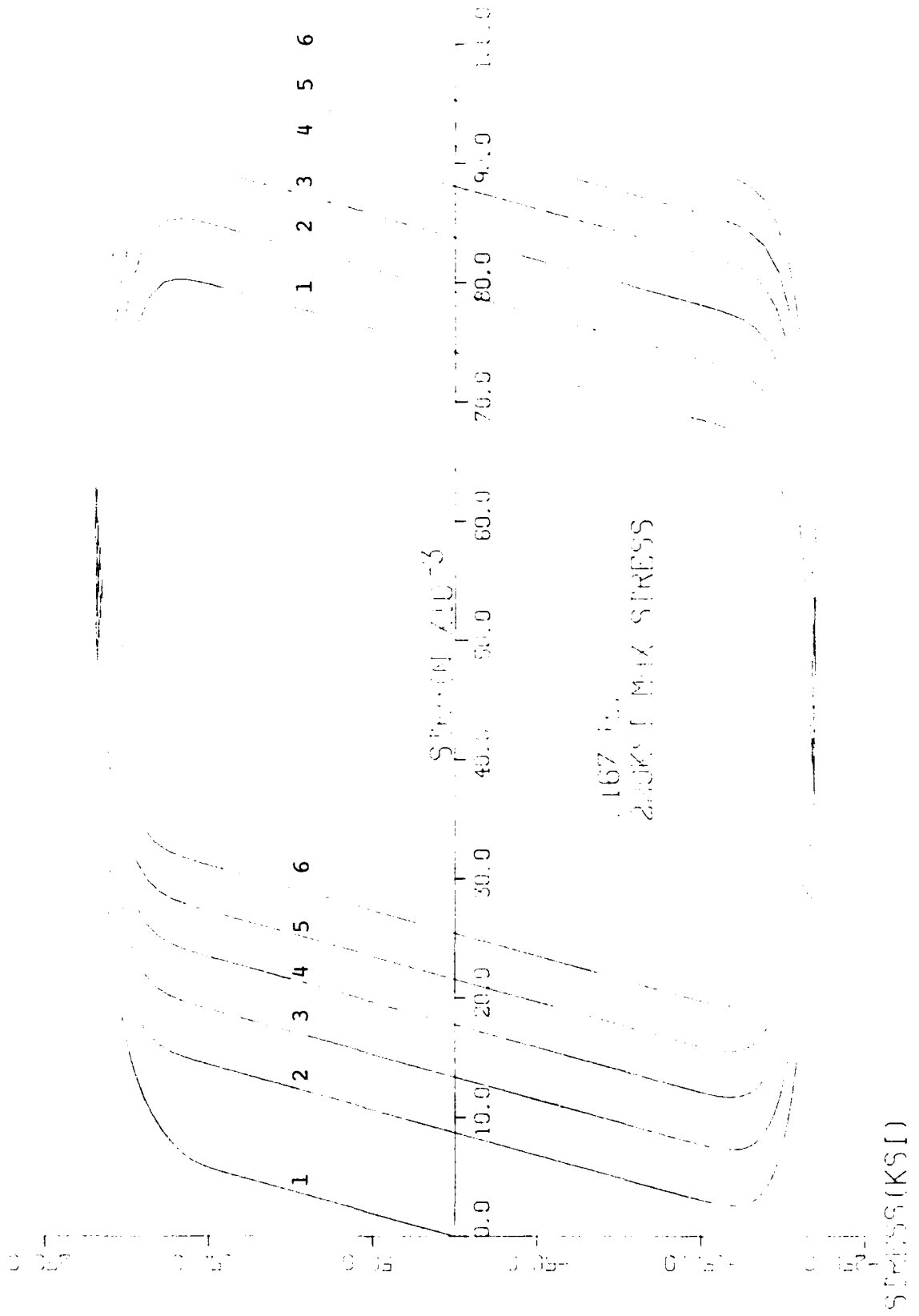


Fig 4.23 Stress/Strain Behavior Over Five Cycles

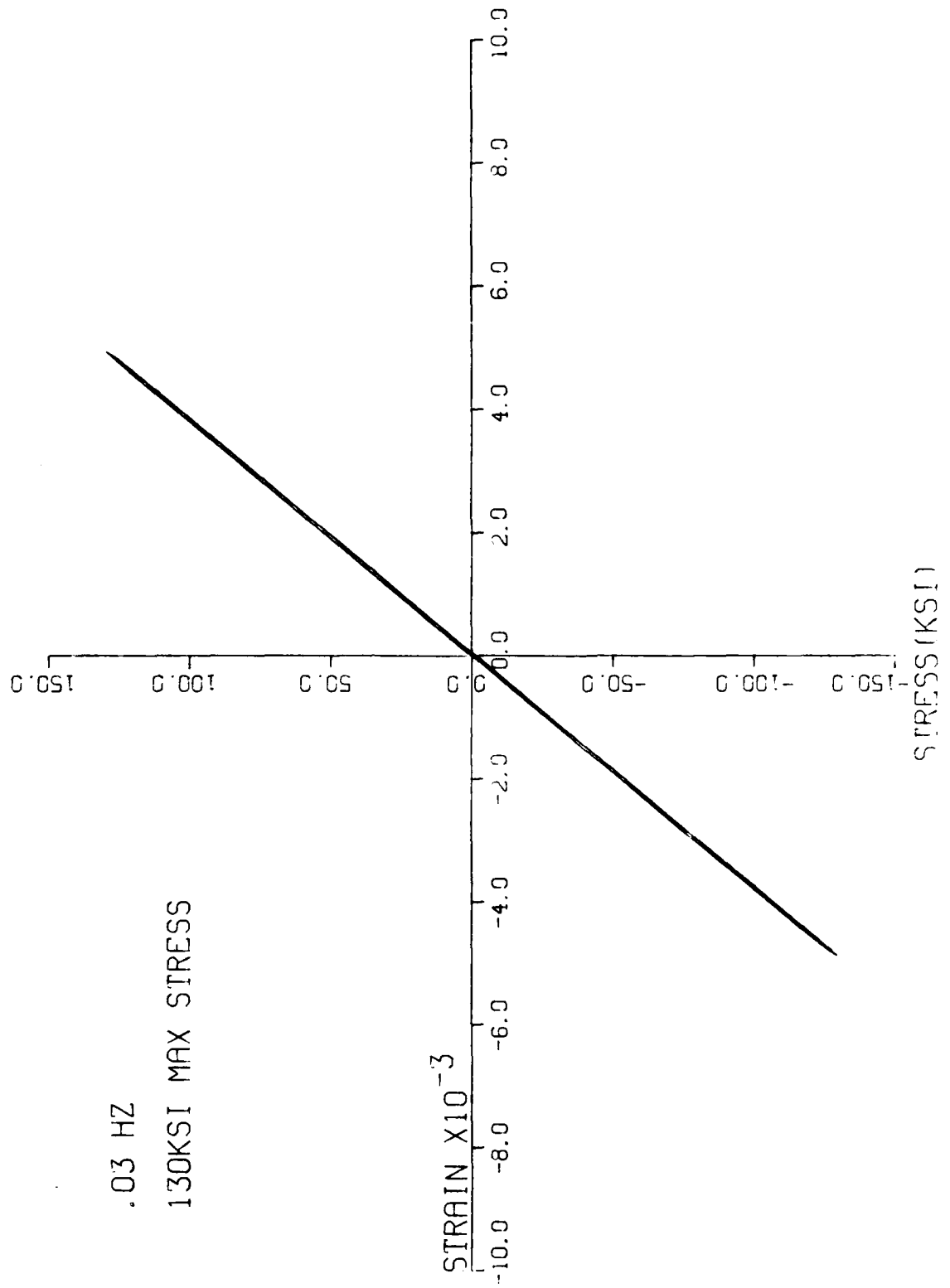


Fig 4.24 Stress/Strain Behavior Over Five Cycles

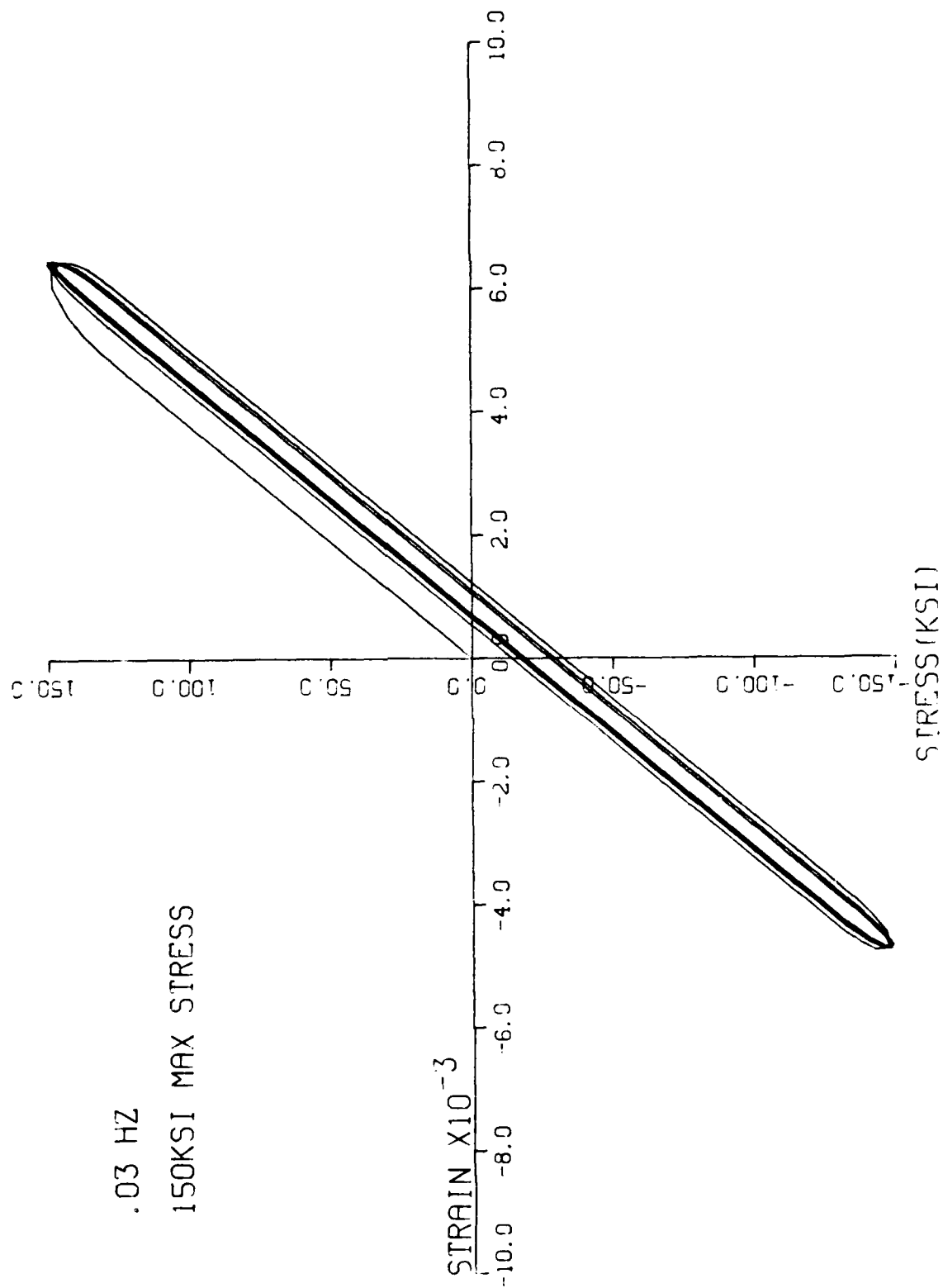


Fig 4.25 Stress/Strain Behavior Over Five Cycles

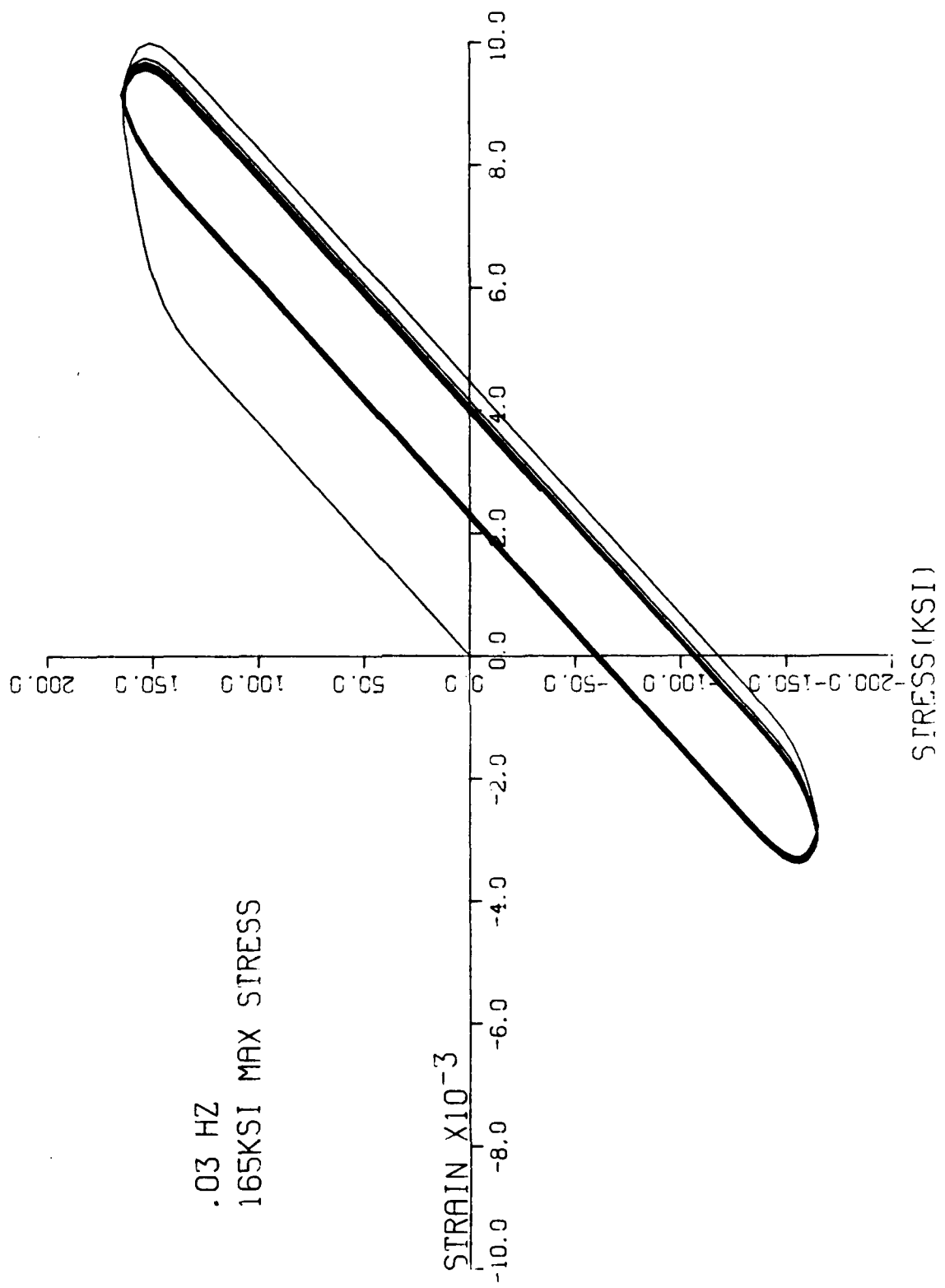


Fig 4.26 Stress/Strain Behavior Over Five Cycles

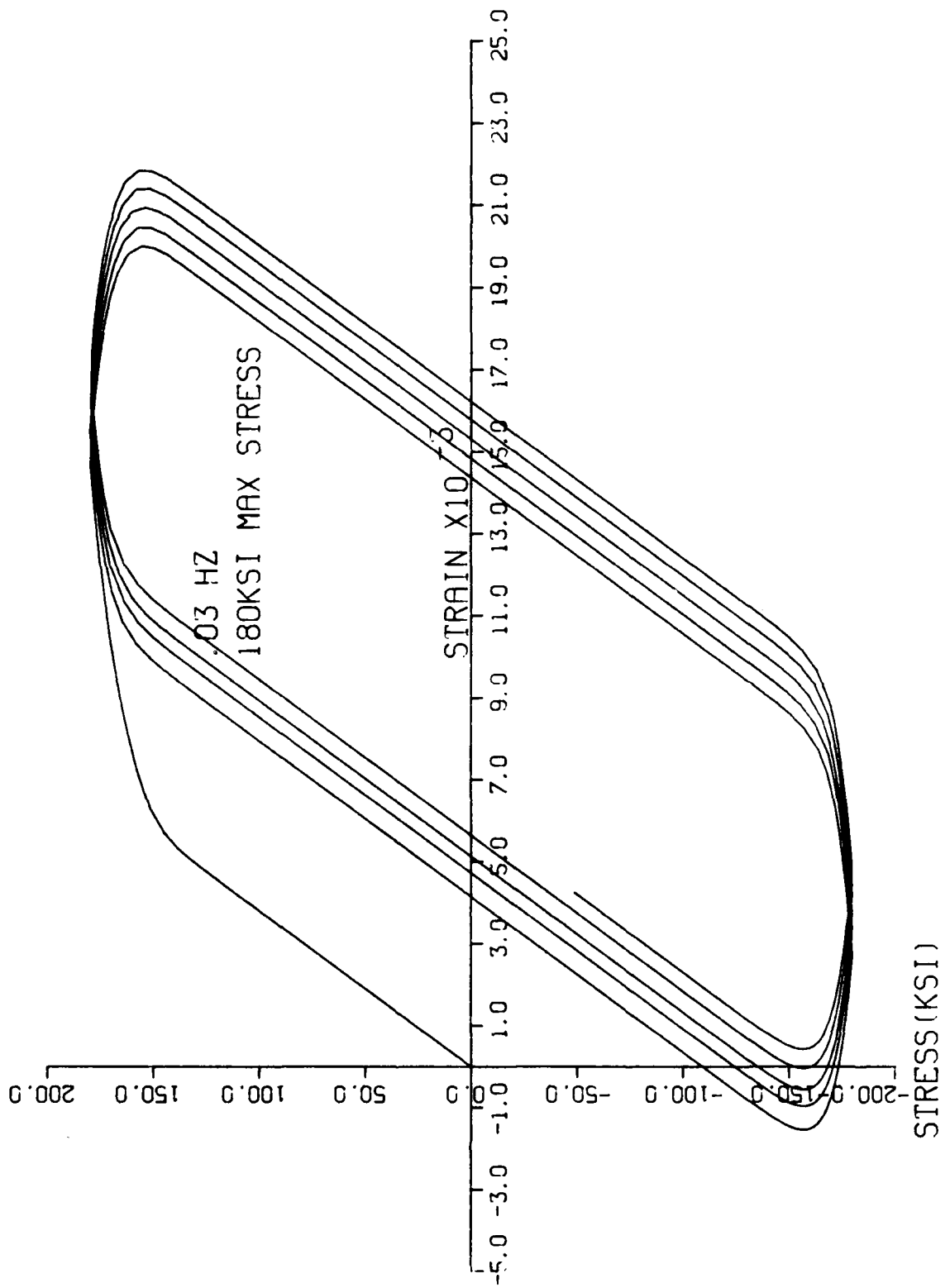


Fig 4.27 Stress/Strain Behavior Over Five Cycles

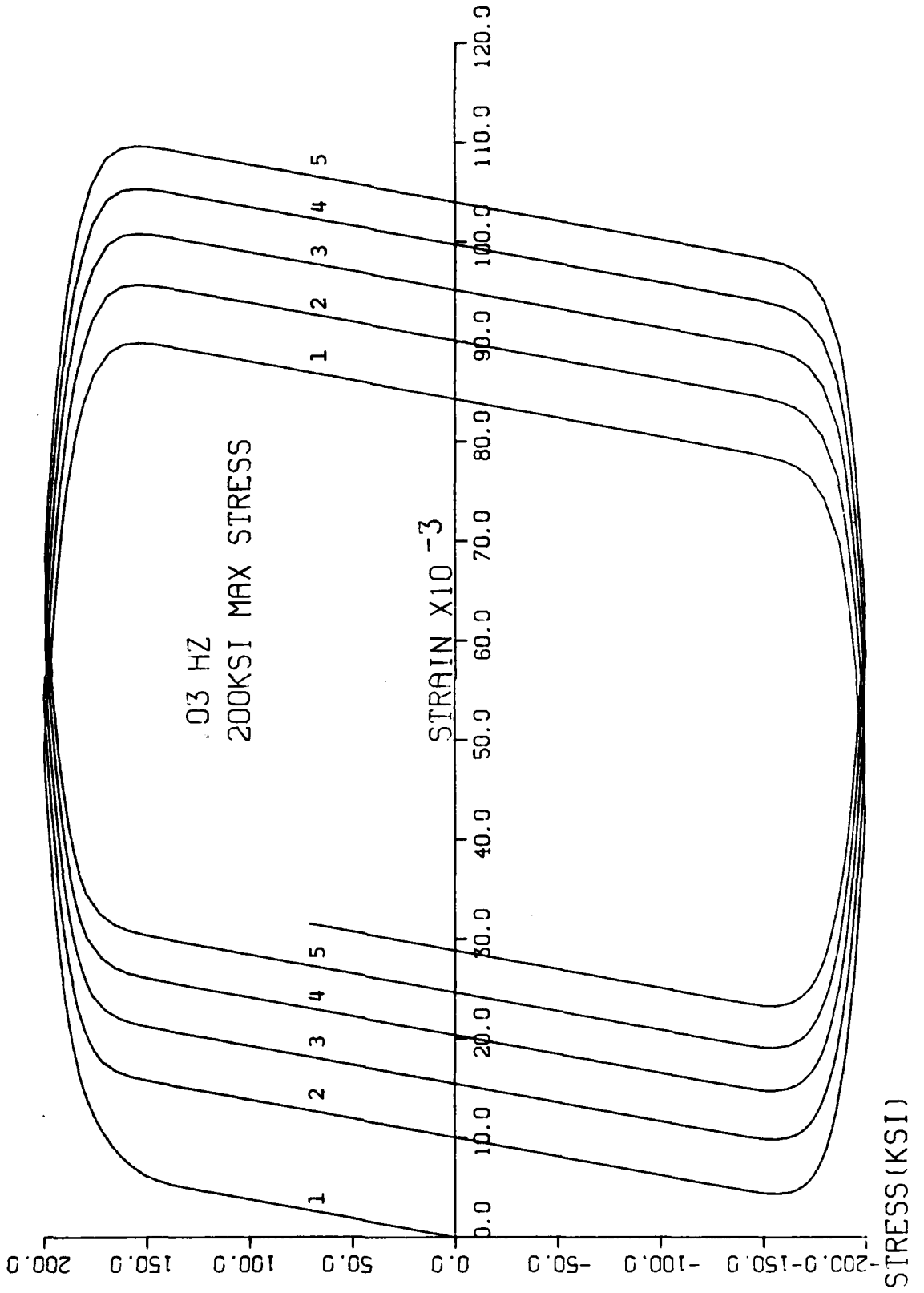


Fig 4.28 Stress/Strain Behavior Over Four Cycles

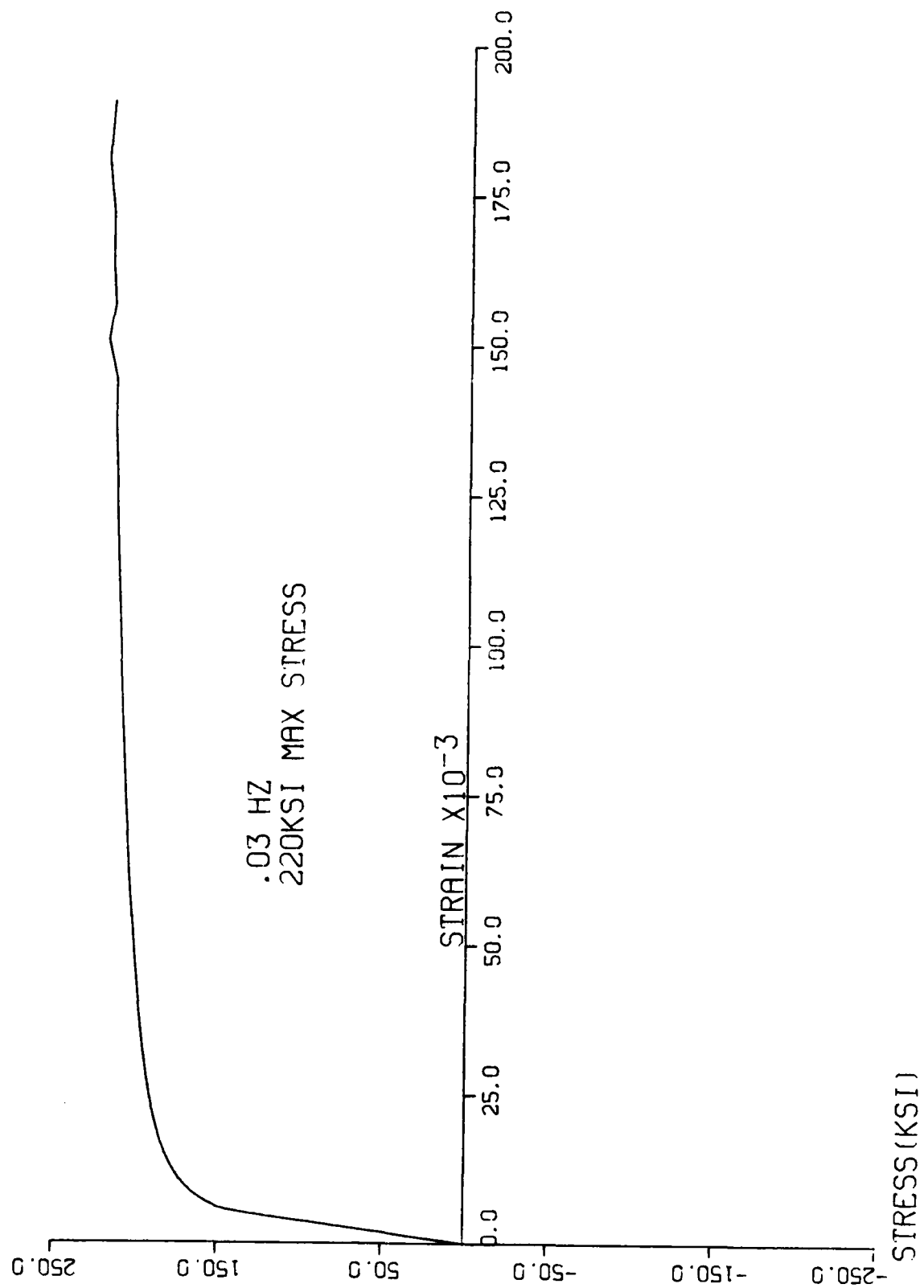


Fig 4.29 Uniaxial Stress/Strain Curve

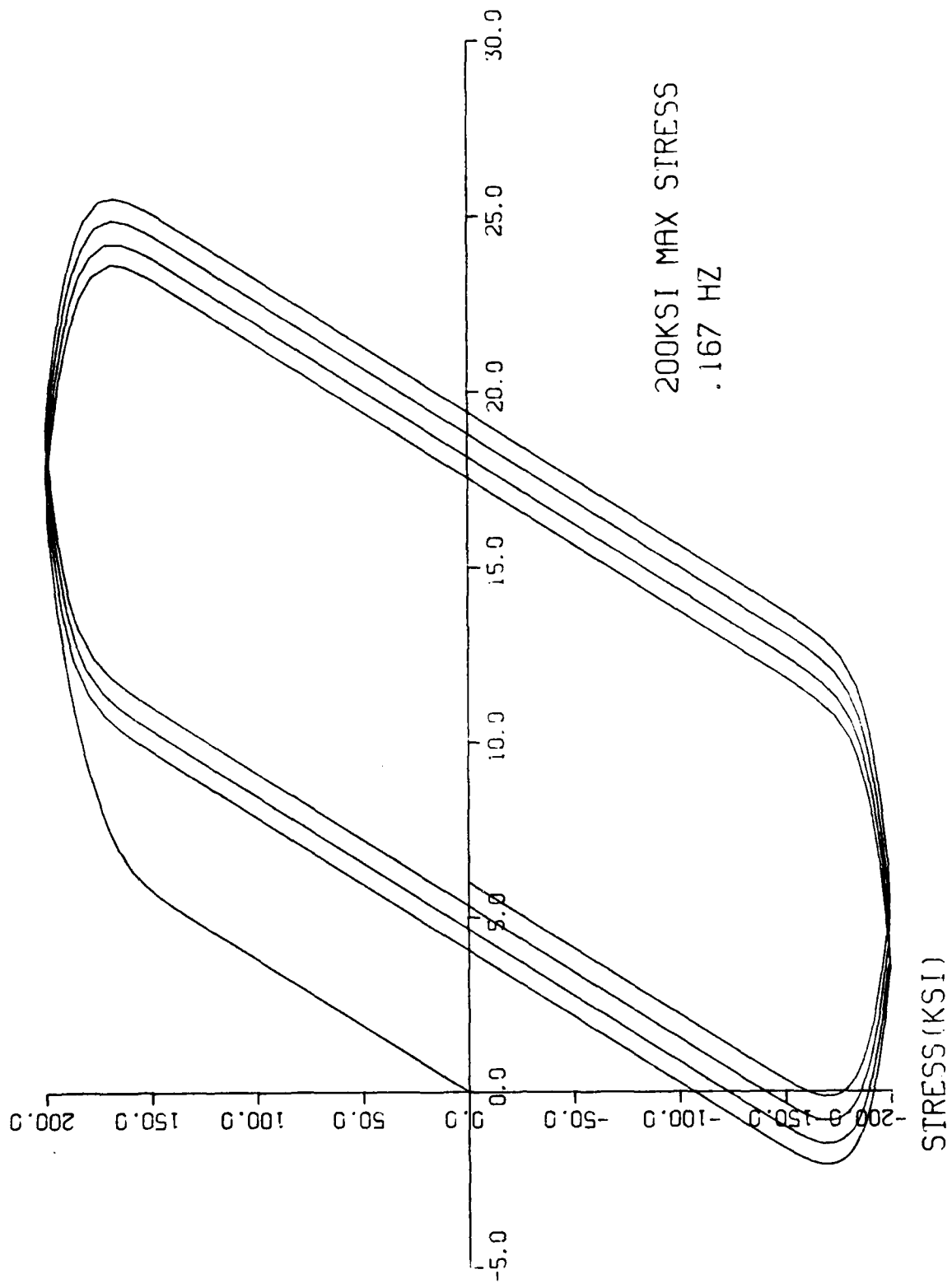


Fig 4.30 Uniaxial Stress/Strain Curve - 10 Elements

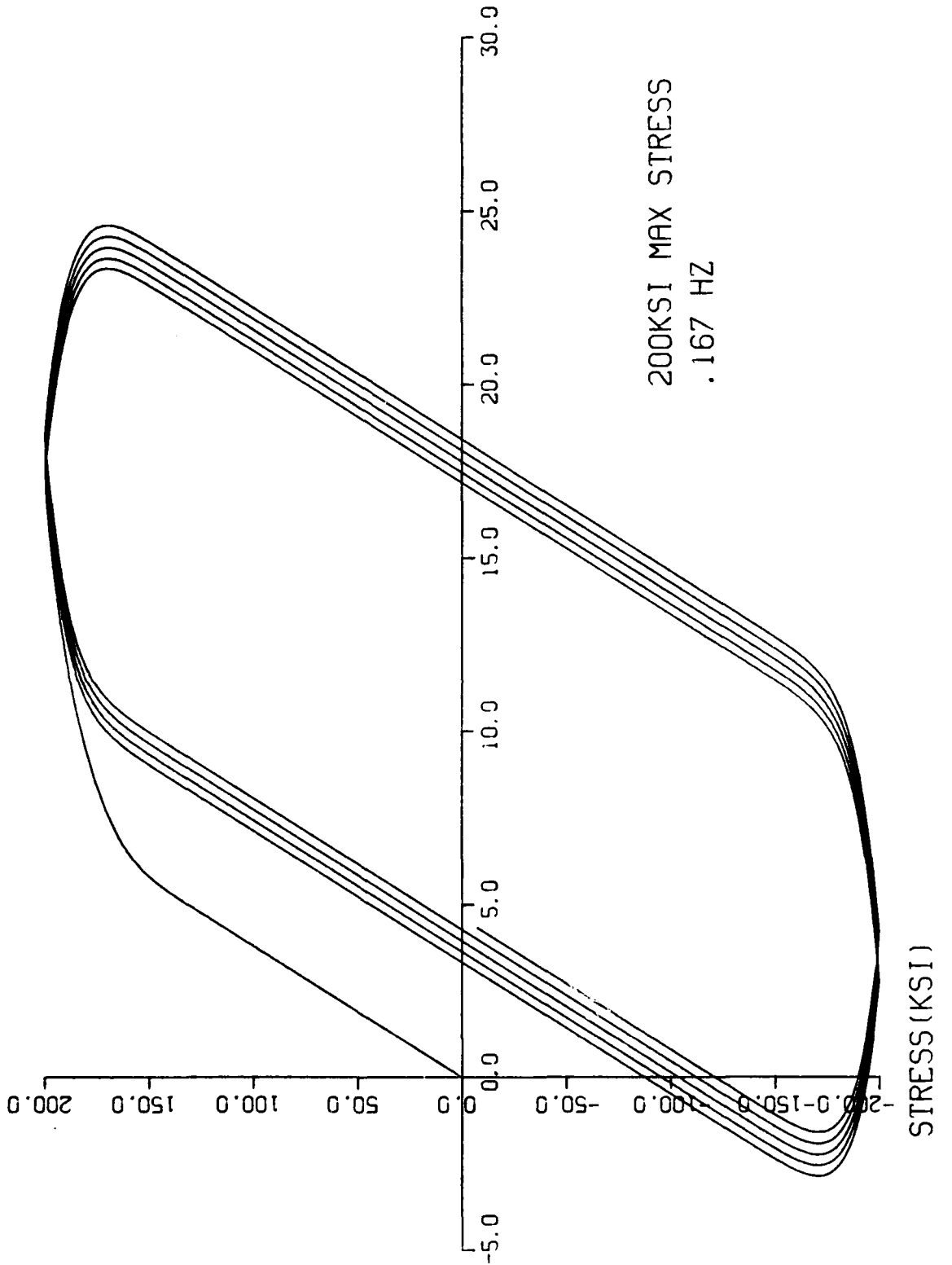


Fig 4.31 Stress/Strain Behavior with .02 Tolerance

for 180 and 220 KSI stress. There is a small amount of decrease in the value of  $Z$  during the elastic portion of the load cycle, but this is insignificant. The increase in  $Z$  is not instantaneous under any of the load conditions. This is seen as a slope in the step function in Figs 4.32-4.34, and is characteristic of the viscoplastic action.

#### Negative R-Ratio Compact Tension Specimen Results

Results and discussion in this section are derived from compact tension specimen load cycling at a frequency of 2.5 Hz, an R-ratio of -1.0 and maximum stress intensity values of 35 and 45 KSI $\sqrt{\text{in}}$ . The conclusions reached are broken down into three major areas:

- a) Crack opening displacements behind crack tip
- b) Profiles of the stress and strain fields ahead of the crack tip
- c) Plastic zone size estimations

The shape of the crack edge as the load goes from its full tensile value to its full compressive value during the second cycle is illustrated in Figs 4.35 and 4.36. The  $Y$  displacement as a function of distance behind the crack is identical to that of a positive R-ratio for the positive portion of the load cycle. As the load decreases through zero and becomes compressive, the crack begins to close. The elements furthest away from the crack tip close first, and as the load increases

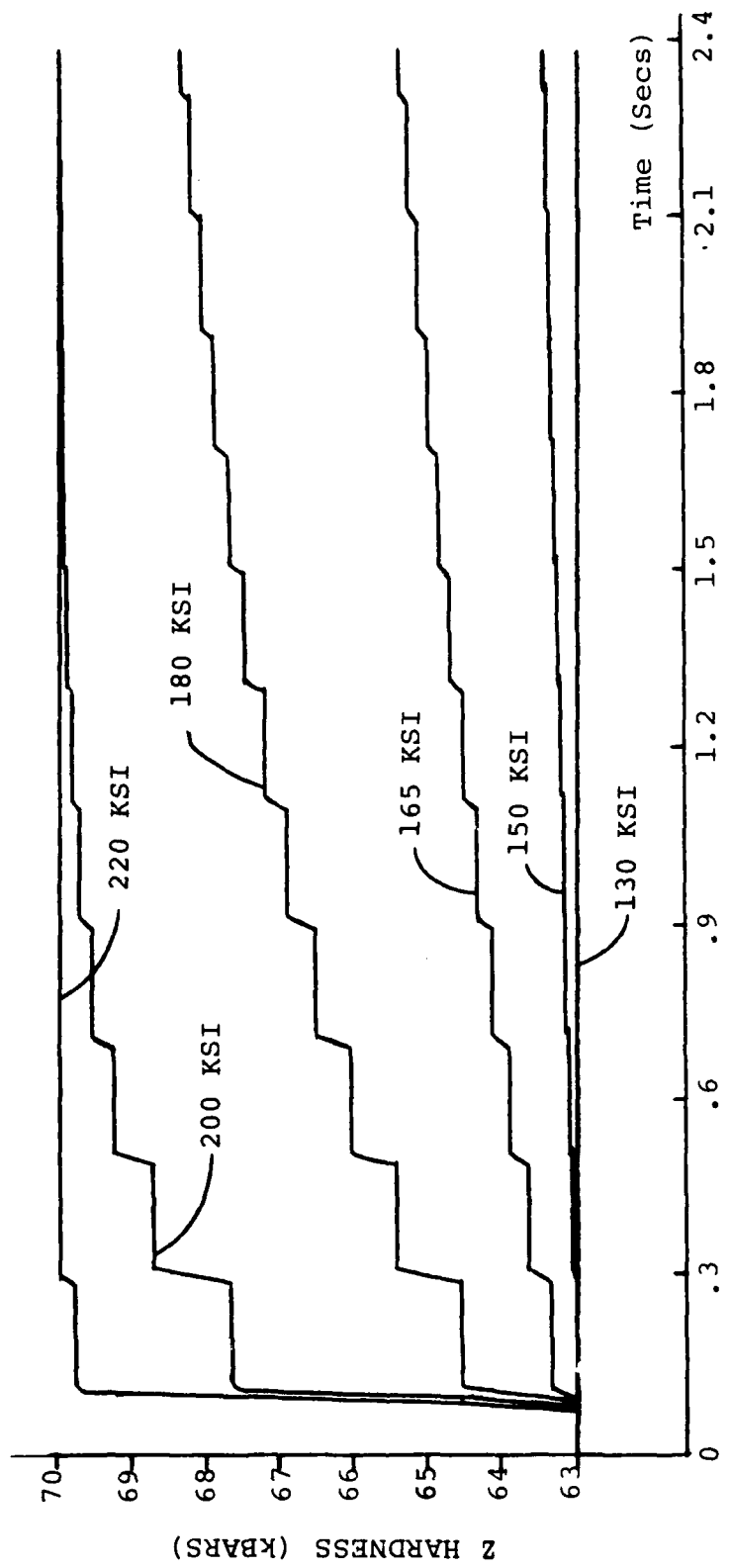


Fig 4.32 Z Hardness Over Six Cycles at 2.5 Hz

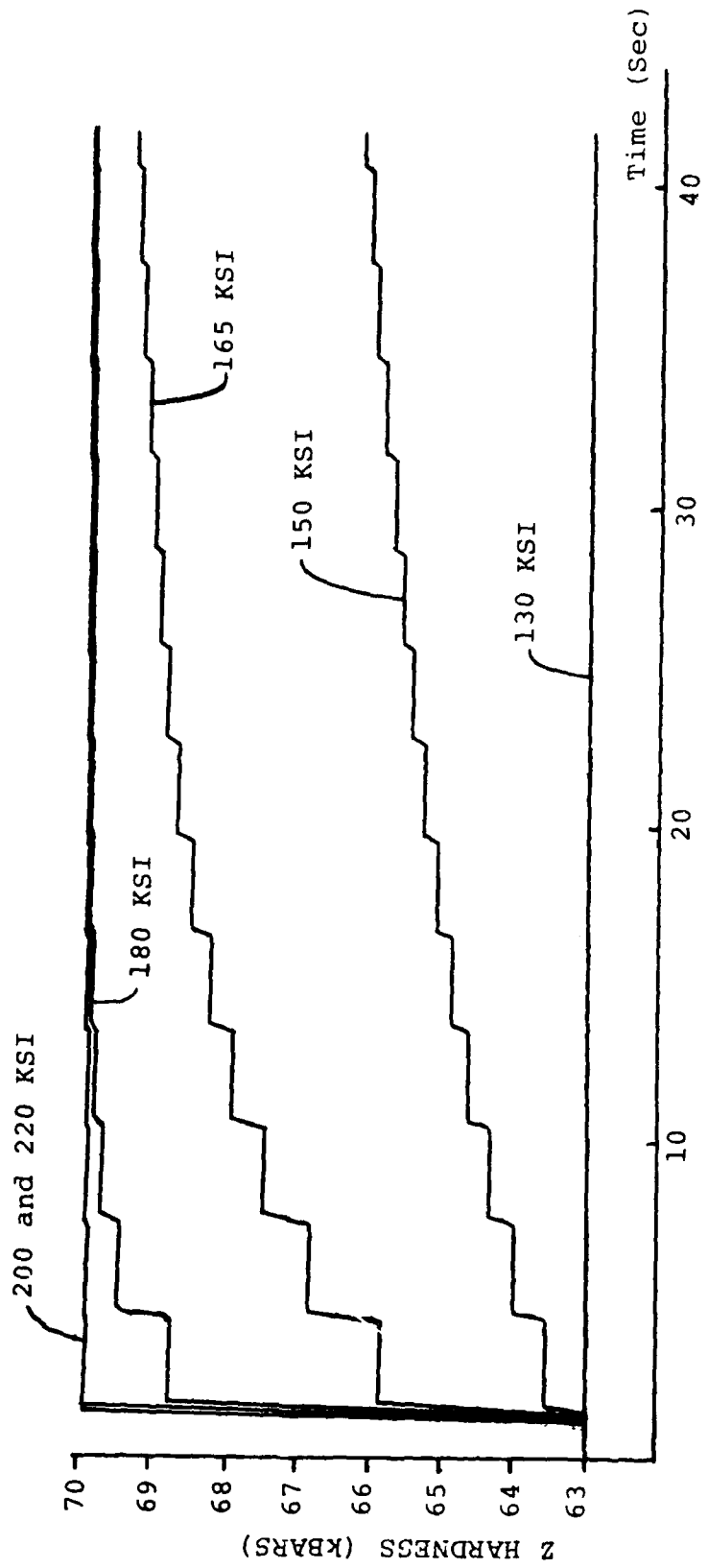


Fig 4.33 Z Hardness Over Six Cycles at 0.167 Hz

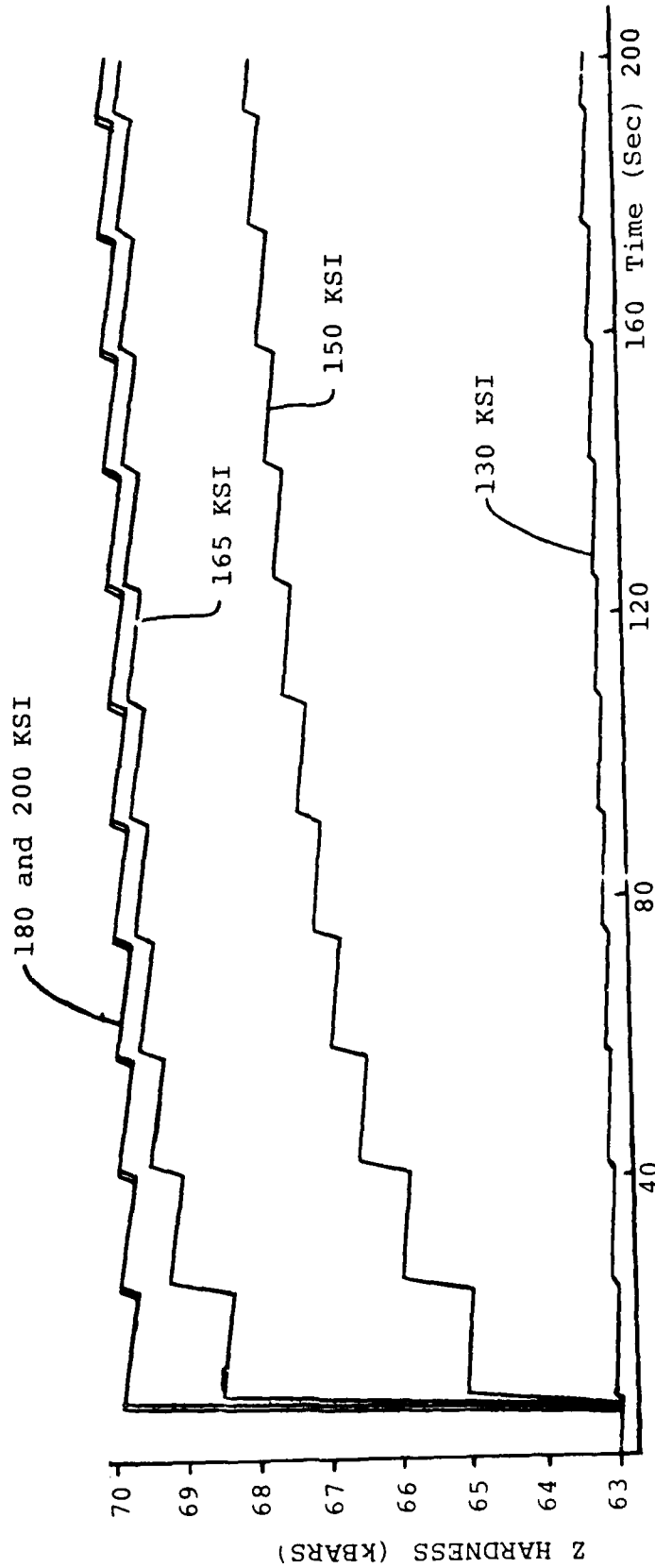


Fig 4.34 Z Hardness Over Six Cycles at 0.03 Hz

in compression, the crack closes closer to the crack tip. This sequence of crack closure is due to the residual plastic strain around the crack tip providing a fulcrum which resists the negative displacement. The edge of the crack can be thought of as a cantilever beam with a positive angular displacement from the x-axis. As a negative force is applied to the end of the beam, it will go to zero y-displacement. Near the fixed support, there will be some residual positive y-displacement. This residual y-displacement provides a radius of curvature at the crack tip so that it remains blunted, even under totally reversed loads.

The stress field ahead of the crack tip at the full tensile load value is shown in Figs 4.37 and 4.38. This profile is steady over several load cycles. This type of stress field has been discussed by several of the authors referenced in this thesis [12, 13, 14]. Notice that for  $K_1 = 45 \text{ KSI} \sqrt{\text{in}}$  (Fig 4.38), the stress field is significantly higher than for  $K_1 = 35 \text{ KSI} \sqrt{\text{in}}$ . A larger plastic zone is established as will be shown. When the load reaches its fully compressed value, the stress fields shown in Figs 4.39 and 4.40 are established. The stresses go from negative to positive and back to negative as the distance ahead of the crack tip increases. This profile is due to the residual positive plastic strains which exist even at the fully reversed load level. Note that the magnitude of the stresses are much smaller than the corresponding stresses under a tensile load. Note also that the reversed load for  $K_1 = 35 \text{ KSI} \sqrt{\text{in}}$  produces a

compressive stress less than that for a  $K_1 = 45 \text{KSI} \sqrt{\text{in}}$  near the crack tip, yet just the opposite is occurring away from the tip.

The strain field ahead of the crack tip under a tensile load increases in magnitude during the load cycling (see Figs 4.41 and 4.42). It is obvious that the larger  $K_1$  value produces a strain function of greater magnitude. A fairly constant rate of strain increase per cycle is evident for both  $K_1$  values. This indicates that the stable strain solution for reversed loading may be at a larger number of cycles than for positive R-ratio load spectra. When the load is at its full negative value the strain immediately ahead of the crack tip is initially negative for  $K_1 = 35 \text{KSI} \sqrt{\text{in}}$ , but becomes positive within four cycles (see Fig 4.43). The strain component for  $K_1 = 45 \text{KSI} \sqrt{\text{in}}$  is always positive immediately ahead of the crack tip. These residual positive strains are due to the large plastic overload which occurs during the first load cycle. The stress profile ahead of the crack tip under compressive loading is governed by these residual strains interfacing with the negative input loads.

The effect of load magnitude on the size of the plastic zone is examined in Figs 4.45 and 4.46. These two figures illustrate the approximate shape and size of the plastic zone when the load is at its maximum tensile value. An element is assumed to have undergone plastic strain if the  $\epsilon_y$  magnitude is greater than  $1 \times 10^{-3}$  in/in. The size of the plastic zone is very stable over load cycling. The slight increases in strain shown in Fig 4.41 and 4.42 are not large enough to drive any of the elements adjacent to the plastic zone into plasticity

over the number of load cycles examined. When the load is reversed, the plastic zone is compressed into an elliptically shaped region (see Figs 4.47 and 4.48). The area of this region is approximately one-twelfth of the area of the plastic zone under a tensile load. This region of significant positive  $\gamma$  strain which exists under the compressive load is due to the large plastic overload which occurs during the first load cycle. The type of material behavior which occurs under this condition could be expected to follow the same pattern as that which is seen when a specimen under positive loading undergoes an application of an overload. The material surrounding the plastic zone applies a compressive force which decreases its size. The resulting residual compressive stresses ahead of the crack tip will aid in retarding crack growth.

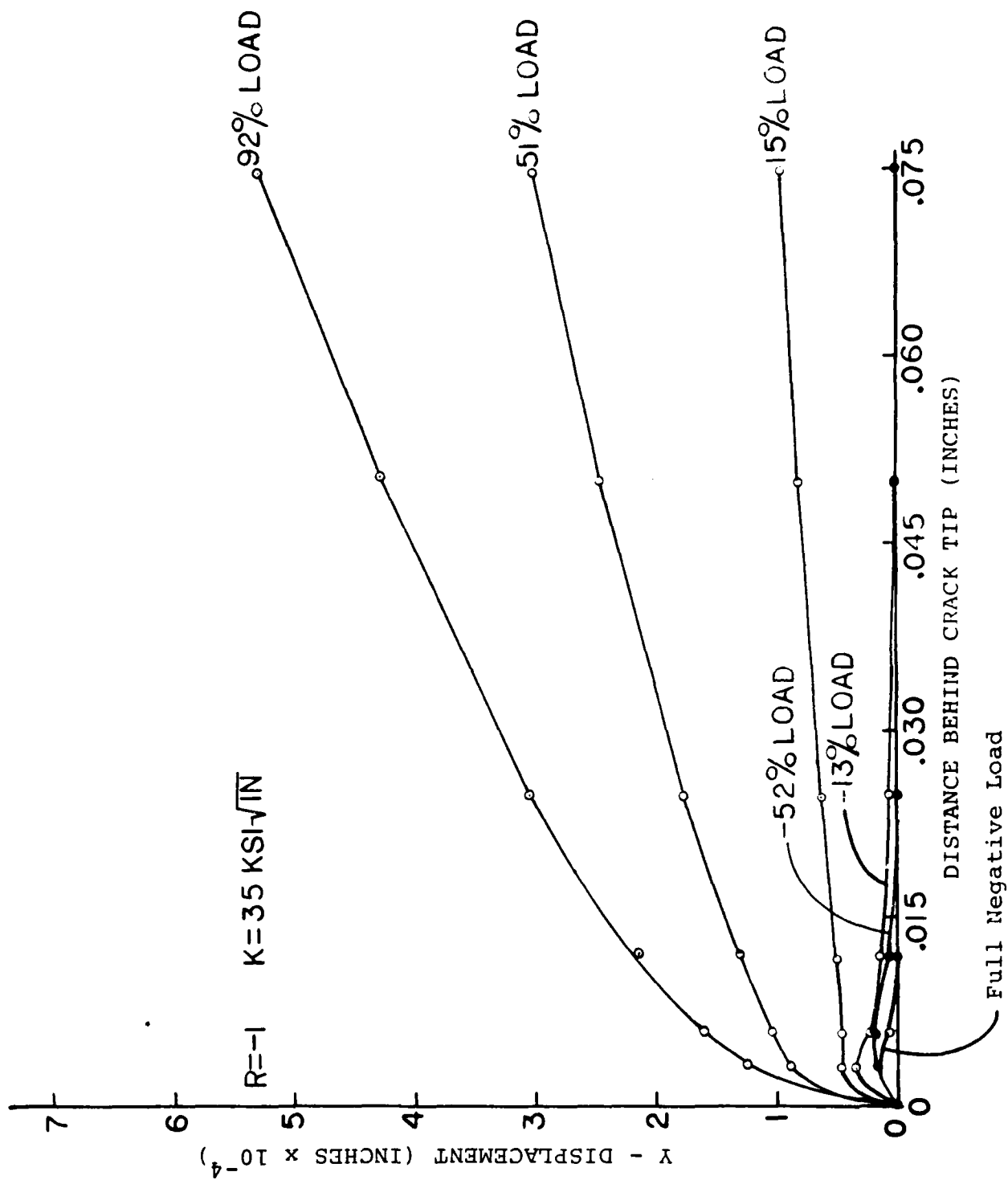


Fig 4.35 Y Displacement vs Distance Behind Crack Tip

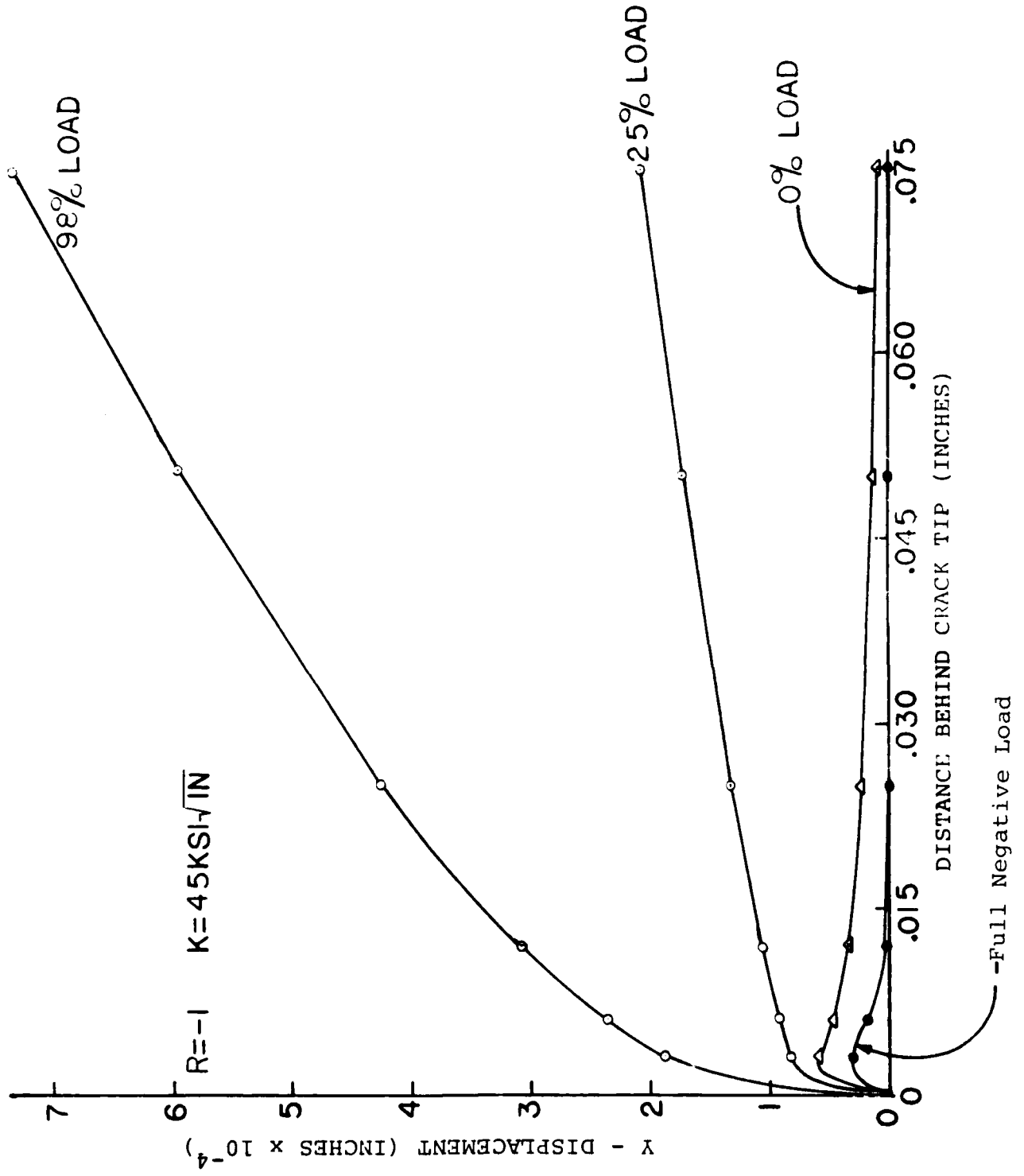


Fig 4.36 Y Displacement vs Distance Behind Crack Tip

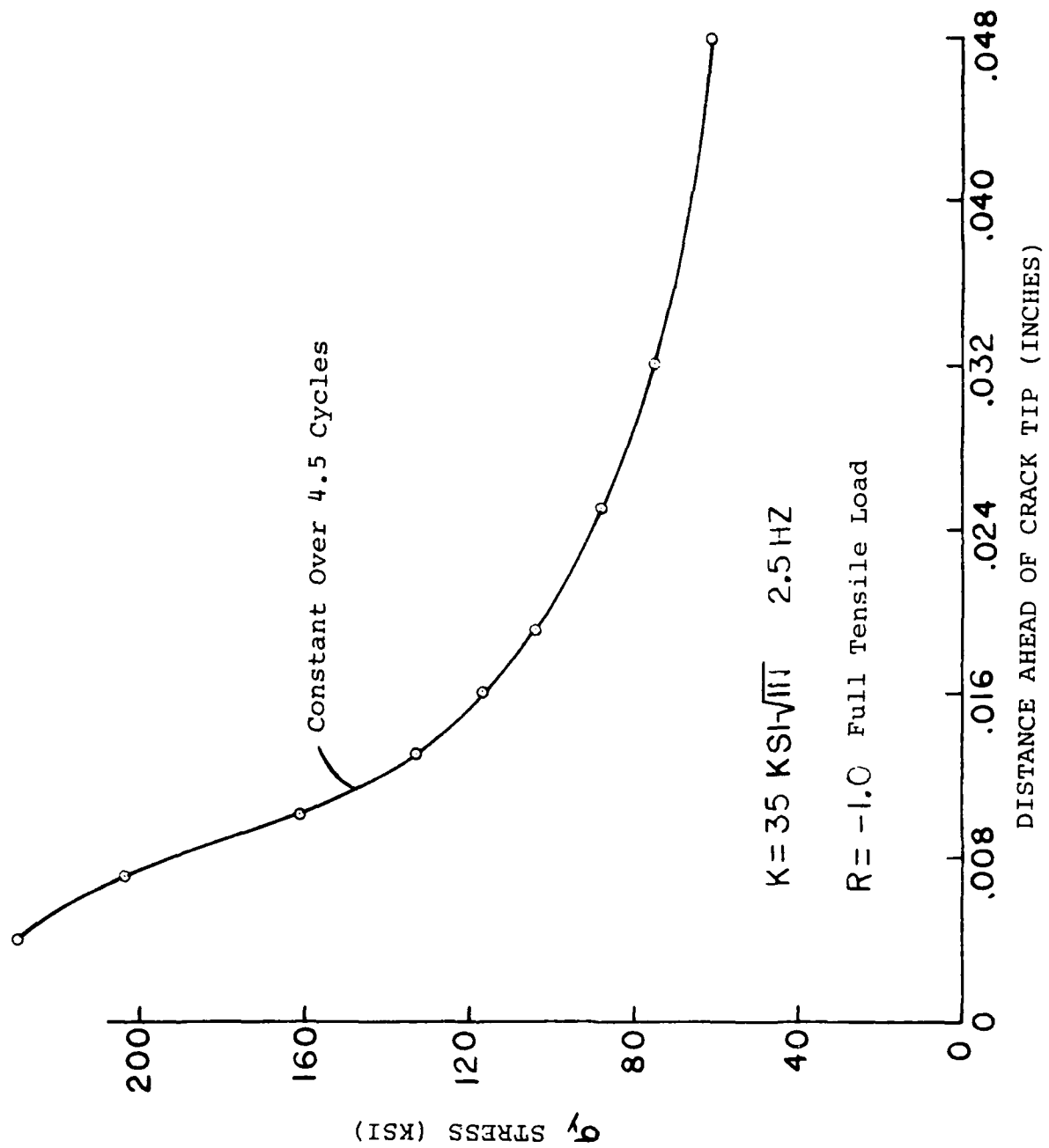


Fig 4.37 Y Stress Field After 2.25 Cycles

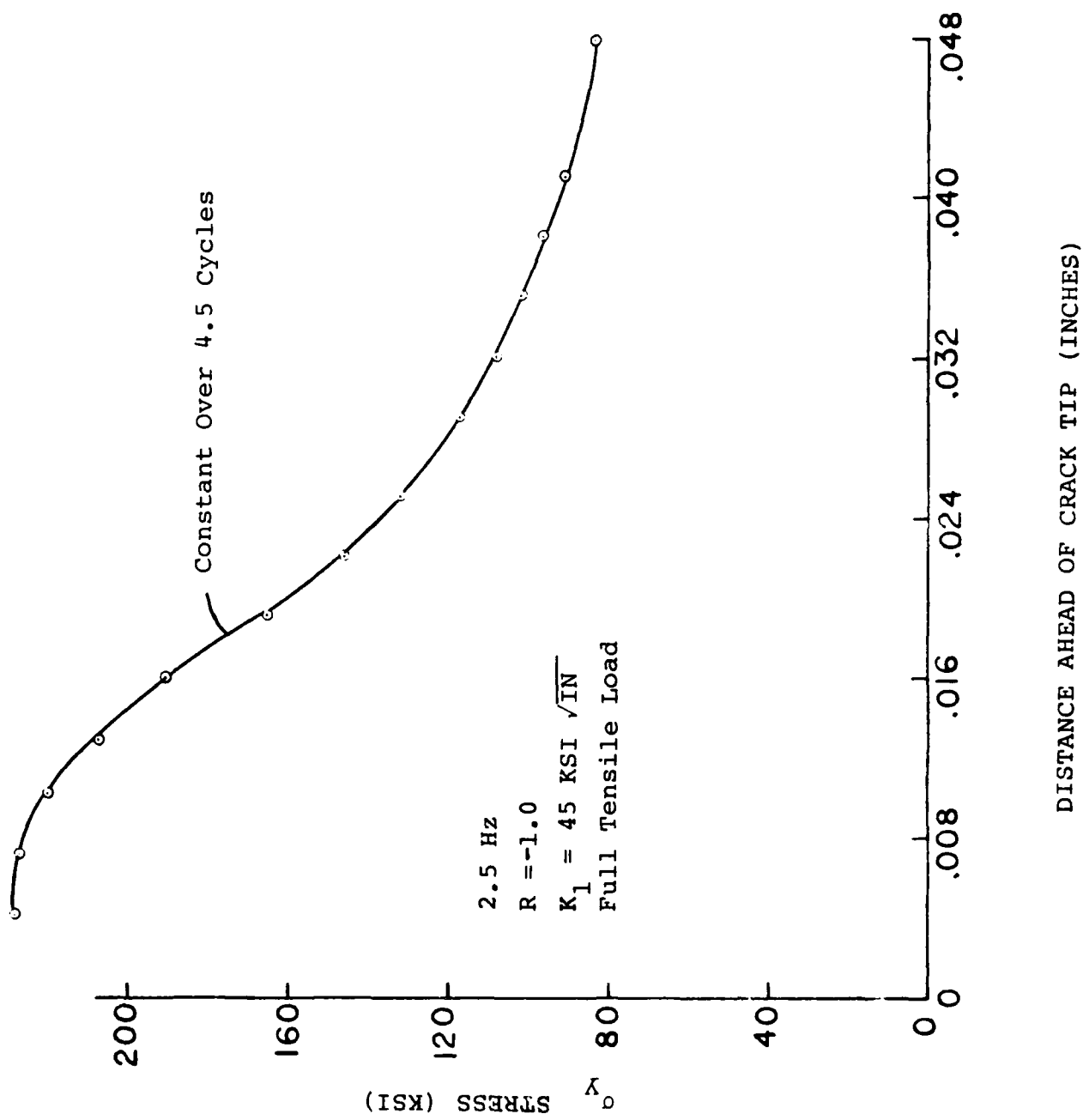


Fig 4.38 Y Stress Field Ahead of Crack Tip

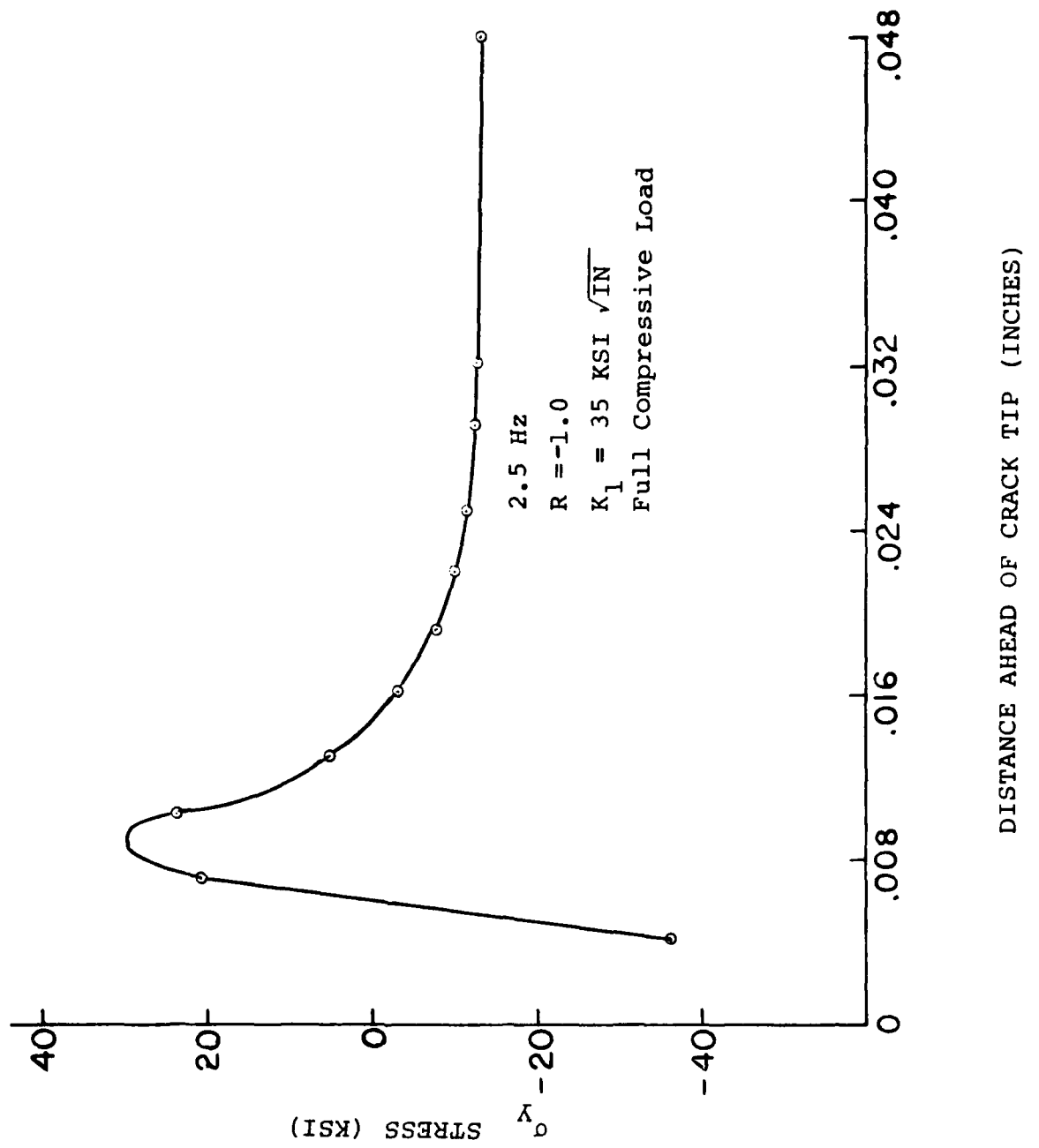


Fig 4.39 Y Stress Field Ahead of Crack Tip

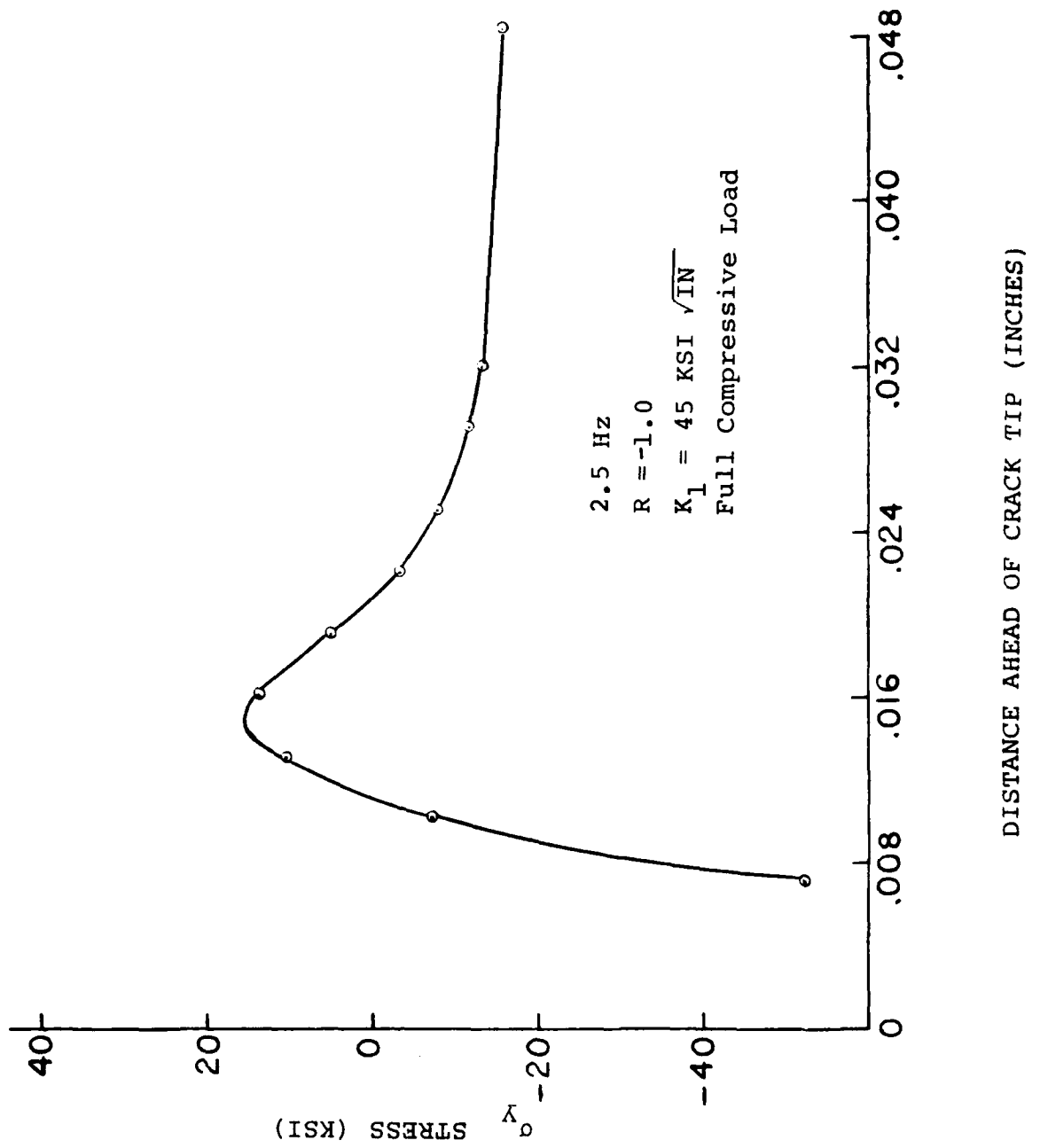


Fig 4.40 Y Stress Field Ahead of Crack Tip

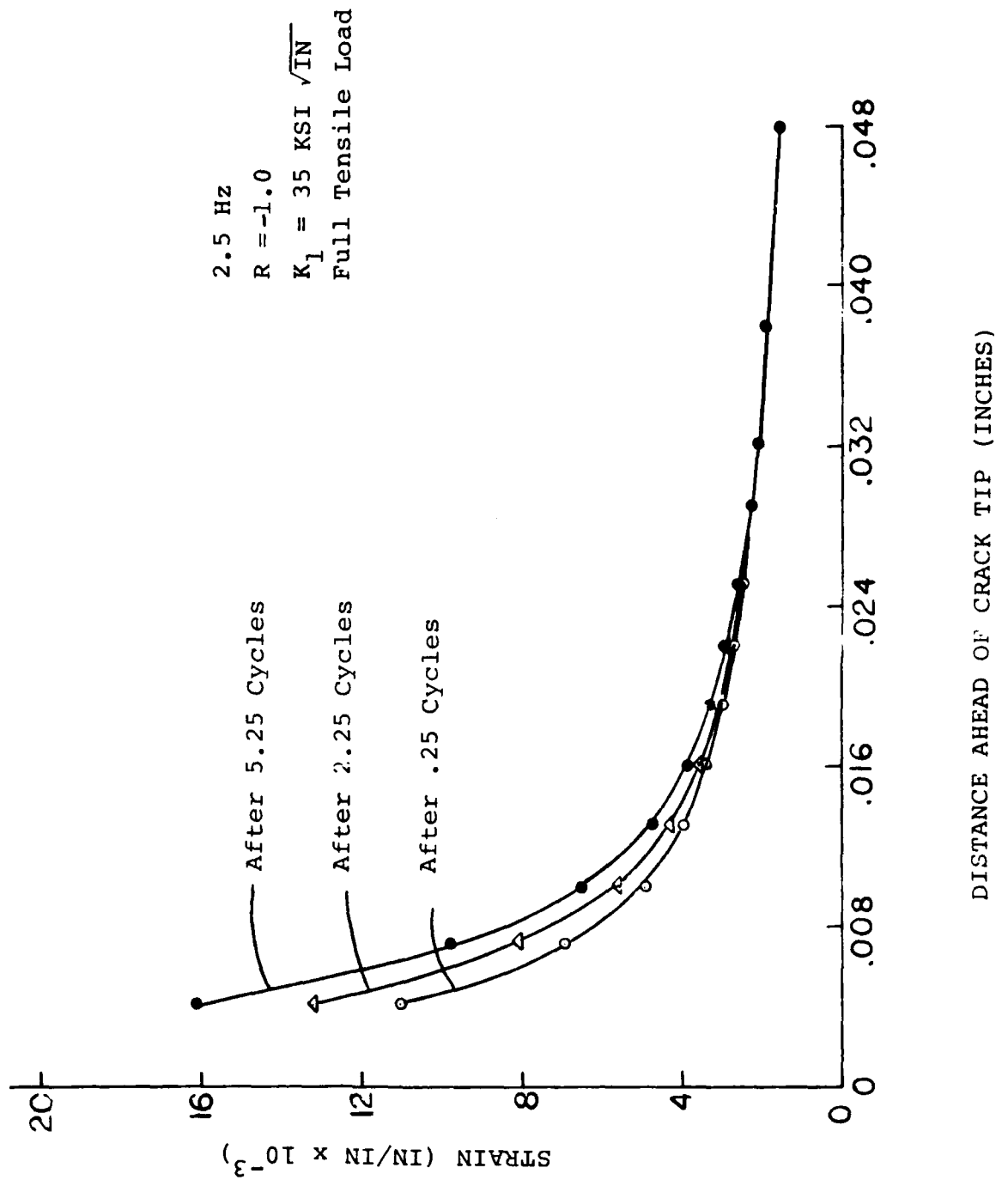


Fig 4.41 Y Strain Field Ahead of Crack Tip

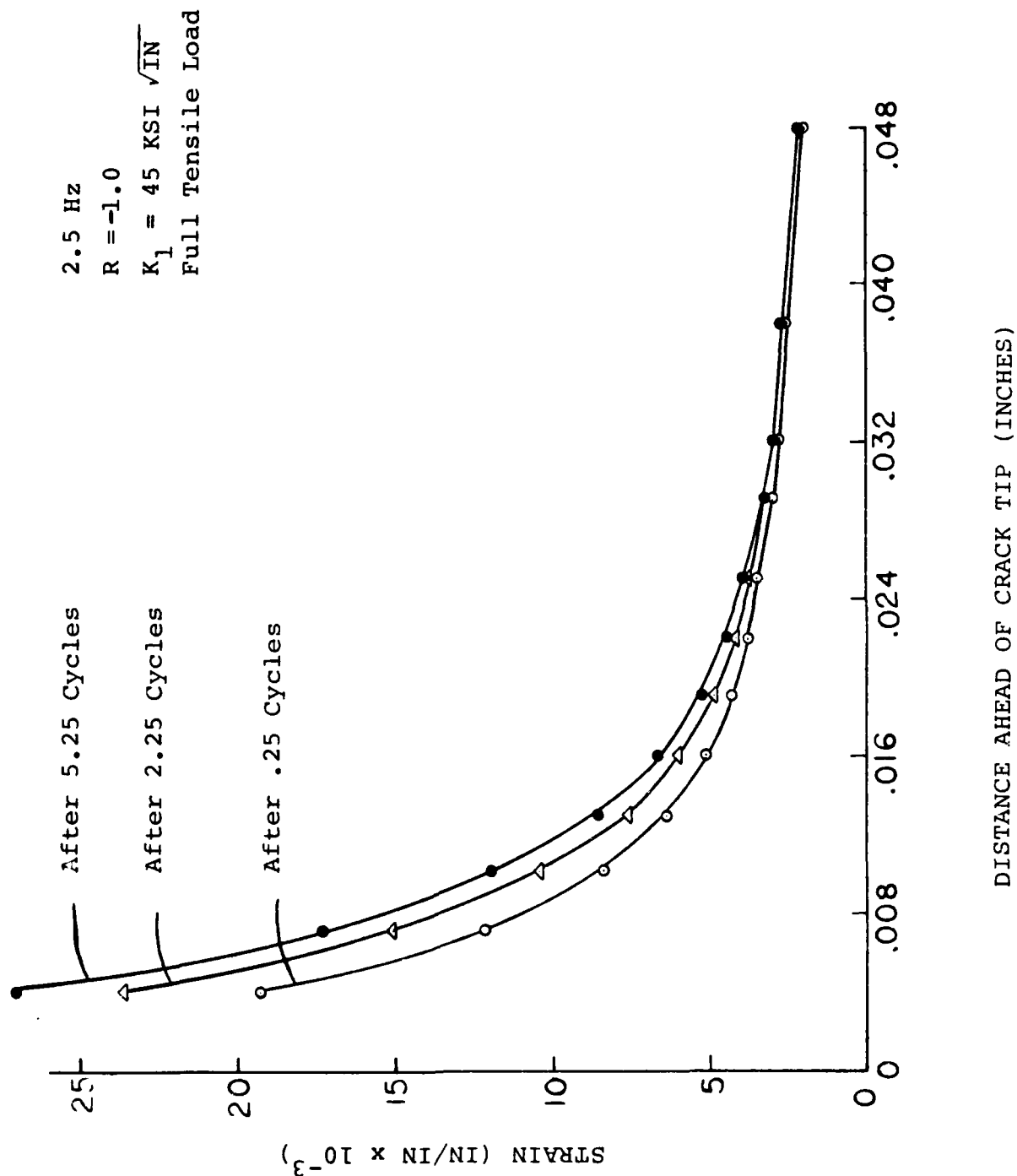


Fig 4.42 Y Strain Field Ahead of Crack Tip

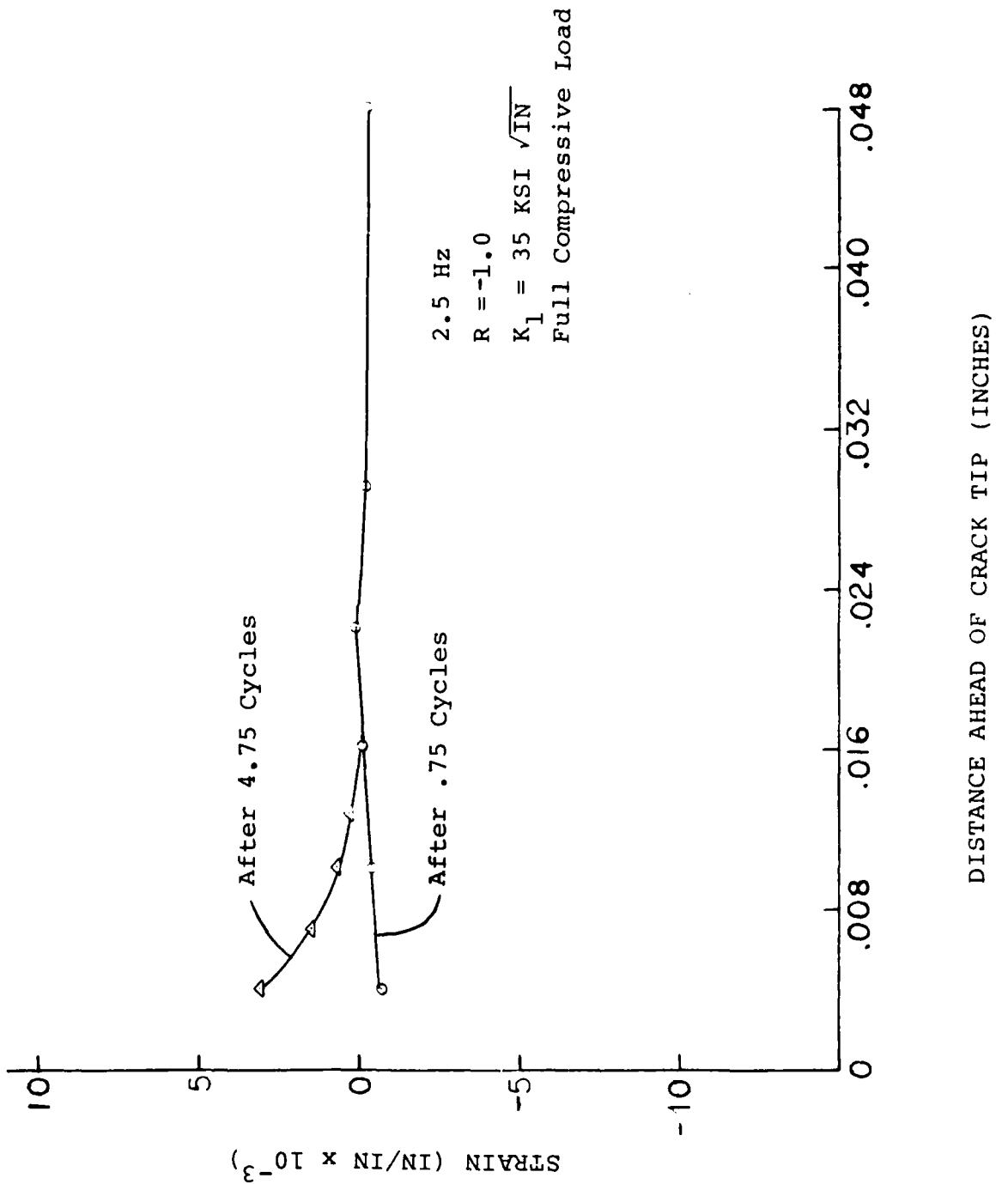


Fig 4.43 Y Strain Field Ahead of Crack Tip

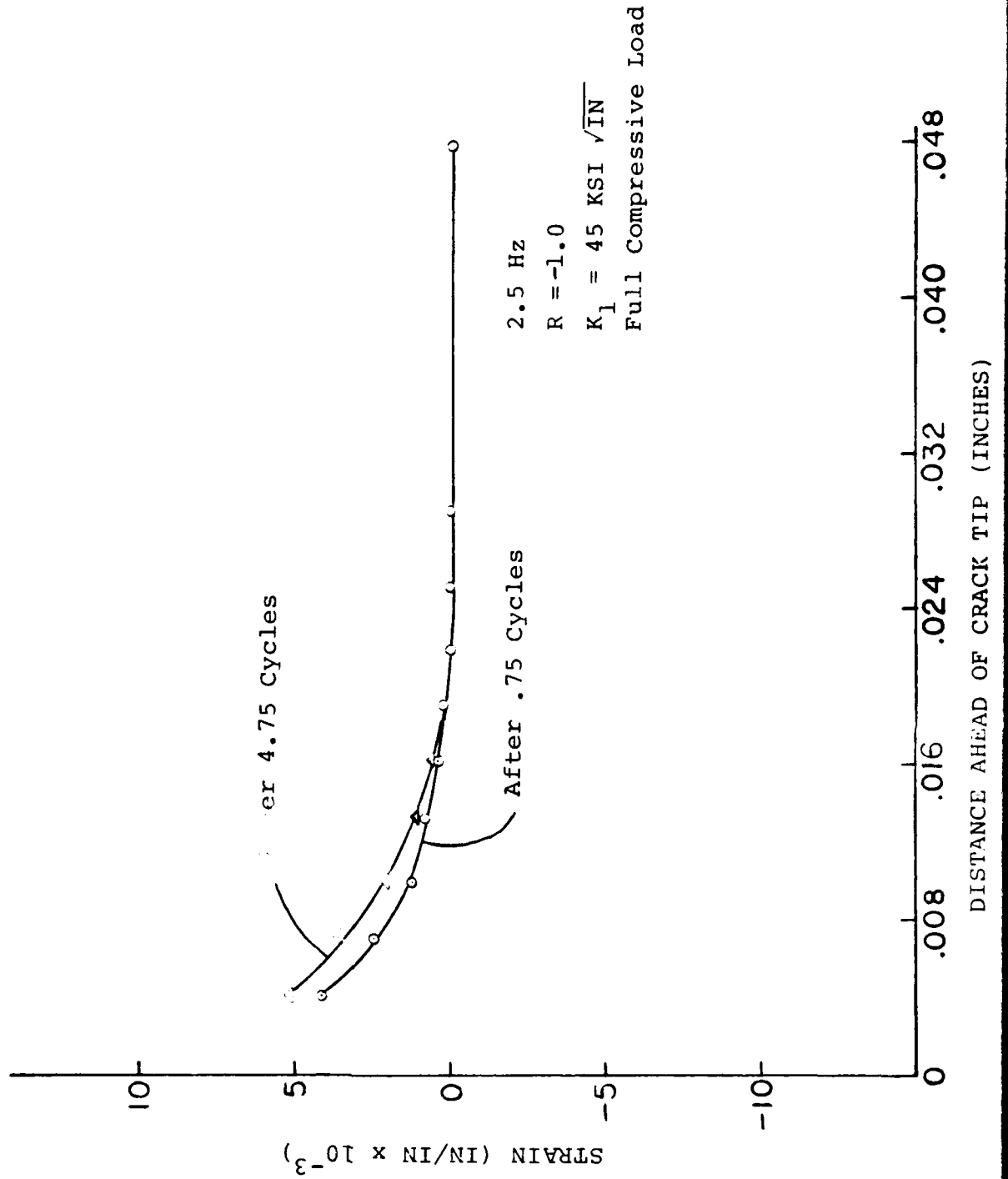


Fig 4.44 Y Strain Field Ahead of Crack Tip

2.5 Hz  
R = -1.0  
 $K_I = 35 \text{ KSI } \sqrt{\text{IN}}$   
Full Tensile Load

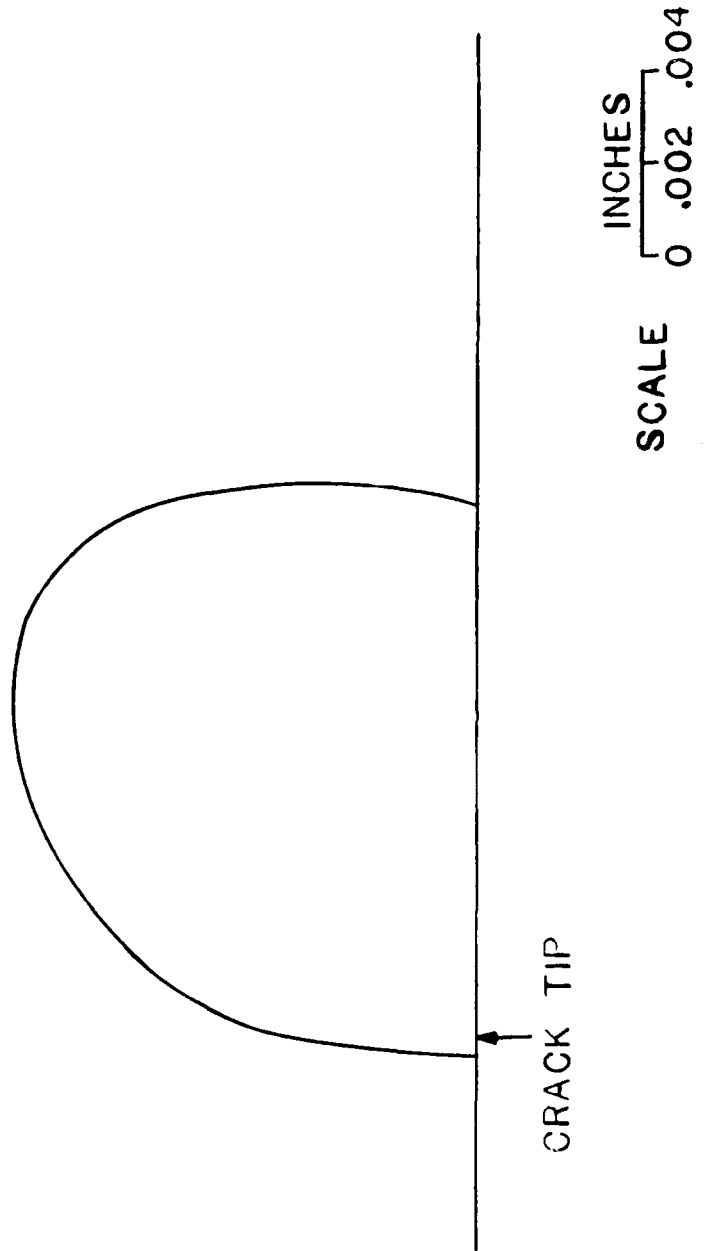


Fig 4.45 Plastic Zone After 2.25 Cycles

AD-A135 867

THE HIGH TEMPERATURE VISCOPLASTIC FATIGUE BEHAVIOR OF  
IN-100 USING THE BO. (U) AIR FORCE INST OF TECH  
WRIGHT-PATTERSON AFB OH SCHOOL OF ENGI.. R E WILSON  
SEP 83 AFIT/GAE/AA/835-6

2/2

UNCLASSIFIED

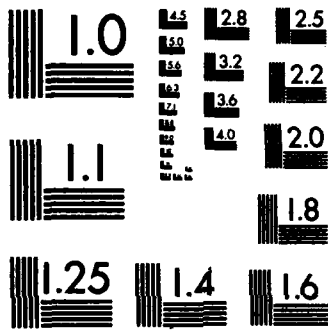
F/G 11/6

NL



END

FILMED  
USA  
DTIC



MICROCOPY RESOLUTION TEST CHART  
NATIONAL BUREAU OF STANDARDS-1963-A

2.5 Hz Full Tensile Load

$R=-1$   $K=45 \text{ KSI}\sqrt{\text{IN}}$

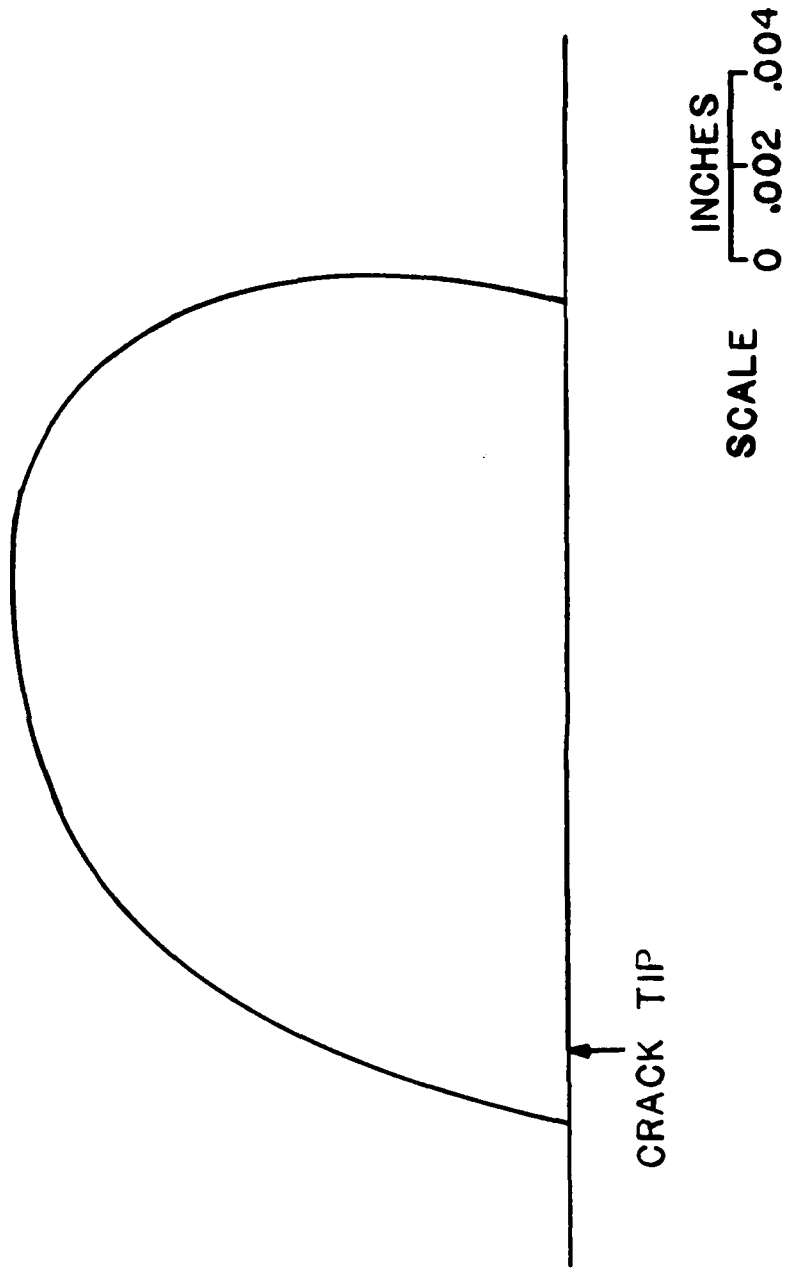


Fig 4.46 Plastic Zone After 2.25 Cycles

2.5 Hz R = -1.0  
 $K_1 = 35 \text{ KSI } \sqrt{\text{IN}}$  Full Compressive Zone

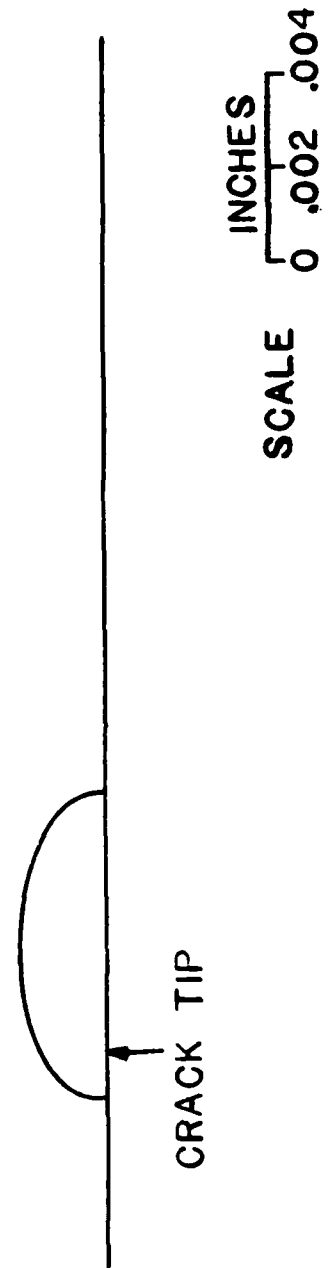


Fig 4.47 Plastic Zone After 2.75 Cycles

$R=-1$      $K=45 \text{ KSI}\sqrt{\text{IN}}$

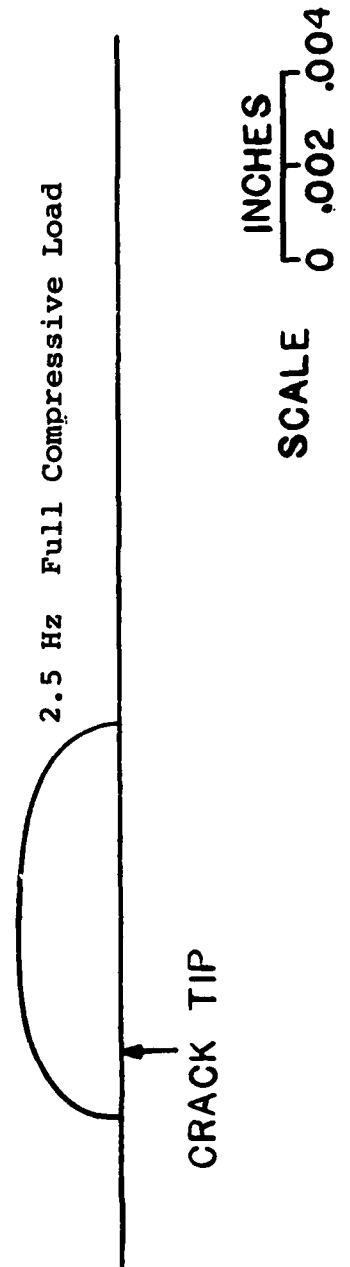


Fig 4.48 Plastic Zone After 2.75 Cycles

## V Conclusions

The results of the computations carried out using the Bodner viscoplastic constitutive equations to model the behavior of IN-100 at elevated temperatures yield the following conclusions for positive R-ratios.

1. The increase in strain realized after each load cycle under an R-ratio of .1 decreases in a manner which indicates that after 23 load cycles, the material will no longer undergo any more plastic straining. All data retrieved at this point would therefore, be applicable to fatigue tests of several thousand cycles.
2. The large majority of plastic straining occurs within the first three load cycles regardless of the R-ratio utilized.
3. The stress field ahead of the crack tip remains relatively constant after one to three load cycles regardless of the R-ratio utilized.
4. The size of the plastic zone is load dependent.
5. The cyclic behavior of the compact tension specimen near the crack tip is stress controlled.
6. The far field overall behavior of the compact tension specimen is elastic and independent of load level.

The following conclusions can be made based on the negative cyclic loading of a compact tension specimen after observing the results for five load cycles:

1. The edges of the crack do not meet when the load is released due to the large plastic overstress in the first load cycle.

2. The edges of the crack come into contact when a compressive load is applied, but an open region remains immediately behind the crack tip due to the large plastic overstress in the first cycle.

3. An elliptically shaped region of positive  $\gamma$ -strain is present in the vicinity of the crack tip even under totally reversed loads. The compressive load decreases the area of the significant positive  $\gamma$ -strain by a factor of twelve.

4. The crack tip remains blunted under reversed loading which other researches indicate leads to a higher fatigue life.

## Bibliography

1. Harris, J.A., Jr., Sims, D.L., Annis, C.G., Jr., "Concept Definition: Retirement for Cause of F-100 Rotor Components," AFWAL-TR-80-4118, Wright-Patterson AFB, Ohio, 1980.
2. Hill, R.J., "Report With Recommendations on Turbine Engine Component Fatigue Life Prediction," Air Force Materials Laboratory, Wright-Patterson AFB, Ohio, December, 1974.
3. Larsen, J.M. and Nicholas, T., "Load Sequence Crack Growth Transients in a Superalloy at Elevated Temperature," Presented at the 14th National Symposium of Fracture Mechanics, July, 1981, Los Angeles, Ca.
4. Hinnerichs, T.D., "Viscoplastic and Creep Crack Growth Analysis by the Finite Element Method," AFWAL-TR-80-4140, Wright-Patterson AFB, Ohio, 1981.
5. Stouffer, D.C., "A Constitutive Representation for IN-100," AFWAL-TR-81-4039, Wright-Patterson AFB, Ohio, 1981
6. Hudak, S.J., Jr., et.al., "Development of Standard Methods of Testing and Analyzing Fatigue Crack Growth Rate Data," AFWAL-TR-78-40, Wright-Patterson AFB, Ohio, May, 1978.
7. Owen, D.R.J., and Hinton, E., Finite Elements in Plasticity Theory and Practice, Chapter 7, pp. 215-270, Swansea, U.K.: Pineridge Press Limited, 1980.
8. Croneworth, J., and Haisler, W.E., "Development and Evaluation of an Uncoupled, Incremental Constitutive Model for Elastic-Plastic-Creep Behavior at Elevated Temperatures," Technical Report No. 3275-82-1, Office of Naval Research and Texas A&M University, 1982.

9. Bodner, S.R., and Zaphir, Z., "Implementation of Elastic Constitutive Equations into "NONSAP" with Applications to Fracture Mechanics," Proceedings ADINA Conference, MIT Report 82448-9, Aug 1979.
10. Bodner, S.R., and Stouffer, D.C., "Comments on Anisotropic Plastic Flow and Incompressibility," Int. J. Engng Sci. Vol. 21. No. 3, pp 211-215, 1983.
11. Smail, J.W., "The Viscoplastic Crack Growth Behavior of a Compact Tension Specimen Using the Bodner-Partom Flow Law," Master of Science Thesis, Dept of Aeronautics and Astronautics, Air Force Institute of Technology, Wright-Patterson AFB, Ohio, December, 1981.
12. Keck, J.E., "The High Temperature Viscoplastic Fatigue Behavior of a Compact Tension Specimen Using the Bodner-Partom Flow Law," M.S. Thesis, Department of Aeronautics and Astronautics, Air Force Institute of Technology, Wright-Patterson AFB, Ohio, 1982.
13. Cook, R.D., Concepts and Applications of Finite Element Analysis, New York: John Wiley & Sons, 1981.
14. Collins, J.A., Failure of Materials in Mechanical Design, New York: John Wiley & Sons, 1981.

## APPENDIX A

The computer program VISCO was modified for negative cyclic loading in several areas. The first change was made in the "read input data" section. Previously loads were only applied to the top of the hole when the input load is applied. Since the load was now to be applied at either the top or the bottom of the hole (depending on the algebraic sign of the load), the node numbers along the bottom of the hole needed to be included as part of the input data. These nodes are identified by the variable name NFN(I), where I goes from one to the number of nodes to be loaded in compression. The numbers of the negatively loaded nodes are read in line 980.

The load is shifted from the top of the hole to the bottom of the hole and back to the top in the "LOAD" subroutine. This shift of load depends on the sign of the input load. If the load is positive, the force is applied to nodes NFA(I), which are along the top of the hole. If the load is negative, the force is applied to nodes NFN(I), which are along the bottom of the hole. The algorithm for shifting the load is contained in lines 6470-6550.

To accomplish crack closure and crack opening, changes were made in the "SOLVE" subroutine. Nodes along the crack edge (91-97) could not be allowed to have negative displacements and must also have a zero force boundary condition for positive loads. A test was incorporated for the above nodes to determine if the displacement was negative, and if so, set

it equal to zero. The algorithm for crack closure and opening is contained in lines 7060-7090.

The remaining alterations were done in the "CYCLIC" subroutine. The changes allow any R-ratio and frequency to be modeled. TTOP and TBOT are variables to indicate at what time the load should be at its maximum and minimum values respectively. The load percentage PP is then calculated considering the point of time within the cycle given by TLOC and a linear load and unload profile. Changes in subroutine CYCLIC are in lines 12130-12200.











VITA

Roy E. Wilson was born on 27 October 1955 in Brattleboro, Vermont. He graduated from Brattleboro Union High School in 1973 and then enlisted in the USAF. After serving as an Electronic Warfare Systems Repairman in the Strategic Air Command, he received an AFROTC scholarship and attended Central Florida University. He received a B.S. in Mechanical Engineering in August 1979 and was commissioned as a second lieutenant in the USAF. He then served as a reliability and maintainability engineer in the Reconnaissance and Electronic Warfare Systems Program Office at Wright-Patterson AFB. He entered the School of Engineering, Air Force Institute of Technology in June 1982.

Permanent Address: 876 Pratt St  
Deland, Fla 32720

REPORT DOCUMENTATION PAGE		READ INSTRUCTIONS BEFORE COMPLETING FORM
1. REPORT NUMBER AFIT/GAE/AA/83S-6	2. GOVT ACCESSION NO. <b>A135867</b>	3. REPORT'S CATALOG NUMBER
4. TITLE (and Subtitle) THE HIGH TEMPERATURE VISCOPLASTIC FATIGUE BEHAVIOR OF IN-100 USING THE BODNER- PARTOM FLOW LAW	5. TYPE OF REPORT & PERIOD COVERED MS Thesis	
	6. PERFORMING ORG. REPORT NUMBER	
7. AUTHOR(s) Roy E. Wilson LLT, USAF	8. CONTRACT OR GRANT NUMBER(s)	
	10. PROGRAM ELEMENT, PROJECT, TASK AREA & WORK UNIT NUMBERS	
9. PERFORMING ORGANIZATION NAME AND ADDRESS Air Force Institute of Technology (AFIT/EN) Wright-Patterson AFB, Ohio 45433	12. REPORT DATE September 1983	
	13. NUMBER OF PAGES 109	
11. CONTROLLING OFFICE NAME AND ADDRESS Air Force Institute of Technology (AFIT/EN) Wright-Patterson AFB OH 45433	15. SECURITY CLASS. (of this report)  Unclassified	
	15a. DECLASSIFICATION/DOWNGRADING SCHEDULE	
16. DISTRIBUTION STATEMENT (of this Report)  Approved for public release; distribution unlimited		
17. DISTRIBUTION STATEMENT (of the abstract entered in Block 20, if different from Report)  Approved for public release; IAW AFR 190-17  G.F. DALBY, MAJOR, USAF Director of Public Affairs		
18. SUPPLEMENTARY NOTES  Approved for public release; IAW AFR 190-17. <i>G.F. Dalby</i> Lt. Col. E. WOLFAVER Dept for Research and Professional Development Air Force Institute of Technology (AIC) Wright-Patterson AFB OH 45433  26 SEPT 83		
19. KEY WORDS (Continue on reverse side if necessary and identify by block number)  Viscoplasticity Bodner-Partom Flow Law Finite Element Modeling		
20. ABSTRACT (Continue on reverse side if necessary and identify by block number)  Few studies have been made on the stress/strain field or plastic zone size ahead of a crack tip in a high temperature environment under varying load frequencies and stress levels. Fewer studies have incorporated compressive loads or analyzed the fatigue effect of a negative R-ratio on the fatigue characteristics of the superalloy in IN-100.		

UNCLASSIFIED

SECURITY CLASSIFICATION OF THIS PAGE(When Data Entered)

This study involves extending existing analysis of the stress field and plastic zone ahead of a crack tip in a compact tension specimen, through a larger number of load cycles and examining the nearly unexplored area of compressive loading of a crack in a superalloy. A USAF Materials Laboratory finite element computer program named VISCO was used for this study. The Bodner-Partom viscoplastic constitutive equations for describing the material behavior were utilized. Load spectra included various frequencies with R-ratios of 0.1 and -1.0 (zero mean load).

SECURITY CLASSIFICATION OF THIS PAGE(When Data Entered)

**END**

**FILMED**

**1-84**

**DTIC**